Stony Brook University

The official electronic file of this thesis or dissertation is maintained by the University Libraries on behalf of The Graduate School at Stony Brook University.

Quantitative imaging of 3D cerebral microvascular network dynamics by ultrahigh -

resolution optical coherence Doppler tomography (μODT)

A Dissertation Presented

by

Jiang You

to

The Graduate School

in Partial Fulfillment of the

Requirements

for the Degree of

Doctor of Philosophy

in

Biomedical Engineering

Stony Brook University

December 2017

Stony Brook University

The Graduate School

Jiang You

We, the dissertation committee for the above candidate for the

Doctor of Philosophy degree, hereby recommend

acceptance of this dissertation.

Dr. Yingtian Pan – Dissertation Advisor
Professor, Department of Biomedical Engineering

Dr. Shu Jia - Chairperson of Defense
Assistant Professor, Department of Biomedical Engineering

Dr. Congwu Du - Committee Member
Professor, Department of Biomedical Engineering

Dr. Styliani-Anna (Stella) E. Tsirka- Outside Committee Member
Professor, Department of Pharmacological Sciences

This dissertation is accepted by the Graduate School

Charles Taber

Dean of the Graduate School

Abstract of the Dissertation

Quantitative imaging of 3D cerebral microvascular network dynamics by ultrahigh -

resolution optical coherence Doppler tomography (μODT)

by

Jiang You

Doctor of Philosophy

in

Biomedical Engineering

Stony Brook University

2017

Optical domain technologies can provide high spatiotemporal resolution for biomedical research and therefore attract tremendous interests in multiple disciplines including psychiatry, neurology, ophthalmology, oncology, urology and many more. Optical coherence tomography (OCT), after more than 20 years of development, has been becoming one of the most widely-used bio-optical modalities not only for laboratory-based research but also for clinical applications. For example, OCT becomes the standard of care for diagnosing glaucoma. Additionally, its derived velocimetry, optical coherence Doppler tomography (ODT), also demonstrates the unique capability of mapping cerebral blood flow velocity (CBFv) of vascular networks with capillary resolution ($\phi<6\mu$m) and thus allows for the widespread utilization in numerous neurology studies.

Although ODT has been widely used in biomedical research, there remain several technical limitations including the shallow penetration depth, low sensitivity for imaging slow flow in capillary and the measurement error due to Doppler angle. To address these challenges, viable solutions are proposed in this dissertation. Chapter 1 starts with a comprehensive review over basic principle of OCT and ODT. Chapter 2-4 explicitly address these OCT technical challenges, for instance, using a 1310nm super-luminescent Diode (SLD) laser source to extend optical penetration depth, utilizing optical contrast agent: intralipid to enhance ODT's sensitivity for capillary flow detection, implementing numerical methods to extend ODT's dynamic range and decouple Doppler angle. In addition to these technical improvements, Chapter 5-6 address two biomedical challenges in oncology and psychiatry. Specifically, Chapter 5 introduces a longitudinal optical access to rodent cerebral vasculature and a method of tumor boundary detection, which provides a powerful insight into the tumor progression. Chapter 6 reveals the close correlation between cocaine-elicited transient ischemic attack (TIA) and hypo-perfused

cortex. Chapter 7 focuses on the development of multi-modality system and novel imaging scheme for the study of neurovascular coupling. Chapter 8 briefly concludes the contents presented in this dissertation and outlines the future development and potential applications of ODT.

Table of Contents

List of Figures

List of Tables

Acknowledgements

List of Publications

Journal Publications

- **You, J.**, Li, A., Park K., Du, C., Pan, Y. (2018) Detecting early tumor boundary using ultrahigh-resolution optical coherence tomography (in preparation)

- **You, J.**, Volkow, N. D., Park, K., Zhang, Q., Clare, K., Du, C., & Pan, Y. (2017). Cerebrovascular adaptations to cocaine-induced transient ischemic attacks in the rodent brain. **JCI insight**, **2**(5). (Cover Art)

- **You, J.**, Li, A., Du, C., & Pan, Y. (2017). Volumetric Doppler angle correction for ultrahigh-resolution optical coherence Doppler tomography. **Applied physics letters**, **110**(1), 011102. (Cover Art)

- **You, J.**, Zhang, Q., Park, K., Du, C., & Pan, Y. (2015). Quantitative imaging of microvascular blood flow networks in deep cortical layers by 1310 nm μODT. **Optics letters**, **40**(18), 4293-4296

- **You, J.**, Du, C., Volkow, N. D., & Pan, Y. (2014). Optical coherence Doppler tomography for quantitative cerebral blood flow imaging. **Biomedical optics express**, **5**(9), 3217-3230. (Cover Art)

- Du C., Volkow, N. D., **You J.**, Park K., Wee S., Koob G. F., & Pan Y. (2018) Compulsive-like Cocaine Self-administration Results in Ischemia and Triggers Angiogenesis in the Rodent Brain (in preparation)

- Gu, X., Chen, W., **You, J.**, Koretsky, A. P., Volkow, N. D., Pan, Y., & Du, C. (2018). Long-term optical imaging of neurovascular coupling in mouse cortex using GCaMP6f and intrinsic hemodynamic signals. **NeuroImage**, **165**, 251-264.

- Li, A., **You, J.**, Du, C., & Pan, Y. (2017). Automated segmentation and quantification of OCT angiography for tracking angiogenesis progression. **Biomedical Optics Express**, **8**(12), 5604-5616.

- Chen, W., **You, J.**, Gu, X., Du, C., & Pan, Y. (2016). High-speed swept source optical coherence Doppler tomography for deep brain microvascular imaging. **Scientific reports**, **6**.

- Zhang, Q., **You, J.**, Volkow, N. D., Choi, J., Yin, W., Wang, W., ... & Du, C. (2016). Chronic cocaine disrupts neurovascular networks and cerebral function: optical imaging studies in rodents. **Journal of biomedical optics**, **21**(2), 026006-026006.

- Park, K., **You, J.**, Du, C., & Pan, Y. (2015). Cranial window implantation on mouse cortex to study microvascular change induced by cocaine. **Quantitative imaging in medicine and surgery**, **5**(1), 97.

- Pan, Y., **You, J.**, Volkow, N. D., Park, K., & Du, C. (2014). Ultrasensitive detection of 3D cerebral microvascular network dynamics in vivo. **Neuroimage**, **103**, 492-501.

Conference Proceedings and Abstracts

- **You, J.**, Park, K., Du, C., & Pan, Y. (2015, March). Ultrasensitive quantification of cerebral capillary flow networks and dynamics. In SPIE BiOS (pp. 931218-931218). International Society for Optics and Photonics.

- **You, J.**, Park, K., Du, C., & Pan, Y. (2014, April). Quantification of capillary flow and density By ultrahigh-resolution OCT. In *Biomedical Optics* (pp. BT3A-61). Optical Society of America.

1. Introduction

The practice of medicine and related studies have always relied on the visualization of anatomic structure and its relation to biological function (medical imaging) which can date back to the 12th and 13th centuries. During the late medieval age, the study of anatomy was directly conducted by dissecting cadavers in anatomy theaters. This form of direct imaging had been being utilized for almost 600 years until x-ray was discovered by a German physicist Wilhelm Conard Röntgen in 1895. This marvelous discovery represented an unprecedented milestone in the history of biomedical imaging and began a new era of modern medical imaging because, for the first time, it shed new light on human's anatomy non-invasively. Since then biomedical imaging technologies have been rapidly developing accompanyed with the emergence of novel imaging technologies including ultrasonic imaging (US) in 1940s [1], positron emission tomography (PET) in 1960s [2], x-ray computed tomography (CT) [3] and magnetic resonance imaging (MRI) in 1970s [4], blood oxygenation level-dependent (BOLD)-functional MRI (BOLD-fMRI) in 1990s [5].

Although these medical imaging technologies have been widely used in clinical diagnosis and biomedical research, there are an increasing number of basic studies concerning the fundermental mechanisms underlying biological phenomena which require high spatiotemporal resolution for imaging biological compartments in vivo or ex vivo. For instance, BOLD-fMRI plays an important role in mapping brain activity in humans by characterizing local deoxygenation concentration in the brain. However, debate about neurovascular signaling [6] can never be closed by BOLD-fMRI due to its limited resolution. Additionally, the exact relation between fMRI signal and neuronal activity is still a matter of debate[7] which requires further studies with higher spatiotemporal resolution. Similar limitations also apply to other macroscopic medical imaging technologies such as US, PET and CT.

Recent advances in the bio-optical technologies can address the resolution challenge and thus play an increasingly important role in modern neurology research. For instance, two photon laser scanning microscopy (2PLSM) has been widely used in neurovascular [8] and neuro-metabolic research [9] for decades. With high spatial resolution, 2PLSM allows for imaging cerebral vasculature, dendrites, neuron, astrocytes and other cerebral components in the brain [10]. Alternatively, CBF and oxygenation are also good imaging contrast for brain function since neuronal activity occurs associated with glucose uptake, oxygenation utilization and the increase of local CBF [11]. Photo-acoustic tomography (PAT) is not only able to provide cerebral blood flow image with vessel-level spatial resolution but also able to map a blood oxygenation of the vascular network. By simultaneously acquiring oxygen utilization in vessel, PAT allows us to visualize metabolic signaling transfer during neuronal activity [12]. Additionally, optical coherence tomography (OCT) invented in 1990s [13] allows for 3D imaging of biological tissue and have been being widely used in multiple disciplines including ophthalmology, gastroenterology, cardiology, urology and so on. In the recent studies, its derived angiographies including optical coherence Doppler tomography (µODT) and phase/speckle variance angiography (µOCA) are playing increasingly critical role in neurology research[14-17] owning to its capillary resolution and relative large field of view compared to 2PLSM. Combining with fluorescence imaging, µODT permits simultaneously monitoring neuronal activity and functional hemodynamic response which shed new light on the debate of neurovascular coupling[18-20]. In this chapter, we first introduced the basic principle of OCT starting with the mathematical model

of Michelson interferometer. Then, a derivation of coherence length was given. Finally, a review of μODT briefly explains the prinicple of ODT as well as its challenges.

1. Principle of optical coherence tomography
    1.1. Optical coherence tomography (μOCT)

The idea of optical coherence tomography (OCT) was first introduced by D Huang et al in 1991 [13]. This innovative technique compounded the concept of ultrasound imaging and optical scattering. However, different from ultrasound imaging which measures acoustic wave delay time reflected from heterogeneous medium, OCT utilizes optical coherence between the sample and the reference mirror in a low coherence interferometry (LCI) to generate image contrast instead of measuring the time delay of light. By using LCI, OCT can provide noninvasive, high-resolution, in vivo 3D structural image of biological tissue.

The first-generation OCT, namely time domain OCT (Figure 1-1A), is based on Michelson interferometry. This set-up generates coherence signal between the scanning reference mirror and the reflective scatterers in biological tissue. Whenever the optical path length difference (OPD) lies within the range of coherence length (l_c), coherence occurs and thus generates imaging contrast. However, the classic time domain OCT has been replaced by Fourier domain (FD) or spectral domain (SD) OCT due to its limited imaging speed [21]. FD/SD-OCT can be further categorized into spectrometer based (Figure 1-1B) and swept source based OCT (Figure 1-1C) according to the type of light source and data acquisition. In recent years, swept source based OCT attracts tremendous attentions owning to its faster scanning rate (A-line > 400kHz [20]) compared to the spectrometer based SDOCT. However, severe phase jittering prevents its widespread utilization in vasculature imaging and, especially, quantitative flow imaging [22-24]. On the contrary, spectrometer based SDOCT demonstrates the superior phase stability which is suitable for flow imaging. Thus, this dissertation focuses on the development of spectrometer based SDOCT and its development.

In the following review, we will start with the mathematical treatment of multi-scatterer model based on Michelson interferometry then move to the basic principle of phase-resolved Doppler OCT.
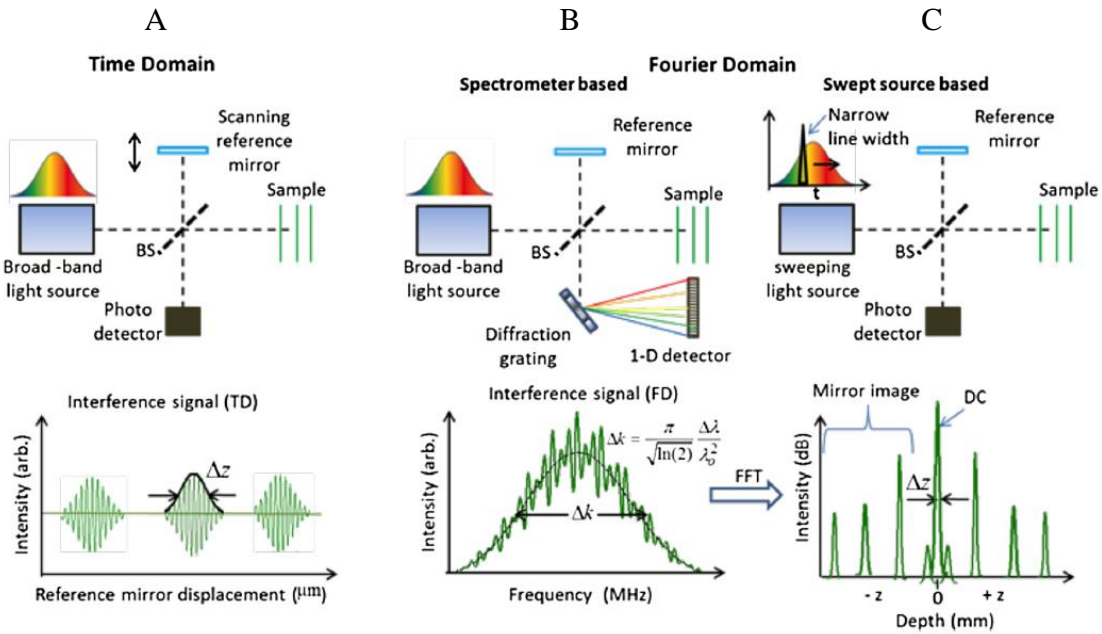
Figure 1-1 Schematic of different OCT modalities. A) Time domain OCT is based on Michelson interferometer which generates depth-resolved reflectivity profile by axially scanning the reference mirror. B) and C) are spectrometer based and swept source based Fourier domain/Spectral Domain OCT respectively. Both B) and C) rely on depth-modulated interference fringes which can be used to retrieve sample's reflectivity profile. B) Spectrometer based SDOCT acquires depth-modulated spectral fringes by a spectrometer and a line array detector. C) Swept source based SDOCT acquires depth-modulated spectral fringes by a balance detector while the swept laser sweeps a certain wavelength range[20].

1.2. Mathematical theory

$$E_R = \frac{E_i}{\sqrt{2}} r_R e^{i2kz_R}$$

$$E_S = \frac{E_i}{\sqrt{2}} \left[r_s(z_s) \otimes e^{i2kz_s} \right]$$

$$i_D = \rho \langle |E_R + E_S|^2 \rangle$$

3
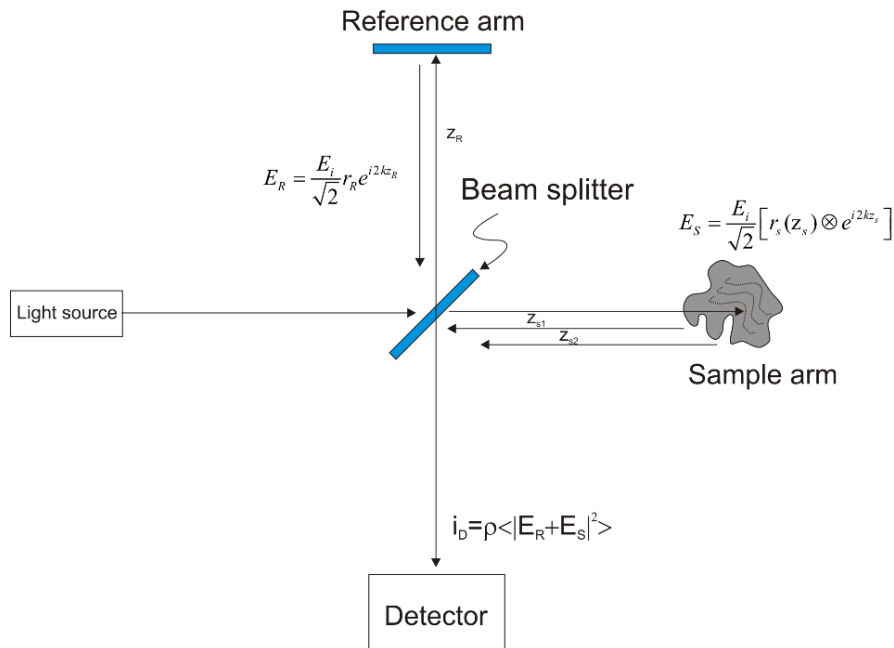
Figure 1-2 Schematic diagram of the simplified model of optical coherence tomography. For calculation convenience, the beam splitter center is arbitrarily defined as zero position (z=0). The reference arm is located at z=z_R. Multiple discrete reflectors $r_s(z_s)$ in tissue are located at z=z_{s1},z_{s2} ,z_{s3}… The coherence signal of the reference and sample arm is received by the detector.

OCT can be simplified down to a Michelson interferometer with a piece of biological tissue in the sample arm (Figure 1-2). The system is illuminated by a polychromatic plane wave whose expression is given by electromagnetic wave equation [25]:

$$E_i = s(\mathrm{k})e^{i(kz-\omega t)} \qquad \text{Eq. 1-1}$$

Where k=$2\pi/\lambda$ is wavenumber and $\omega=2\pi v$ is angular frequency. s(k) describes maximum amplitude of each spectral component of polychromatic light as a function of wavenumber (k). The intensity of incident light is split into two portions by 50:50 beam splitter and the reflected electric field from the reference mirror and a single layer of the tissue can be written as:

$$50:50 \text{ Beam Splitter}: E_S^2 = E_R^2 = \frac{1}{2}E_i^2 \qquad \text{Eq. 1-2}$$

$$\text{Reference arm}: E_R = \frac{E_i}{\sqrt{2}}r_R e^{i2kz_R} \qquad \text{Eq. 1-3}$$

$$\text{Sample arm}: E_S = \frac{E_i}{\sqrt{2}}\left[r_s(\mathrm{z}_s)\otimes e^{i2kz_s}\right] \qquad \text{Eq. 1-4}$$

Where r_R denotes the electric field reflectivity of the reference mirror whose path length is z_R. Similarly, $r_s(z_s)$ denotes the electric field reflectivity of the different tissue layers. To further simplify the OCT model, we assume the complex biological tissue consists of a series of discrete partial reflect scatterers whose scattering profile can be mathematically described as:

$$r_s(\mathrm{z}_s) = \sum_{n=1}^{N} r_{s_n}\delta(\mathrm{z}_s - \mathrm{z}_{s_n}) \qquad \text{Eq. 1-5}$$

Substitute Eq. 1-5 into Eq. 1-4:

$$\text{Sample arm}: E_S = \frac{E_i}{\sqrt{2}}\left[r_s(\mathrm{z}_s)\otimes e^{i2kz_s}\right] = \frac{E_i}{\sqrt{2}}\sum_{n=1}^{N} r_{s_n}e^{i2kz_s} \qquad \text{Eq. 1-6}$$

Convolution ($\otimes$) of term $r_s(z_s)$ and exp{$i2kz_s$} means that the total amplitude of the backscattered light from the sample tissue equals to the summation of the electric field reflected from multiple

scatterers at different depths (z_s). Thus, the average intensity at the detector of a single spectral component k is:

$$I_D(\text{k}, \omega) = \frac{\rho}{2}\left\langle |E_R + E_S|^2 \right\rangle = \frac{\rho}{2}\left\langle (E_R + E_S)(E_R + E_S)^* \right\rangle \qquad \text{Eq. 1-7}$$

$$I_D(\text{k}, \omega) = \frac{\rho}{2}\left\langle \left| \frac{s(\text{k})}{\sqrt{2}} r_R e^{i(2kz_R - \omega t)} + \frac{s(\text{k})}{\sqrt{2}} \sum_{n=1}^{N} r_{s_n} e^{i(2kz_{s_n} - \omega t)} \right|^2 \right\rangle \qquad \text{Eq. 1-8}$$

Where I_D denotes the average intensity of the coherence signal and the angular brackets <> denote the intensity integral along the response time. In addition, brackets also eliminate frequency ω of electric magnetic field which is several orders faster than the detector response time. Thus, $I_D(\text{k})$ can be expressed as

$$I_D(\text{k}) = \frac{\rho}{4}\left[\left\langle |s(\text{k})|^2 \right\rangle (r_R^2 + \sum_{n=1}^{N} r_{s_n}^2) \right]$$

$$+ \frac{\rho}{4}\left[\left\langle |s(\text{k})|^2 \right\rangle \sum_{n=1}^{N} r_R r_{s_n} \left(e^{i2k(z_R - z_{s_n})} + e^{-i2k(z_R - z_{s_n})} \right) \right] \qquad \text{Eq. 1-9}$$

$$+ \frac{\rho}{4}\left[\left\langle |s(\text{k})|^2 \right\rangle \sum_{n \neq m=1}^{N} r_{s_m} r_{s_n} \left(e^{i2k(z_{s_m} - z_{s_n})} + e^{-i2k(z_{s_m} - z_{s_n})} \right) \right]$$

If we only take the real parts into account, Eq. 1-9 can be re-written by Euler's equation $(e^{ix} + e^{-ix})/2 = \text{Re}[x] = \cos(x)$:

$$I_D(\text{k}) = \frac{\rho}{4}\left[S(\text{k})(r_R^2 + \sum_{n=1}^{N} r_{s_n}^2) \right]$$

$$+ \frac{\rho}{2}\left[S(\text{k}) \sum_{n=1}^{N} r_R r_{s_n} \cos\left[2k(z_R - z_{s_n}) \right] \right] \qquad \text{Eq. 1-10}$$

$$+ \frac{\rho}{2}\left[S(\text{k}) \sum_{n \neq m=1}^{N} r_{s_m} r_{s_n} \cos\left[2k(z_{s_m} - z_{s_n}) \right] \right]$$

Where $<|s(\text{k})|^2>$ is replaced by $S(\text{k})$ which represents the power spectrum density of the light source. This equation suggests that the coherence intensity of each spectral components (k) consists of three different terms: DC term, mutual coherence term and auto coherence term. The first term is DC term solely determined by the reflectivity of both the sample (r_S) and the reference arm (r_R) but independent on OPD between the two arms. Thus, the DC term does not provide any depth dependent information and usually eliminated. The second term is called mutual coherence or cross-correlation term in which OPD between the two arms is encoded and therefore is the desired signal for retrieving the scattering profile of the biological tissue. The third term is known as auto coherence or auto-correlation term that is generated across different reflective scatterers in the

same tissue and therefore is the undesired artifacts. In most cases, auto-correlation term can be negligible since its magnitude is several orders weaker than cross-correlation term due to either scattering and attenuation in biological tissue.

Generalized expression of OCT signal

Although the time domain OCT has been outdated, it is important to understand the basic image reconstruction and its relation to spectral domain OCT. We rewrite the Eq. 1-10 as functional of OPD=z_R-z_{Sn} and wavenumber k:

$$I_D(\mathrm{k}, r_R, r_{s_n}) = \frac{\rho}{4}\left[S(\mathrm{k})(\mathrm{r}_R^2 + r_{s_n}^2) \right]$$
$$+ \frac{\rho}{2}\left[S(\mathrm{k}) r_R r_{s_n} \cos\left[2k(\mathrm{z}_R - \mathrm{z}_{s_n}) \right] \right]$$
$$+ \frac{\rho}{2}\left[S(\mathrm{k}) r_{s_m} r_{s_n} \cos\left[2k(\mathrm{z}_{s_m} - \mathrm{z}_{s_n}) \right] \right]$$

Eq. 1-11

Eq. 1-11 suggests that, for single reflector r_{sn} at depth z_{sn}, the intensity of coherence signal is governed by wavenumber k and path length difference z_R-z_{Sn}. Eq. 1-11 can be considered as the general expression for both time and spectral domain OCT signals because it generates a 3D intensity space as functional of wavenumber (k), scatterer depths (z_{Sn}) and reference path length (z_R). Specifically, the signal of time domain OCT can be obtained through integrating wavenumber and all scatterer depths while treating the reference mirror location (z_R) as a variable since the reference mirror mechanically scans along the axial direction constantly changing OPD respect to the zero position. Differently, the signal of spectral domain OCT can be obtained through integrating the scatterer depths and treating the reference path length as a constant and wavenumber as a variable. Because, in spectral domain OCT, the reference mirror is fixed, and the coherence signal is dispersed and detected by a linear spectrometer.

Time domain: For time domain OCT, the acquired data by the photo detector can be considered as the sum of the coherence fringe contributed by each individual spectral compartment (k) and each scatterer along z direction. Thus, the result is obtained by the integral of Eq. 1-11 along k and z_{Sn}:

$$TD(\mathrm{z}_R) = \frac{\rho}{4}\left[S_0\left[r_R^2 + \sum_{n=1}^{N} r_{S_n}^2 \right] \right]$$
$$+ \frac{\rho}{2}\left[\int_0^\infty S(k)dk \sum_{n=1}^{N} r_R r_{S_n} e^{-(z_R - z_{S_n})^2 \Delta k^2} \cos\left[2k_0(z_R - z_{S_n}) \right] \right]$$

Eq. 1-12

According to Eq. 1-12, retrieving the scattering profile $r_{sn}(z)$ relies on mechanical scan of reference mirror.

Spectral domain: Spectral domain OCT improves data acquisition speed by circumventing the mechanical movement of the reference mirror. Instead of mechanically scanning the mirror in the reference arm and acquiring the coherence signal at individual depth r(z_R) by a photo detector, spectral domain OCT utilizes linear array CCD/CMOS to capture the coherence signal dispersed

into multiple spectral components. This spectral fringe can be considered as the integral of Eq. 1-11 along z_{sn} treating the reference mirror z_R as a constant. To retrieve the reflectivity profile of the tissue, we take Fourier transform of integrated Eq. 1-11 :

$$
\begin{aligned}
SD(z)\big|_{z_R} &= \Im\left\{SD(k)\big|_{z_R}\right\} \\
&= \frac{\rho}{8}\gamma(z)\left[r_R^2 + \sum_{n=1}^{N} r_{S_n}^2\right] \\
&+ \frac{\rho}{4}\left[\gamma(z)\otimes\sum_{n=1}^{N} r_R r_{S_n}\left(\delta\left(z\pm 2(z_R - z_{S_n})\right)\right)\right] \\
&+ \frac{\rho}{8}\left[\gamma(z)\otimes\sum_{m\neq n=1}^{N} r_R r_{S_n}\left(\delta(z\pm 2(z_{S_n} - z_{S_m}))\right)\right]
\end{aligned}
$$

Eq. 1-13

Where $SD(z)|_{zR}$ denotes the retrieved reflectivity profile of the target sample, the normalized Gaussian function S(k) and its inverse Fourier transform $\gamma(z)$ are given by

$$\gamma(z) = e^{-z^2\Delta k^2} \xleftrightarrow{\Im} S(k)$$

Eq. 1-14

Thus, the spectral domain OCT signal $SD(z)|_{zR}$ can reflect the true reflectivity profile $r_s(z_s)=\sum r_{sn}\delta(z_s\text{-}z_{sn})$ and the convolution term $\gamma(z)$ determines the axial resolution.

1.3. Coherence length and axial resolution

Although the system setup and the data acquisition approach of TDOCT and SDOCT are different, the fundamental principle of imaging reconstruction of both systems are the same: temporal coherence. Therefore, the complex degree of coherence $\gamma(\tau)$ of temporal coherence determines the axial resolution of both systems (Eq. 1-14). $\gamma(\tau)$ is a normalized function of self-coherence function or auto-correlation function $\mathbf{\Gamma}(\tau)=<\mathbf{u}(t+\tau)\mathbf{u}^*(t)>$ where $\mathbf{u}$ represents the optical disturbance[26, 27]:

$$\gamma(\tau) = \frac{\Gamma(\tau)}{\Gamma(0)}$$

Eq. 1-15

The auto-correlation functions can be obtained by taking inverse Fourier transform of the power spectrum density function of the light source:

$$\vec{\Gamma}(\tau) = \int_0^\infty 4S^{(r,r)}(\upsilon)e^{-j2\pi\upsilon\tau}d\upsilon$$

Eq. 1-16

Where $S^{(r,r)}(\upsilon)$ is the power spectral density function of the real-valued optical disturbance $u^r(t)$. Substitute Eq. 1-16 into Eq. 1-15, we can get:

$$\vec{\gamma}(\tau) = \frac{\Gamma(\tau)}{\Gamma(0)} = \frac{\int\limits_{0}^{\infty} 4S^{(r,r)}(\upsilon)e^{-j2\pi\upsilon\tau}d\upsilon}{\int\limits_{0}^{\infty} 4S^{(r,r)}(\upsilon)d\upsilon} = \int\limits_{0}^{\infty}\overline{S}(\upsilon)e^{-j2\pi\upsilon\tau}d\upsilon = \Im\left\{\overline{S}(\upsilon)\right\} \qquad \text{Eq. 1-17}$$

Where $\overline{S}(\upsilon)$ is a normalized power spectral density function:

$$\int\limits_{0}^{0}\overline{S}(\upsilon)d\upsilon = 1 \qquad \text{Eq. 1-18}$$

Thus, the complex degree of coherence $\gamma(\tau)$ can be simply obtained by taking inverse Fourier transform of the normalized power spectral density function. we use full width half maximum (FWHM) to quantify the "width" of $\gamma(\tau)$ as the definition of coherence time or the system's axial resolution.

For OCT application, the light source is expected to provide Gaussian shape normalized power spectral density:

$$\overline{S}(\upsilon) \cong \frac{2\sqrt{\ln 2}}{\sqrt{\pi}\Delta\upsilon}\exp\left[-\left(2\sqrt{\ln 2}\frac{\upsilon-\overline{\upsilon}}{\Delta\upsilon}\right)^{2}\right] \qquad \text{Eq. 1-19}$$

Where $\Delta\upsilon$ is FWHM of power spectrum density. By a simple inverse Fourier transform, the complex degree of coherence can be obtained:

$$\vec{\gamma}(\tau) = \exp\left[-\left(\frac{\pi\Delta\upsilon\tau}{2\sqrt{\ln 2}}\right)^{2}\right]\exp(-j2\pi\overline{\upsilon}\tau) \qquad \text{Eq. 1-20}$$

The modulus of $\gamma(\tau)$ characterizes the visibility decay while the second term gives the fringes with constant phase. Per the FWHM definition of coherence time, the modulus of $\gamma(\tau)$ equals to 0.5:

$$\gamma(\tau) = \exp\left[-\left(\frac{\pi\Delta\upsilon\tau}{2\sqrt{\ln 2}}\right)^{2}\right] = \frac{1}{2} \qquad \text{Eq. 1-21}$$

$$\tau = \pm\frac{2\ln 2}{\pi\Delta\upsilon}, \tau_{c} = \frac{4\ln 2}{\pi\Delta\upsilon} \qquad \text{Eq. 1-22}$$

For round-trip OCT system, the system's axial resolution is given by

8

$$l_c = \frac{c\tau_c}{2} = \frac{2c\ln 2}{\pi\Delta\upsilon} = \frac{2\ln 2}{\pi}\frac{\lambda_0^2}{\Delta\lambda}$$

Eq. 1-23

Where c is the speed of light, λ_0 is the central wavelength of the light source and $\Delta\lambda$ denotes the FWHM of the spectrum.

2. Optical coherence Doppler tomography

The advances of modern imaging technologies lead to the extension of biomedical interest in *in vivo* functional study. Recently, optical Doppler coherence tomography (ODT) and its derived methods [28, 29] have demonstrated their unique capability of quantitative imaging for rodent vasculature with large field of view and capillary resolution. Therefore, those technologies have been being rapidly developed in the last decade and playing crucial role in neurology study [30-32].

2.1. Mathematical theory

Proposed by Austrian physicist Christian Doppler in 1842, Doppler effect describes the frequency shift of a wave signal reflected from a moving target. For imaging vascular blood flow, frequency or wavelength shifts can characterize the speed of red blood cells. In addition, it is also affected by the central wavelength of the signal source and the vessel angle with respect to the z axis:

$$\Delta f = \frac{2v\cos(\theta)}{c}f_0 = \frac{2v\cos(\theta)}{\lambda_0}$$

Eq. 1-24

Where Δf denotes the frequency shift. f_0 is the central frequency of source signal, v is the velocity of moving targets (e.g. red blood cells) and λ_0 represents the central wavelength of the light source. The equation elucidates that Doppler effect can only detect the axial velocity component $v_z=v\cos(\theta)$ of the moving target. To retrieve the full velocity, one need to measure either the transverse velocity $v_{x,y}$ [33-35] or detect the 3D vessel angle[36-38].

To quantify the blood flow velocity, the frequency shift need to be measured. However, detecting the optical frequency shift is more difficult than detecting the acoustic frequency shift. Dating back to 1997, ODT was reconstructed by directly measuring Doppler frequency shift defined as the difference between the carrier frequencies [39, 40]. However, the short Fourier transform used in this method fails to decouple the imaging speed and flow velocity sensitivity. In 2000, Y. Zhao et.al proposed a phase-resolved ODT which addressed the imaging speed limitation without sacrificing the flow sensitivity and has been commonly used since then[16].

In phase-resolved ODT, Doppler frequency shifts Δf can be calculated based on Doppler phase shift $\Delta\phi$ between two adjacent A-scan due to its direction relation to frequency:

9

$$\Delta f = \frac{\Delta \phi}{2\pi dt} = \frac{\phi_{i+1,z} - \phi_{i,z}}{2\pi \cdot \Delta T} = \frac{\tan^{-1}\left(\frac{\mathrm{Im}\{A_{i+1,z}\}}{\mathrm{Re}\{A_{i+1,z}\}}\right) - \tan^{-1}\left(\frac{\mathrm{Im}\{A_{i,z}\}}{\mathrm{Re}\{A_{i,z}\}}\right)}{2\pi \cdot \Delta T} \qquad \text{Eq. 1-25}$$

Where Δf and $\Delta \phi$ are frequency and phase shift, respectively. $\phi_{i,z}$ denotes the phase information of analytical i^{th} A-scan at depth of z. ΔT is the time interval between i^{th} and $(i+1)^{th}$ A-scan. Additionally, a cross-correlation algorithm is wildly used to retrieve phase difference owing to its better performance [41-44]:

$$\Delta \phi = \arctan \left\{ \frac{\sum_{j=1}^{J}\left[\mathrm{Im}(A_{j+1,z})\mathrm{Re}(A_{j,z}) - \mathrm{Im}(A_{j,z})\mathrm{Re}(A_{j+1,z})\right]}{\sum_{j=1}^{J}\left[\mathrm{Re}(A_{j+1,z})\mathrm{Re}(A_{j,z}) - \mathrm{Im}(A_{j,z})\mathrm{Im}(A_{j+1,z})\right]} \right\} \qquad \text{Eq. 1-26}$$

Substituting Eq. 1-24 into Eq. 1-25, the velocity of red blood cells can be expressed as the function of Doppler phase shift.

$$\frac{2v\cos(\theta)}{\lambda_0} = \frac{\Delta \phi}{2\pi \Delta T} \qquad \text{Eq. 1-27}$$

$$v = \frac{\Delta \phi \lambda_0}{4\pi n \Delta T \cos \theta} \qquad \text{Eq. 1-28}$$

Where n is the refractive index, ΔT is the time interval between two A-scans, λ_0 represent the central frequency and θ is Doppler angle with respect to the incident light direction. Eq. 1-29 elucidates that the velocity of red blood cells v is proportional to Doppler phase difference $\Delta \phi$ between two adjacent A-scans.

2.2. Minimum detectable flow velocity

The sensitivity of ODT is governed by the minimum detectable flow (v_{min}) which is determined by the overall phase variance $\sigma_{overall}$ (rad):

$$v_{min} = \frac{\sigma_{overall} \lambda_0}{4\pi n \Delta T \cos \theta} \qquad \text{Eq. 1-29}$$

The overall phase floor consists of two parts: the phase noise due to the system's unstability (σ_ϕ) and the phase noise due to the decorrelation of lateral scanning ($\sigma_{\Delta x}$)

$$\sigma_{overall} = \sqrt{\sigma_\phi^2 + \sigma_{\Delta x}^2} \qquad \text{Eq. 1-30}$$

For single point scan (without scanning), $\sigma_{\Delta\phi}$ is solely determined by the system's signal-to-noise ratio (SNR) given by [45]:

$$SNR = \left(\left| \vec{E} \right| / \left| \vec{n} \right| \right)^2 \qquad \text{Eq. 1-31}$$

Where **n** is a random noise vector and **E** describes light returning from the sample. The standard deviation of the measured complex electric field is given by:

$$\sigma_{\phi'}^2 = \frac{1}{2} \left(\left| \vec{n} \right| / \left| \vec{E} \right| \right)^2 \qquad \text{Eq. 1-32}$$

Thus, the minimum detectable phase σ_ϕ between $\phi_{i,z}$ and $\phi_{i+1,z}$ is given by:

$$\sigma_\phi = \sqrt{2\sigma_{\phi'}^2} = \frac{1}{\sqrt{SNR}} \qquad \text{Eq. 1-33}$$

However, the scanning scheme does not satisfy the inherent assumption that A-scan is acquired at the same location where the physical structures remain consistent. Especially, in biological tissue, the micro-motion from tissue itself and inherent heterogeneous biological structure lead to the failure of this assumption. Therefore, the phase variance $\sigma_{\Delta x}$ induced by the lateral scanning need to be considered which is given by:

$$\sigma_{\Delta x} = \sqrt{\frac{4\pi}{3} \left\{ 1 - \exp\left[-2\left(\frac{\Delta x}{d} \right)^2 \right] \right\}} \qquad \text{Eq. 1-34}$$

Where Δx is the increment step in lateral scanning and d is $1/e^2$ beam with at the focus.

B.H Park et. al experimentally measured $\sigma_{\Delta x}$ and σ_ϕ as increasing the incremental step (Δx) of lateral A-scan which is represented as the fraction of beam width[45]. As Δx greater than 0.1, the overall phase variance Eq. 1-30 is dominated by lateral scan induced phase variance $\sigma_{\Delta x}$. In the other word, this curve provides us a clue of minimizing $\sigma_{ovreall}$ and an approach of improving the ODT sensitivity for ultra-slow flow: to minimize the incremental step Δx, or to oversample A-line number to improve the phase correlation between adjacent A-scans[46]. However, the overall phase variance stops decreasing until it hits the σ_ϕ boundary which means the minimum detectable flow is ultimately limited by the system's phase unstability.

11
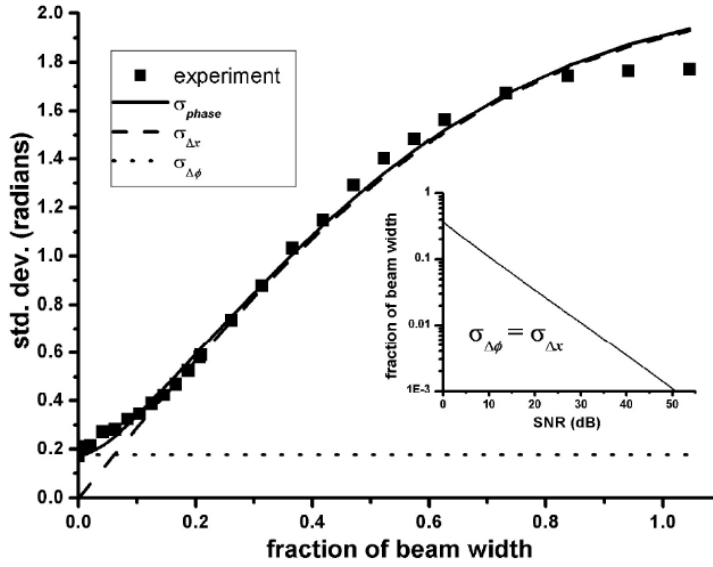
Figure 1-3 Phase variance as functional of incremental step of lateral scan (fraction of beam width $\Delta x/d$, d is $1/e^2$ beam with at the focus). Solid line: theoretical modeling of overall phase variance ($\sigma_{ovreall}$); Dashed line: phase variance due to lateral scan ($\sigma_{\Delta x}$); Dot line: Phase variance due to system SNR (σ_{ϕ}). Square Dot: Experimental data of overall phase variance. Inset: set $\sigma_{\Delta x}=\sigma_{\phi}$ to correlate incremental step size with the corresponding SNR measured at single spot without scanning[45].

2.3. Phase wrapping threshold velocity

The detetable velocity is limited when the Doppler phase difference reaches its maximum π. The speed limitation is known as phase wrapping threshold veloicty v_{wrap} which can be calculated as [47]:

$$v_{wrap} = \frac{\Delta\phi_{max}\lambda_0}{4\pi n\Delta T\cos\theta} = \frac{\pi\lambda_0}{4\pi n\Delta T\cos\theta} = \frac{\lambda_0}{4n\Delta T\cos\theta} or \frac{\lambda_0 f}{4n\cos\theta} \qquad \text{Eq. 1-35}$$

Where f denotes A-scan rate equal to $1/\Delta T$. When the velocity of moving particles is faster than v_{wrap}, the detected phase is wrapped to the opposite end of the phase range ($\pi\rightarrow 0$) and therefore leads to the ambiguous velocity measurement. As depicted in Figure 1-4, 1% intrailpid flow phantom (15μL/min) was imaged at 10kHz and 5kHz by ODT. 10kHz ODT image demonstrates the normal parabolic distribution while, in 5kHz case, the flow velocity in the center flips over to the opposite end of phase range showing a lower speed. Because v_{wrap} at 10kHz is two times of that at 5kHz ($v_{wrap,10kHz}= 2v_{wrap,5kHz}$). This artifact is known as phase wrapping and can be corrected by phase unwrapping algorithms. Some phase correction approaches rely on searching the phase jumps in the wrapped phase signal and correct it by adding phase compensator $M\cdot 2\pi$ (M=1,2,3...) to each data pixel[48, 49]. However, the detection of phase jump may fail due to the severe noise level and thus requires filtering algorithms [50].

12
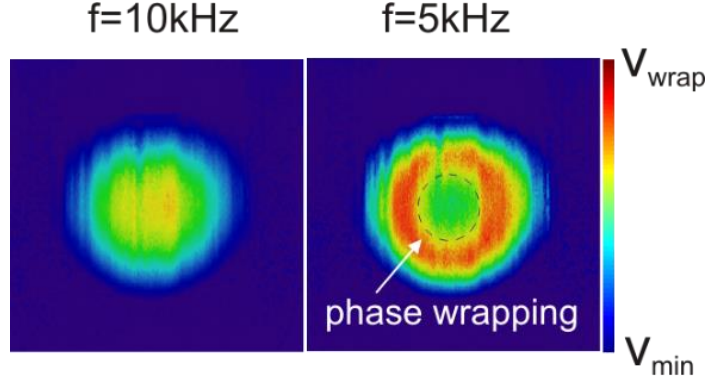
Figure 1-4 Phase wrapping artifacts in slow A-scan rate. Fast scan rate f=10kHz. Slow scan rate f=5kHz. 1% intralipid flow phantom (15µL/min) in capillary tube ϕ~280µm.

2.4. Maximum detectable flow velocity

v_{wrap} is not the ultimate velocity limitation because the wrapped velocity can still be retrieved by the post unwrapping algorithms. Instead, the maximum detectable velocity is ultimately determined by interferometric fringes washout artifacts due to the finite integration time (τ) of the camera.

For spectrometer-based system, integration time τ_{SD} can be expressed as:

$$\tau_{SD} = D \cdot T \qquad \text{Eq. 1-36}$$

Where τ_{SD} denotes the integration time, D is the detector duty cycle and T is A-scan frequency. According to the generalized coherence signal equation (Eq. 1-11), the moving scattering particles (e.g. red blood cell) may introduce SNR degradation within the integration time τ:

$$I'(\mathrm{k}) = \frac{\rho}{2} S(\mathrm{k}) r_R r_{s_n} \int_0^\tau \cos\left[2nk(\Delta z + v_{RBC} t)\right] dt \qquad \text{Eq. 1-37}$$

$$I'(\mathrm{k}) = \frac{\rho}{2} S(\mathrm{k}) r_R r_{s_n} \cos\left[2nk\Delta z\right] \sin c\left(2nkv_z\tau\right) \cdot \tau \qquad \text{Eq. 1-38}$$

Where $\Delta z = z_R - z_S$ represents OPD between the sample and the reference arm in Eq. 1-11. The SNR degradation due to sinc(x)=sin(x)/x term is known as fringe washout which occurs when the reflector's motion is too fast yielding a maximum phase shift π during the integration time τ. The corresponding velocity limits is known as fringe washout velocity v_{wash}[47]:

$$v_{wash} = \frac{\lambda_0}{4n\tau_{SD}\cos\theta} = \frac{\lambda_0}{4nDT\cos\theta} \qquad \text{Eq. 1-39}$$

13

According to Eq. 1-39, v_{wash} is determined by the integration time. The shorter the integration time, the faster v_{wash} is. However, shorter integration time may decrease system SNR. Thus, careful consideration needs to be taken when choose the camera integration time.

2. Improved optical penetration depth by 1300nm µODT

Cerebral cortex consists of six cortical layers characterized by their histological, neurochemical and neurophysiologic differences [51]. Such differences lead to heterogeneous neurovascular responses of different cortical layers to various brain stimuli, which has been attracting tremendous interest in brain functional studies. However, to understand the hemodynamic response of each cortical layer to a brain stimulation, there is demand for new neuroimage modalities. Not only can this unique imaging technology provides high spatiotemporal resolution imaging quantification of cerebral blood flow velocity (CBFv) in capillaries but also a large field of view (FOV), especially sufficient image depth (e.g., >800µm). f-MRI has been widely used for whole-brain functional studies [ref], but higher resolution is required in more and more applications to characterize cerebral hemodynamic changes in individual vascular compartments elicited by neuronal activations. Two-photon microscopy (TPM) has been widely applied for high-resolution 3D imaging of cerebral microvasculature, and a recent study demonstrated extended penetration depth to >1mm in mouse cortex with newly developed 1280nm TPM[52]. Yet, TPM requires fluorescence tracking that may complicate pharmacological studies and quantitative CBFv imaging is usually limited a small FOV (e.g., single or few micro vessels). Photoacoustic microscopy is recently reported to enable high-resolution cerebral micro vasculature and blood oxygenation imaging, which is important for brain functional study [12].

Recent advances in optical coherence-domain techniques such as optical microangiography (OA) [53] and optical coherence Doppler tomography (ODT) [44] have permitted tracker-free 3D visualization of cerebrovasculature and quantitative CBFv imaging of vessels of different caliber in mouse cortex. For instance, ultrahigh-resolution ODT (µODT) has been shown to image microcirculatory CBFv network dynamics and identify laser disruption of local microvasculature and more importantly spreading of spontaneous microischemia elicited by repeated cocaine administration, which requires both high flow detection sensitivity and large FOV . It is noteworthy, however, that due to limited image depth, the insightful heterogeneous CBFv network dynamics in different cortical layers in response to various brain activation is not yet fully understood.

To tackle this challenge, we developed a new µODT powered by a 1310nm broadband light source which recuded optical scattering and thus extended optical penetration depth. Its advantages in imaging depth was demonstrated by comparing with our previous 800nm µODT system. Additonally, data acquisition and processing speed was dramatically improved by the advanced circular buffer structure and GPU parallel computing. Besides the system improvement, we also provided two clinically related applications : measuring microvascular density of cortical layers and monitoring depth-dependent brain dysfunction to show the new 1310nm µODT's great impact on biomedical and pre-clinical studies.

1. Methods
    1.1. Ultrahigh-resolution optical coherence tomography system

We developed a new µODT system at 1310nm where the reduced light scattering of biological tissue may lead to increased penetration depth for flow imaging. An ultra-broadband light source (Thorlab LSC2000C, λ_0=1310nm, $\Delta\lambda_{FWHM}$ =220nm) was used to illuminate a spectral-domain OCT engine consisting of a 2×2 broadband fiberoptic Michelson interferometer (Thorlab optics fiber couple, λ=1310±70nm). Light exiting the reference arm was collimated, propagated through a pair of wedge prisms for dispersion compensation. Light beam is focused on a retroreflective mirror to maximize the bandwidth ($\Delta\lambda_{cs}\approx$200nm) of the cross-spectrum (i.e., $S_{cs}(\lambda)\equiv$ $[S_s(\lambda)\cdot S_r(\lambda)]1/2$, where $S_s(\lambda)$, $S_r(\lambda)$ were the sample and reference power spectra), so that a high axial resolution of 2.8µm in brain tissue was reached, which is defined by the transform-limited coherence length, L_c=2(ln2)/$\pi\cdot\lambda_0^2/\Delta\lambda_{cs}$. The collimated light was transversely scanned by a fast servo mirror and focused onto mouse cortex through a cranial window with an f18mm/NA0.25 NIR objective, yielding a lateral resolution of 3.2µm. The backscattered light from mouse cortex was recombined with the reference light in the detection fiber connected to a custom high-resolution spectrometer (Wasatch Photonics spectrometer). The interference fringes spectrally encoding the depth profile were detected by a high-speed line scan InGaAs camera (2048-pixels, 145k-lines/s; GL2048, Sensors Unlimited) synchronized with sequential transverse scans for 2D/3D µOCT acquisition. Focus tracking was implemented to enable full cortex imaging by incrementing focal plane 200~300µm in z (depth) direction. Cross-sectional µODT image v_z, x was reconstructed from the measured phase difference $\Delta\phi z$, x between adjacent A-scans by phase subtraction method (PSM: v_z, x = $\lambda\Delta\varphi/(4\pi n\tau\cos\theta)$; where θ is incident angle with flow, n is refractive index of brain, τ is duration between 2 A-scans) or by phase-intensity method (PIM) [15]. Since this process was computationally intensive, graphic processing unit (GPU) with custom GUI programming was implemented to boost FFT and phase detection. The GPU boosted control console allowed for real-time rendering and display of maximum intensity projection (MIP) of µODT images, e.g., as fast as 473 fps for a B-scan containing 1k×2k pixels. Therefore, the dynamic features of the CBFv network were readily visualized during imaging [37].
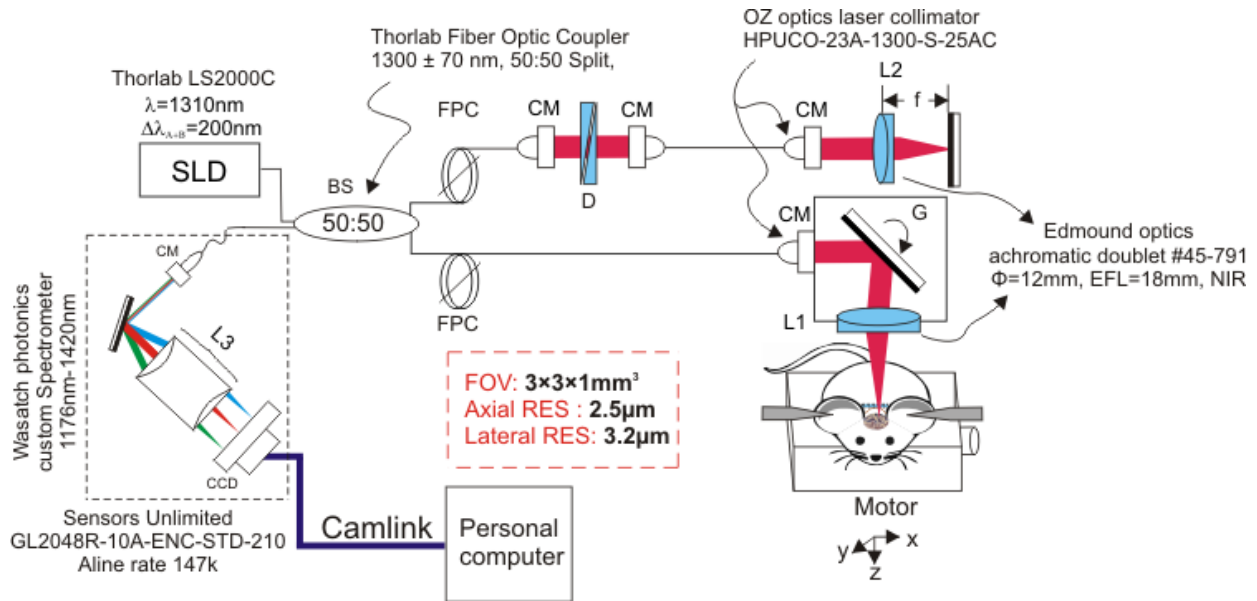
Figure 2-1 Schematic diagram of SD-OCT system. SLD: superluminescent diode, BS: beam splitter, CM: Collimator, FPC: Polarization controller, G: Galvo scanner L1: Sample arm objective, L2: Reference arm lens, L3: Detector lens group, D: dispersion compensation prism pairs.

1.2. Superluminence diode broadband light source

Thorlab LS2000C, a superluminence diode (SLD) broadband light source consisting of two SLDs, was used to illuminate the new OCT system. Thorlab LS2000C has 3 channels including CH A, CH B and CH A+B corresponding to difference outputs. The light source is not only able to provide the extended spectrum combing two SLDs from CH A+B (purple) but also able to provide the low coherence light of individual SLD from either CH A (Blue) or CH B (Red). It is noteworthy that a custom modification was applied to maximize the output power from the third channel CH A+B. To minimize the energy loss, fiber splicing is avoided through bypassing the output of individual SLD A and B port. As a result, we can achieve the maximum output power of ~11mW from CH A+B with spectral FWHM of ~200nm.
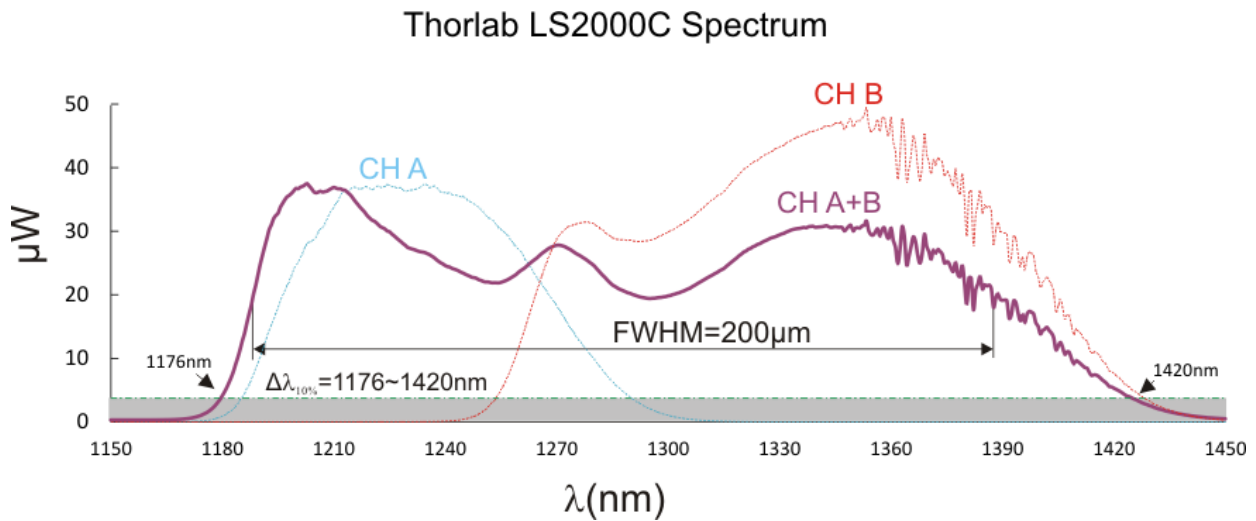
Figure 2-2 Spectrum of Thorlab LS2000C. Spectral bandwidth is extended by combining two SLDs. Only $\Delta\lambda_{10\%}$=244nm (1176~1420nm) is projected onto line array camera.

1.3. Custom high-speed spectrometer

A custom spectrometer (Wasatch photonics) (Figure 2-3) was developed in which the coherence signal was firstly dispered by a volume holographic phase grating (895 line/mm) and then projected onto a high-speed line scan InGaAs camera (2048-pixels, 145k-lines/s; GL2048, Sensors Unlimited) through a mulit-element focusing objective (EFL=80mm). A spectral 10% cut-off (Figure 2-2) was applied as a trade-off between axial resolution (Δz) and depth range (z_{max}) and thus yielded the spectral range of 244nm from 1176nm to 1420nm ($\Delta\lambda_{10\%}$=244nm). The imaging depth (z_{max}) is limited by the wavenumber spacing (δk) of the spectrometer [54, 55]. The imaging depth in the Fourier domain is given by:

$$z_{\max} = \frac{\pi}{2 \cdot \delta k} \; and \; \delta k = \frac{2\pi \cdot \Delta\lambda_{10\%}}{N\lambda_0^2} \qquad \text{Eq. 2-1}$$

$$z_{\max} = \frac{\lambda_0^2}{4(\Delta\lambda_{10\%} / N)} \qquad \text{Eq. 2-2}$$

Where λ_0=1310nm represents the central wavelength of the light source and $\Delta\lambda_{10\%}$=244nm is the spectral range projected onto the linear camera. N=2048 represents the total pixel number of the camera. Substituting all the parameters in Eq. 2-2, the maximum depth range is ~3.6mm in free space and 2.6mm in biological tissue (n=1.38).
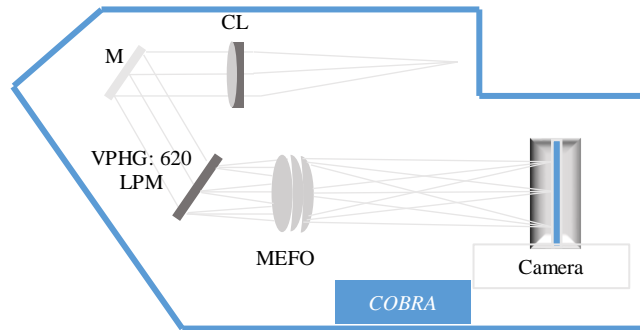
Figure 2-3 Schematic of custom Cobra spectrometer (Wasatch Photonics); CL: Collimating Lens; VPHG: Volume Holographic Phase Grating; M: Mirror; MEFO: Multi-element focusing Objective.

1.4. Custom data acquisition software

1.4.1. Graphic user interface (GUI)

A custom OCT data acquisition software was developed on Qt 5.6.1 (MSVC2013,32bit), a cross-platform software development framework that allows for fast access to user interface design, multi-threading processing and serial port communicating. The software consists of 5 sections (Figure 2-4) including 1. Scanning parameter configuration 2. Selection of scanning modes and data saving 3. Tabs a) motor stage control b) 2D Galvo scanning set-up c) Log information d) GPU information. 4. Spectrum plot 5 real time OCT/ODT display.
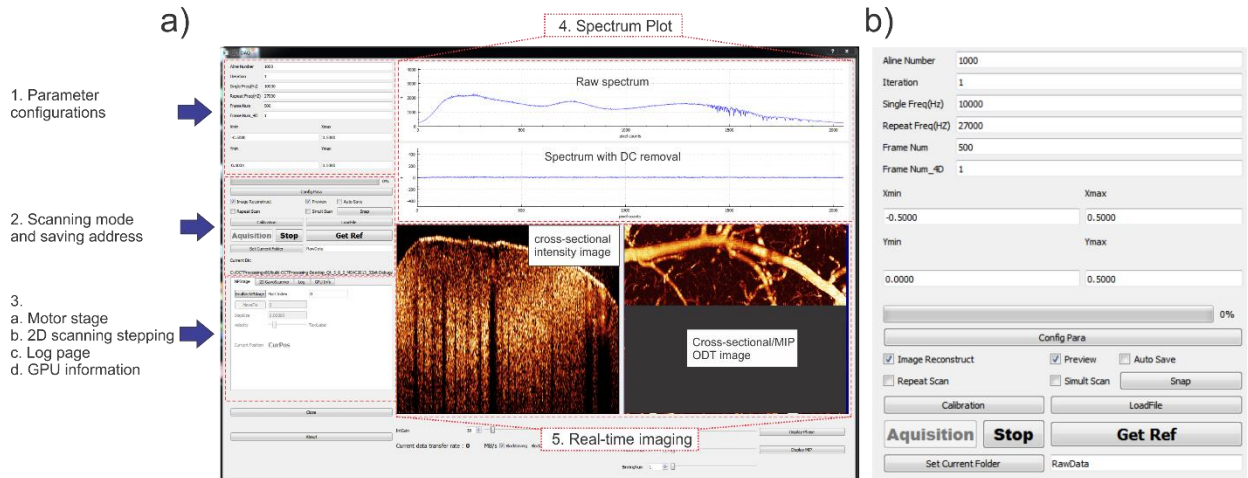
Figure 2-4 a) Graphic user interface (GUI) of real-time data acquistion software for µOCT system. 1. Scanning parameter configeration. 2 Scanning mode selection 3. Tabs a) motor stage b) 2D scanning stepping c) Log page d) GPU information 4 Spectrum plot 5) real time imaging display. b) Zoom-in image of section 1 and section 2.

The present software can run in 3 modes: ODT only, OCA only and simultaneous ODT&OCA. In ODT mode, A-scan number (N_{ODT}) is the production of **Aline Number** and **Iteration**, the scanning frequency of which is given by **Single Freq.** OCA mode requires repeated B-frames at the same y position. A-scan number of single B-frame (N_{OCA}) is **Aline Number** and the number of repetition is given by **Iteration.** The scanning frequency of OCA is given by **Repeated Freq**. **Frame Num** determines the number of B frame of a full 3D scan. It is noteworthy that in the simultaneous mode, the software completes the cross-sectional scan of OCA and ODT sequentially at the same position (Y_n) before incrementing to the next position (Y_{n+1}). To enable the dynamic monitoring blood flow change in functional studies, the software also allows for 4D scan in which **Frame Num_4D** gives the number of 3D volume in a 4D. **Xmin, Xmax, Ymin and Ymax** in voltage define the scanning range of 2D galvo scanners. For an achromatic of EFL=18mm, 1 voltage corresponds to 2mm on the focal plane. Table 2-1 summarizes the configurations and check boxes for 3 different scanning modes.

Table 2-1 Configigerations of µODT GUI software

	ODT only	OCA only*	OCA and ODT*
A-line# of B-scan	AlineNumber×Iteration	AlineNumber	
A-line Frequency	Single Freq	Repeat Freq	
B frame	Frame Num		
Image Recon	Enable		
Preview	Enable		
Auto Save			Enable
Repeat Scan		Enable	Enable
Simultaneous Scan			Enable

* Not available with ring buffer structure.

1.4.2. Ring buffer structure and GPU parallel computing

High speed data acquisition and real-time imaging allows for the dynamic tracking of transient biological events (e.g. functional hyperemia) and for visualizing the flow change instantaneously during the experiment. However, in the old software, the data acquisition and processing speed were limited by the sequential buffer structure and CPU computing. Specifically, the old buffer structure integrated B-frame snapping into a "for" loop in which image reconstruction and data saving modules were called sequentially. Thus, the software initiated the camera and called the acquisition function for each iteration which profoundly decreased the frame rate. Because the maximum frame rate was limited by the latency of calling function and cannot exceed 20fps (latency≈0.065s). Additionally, the B-frame rate was also affected by the image reconstruction thread. Although the multi-thread structure was implemented in the previous version, B-frame acquisition was still delayed due to the inaccessible memory buffer during the incomplete reconstruction process.

To address this problem, the new custom GUI software was designed using ring buffer structure that circumvents the latency issue and dramatically improves B-frame rate and processing speed. Because, in ring buffer structure, the initialization and the acquisition function were called only once and no function was called during the acquisition. Additionally, the ring buffer structure also separated the data acquisition thread from the image processing/saving thread. In the other word, the acquisition rate of B-frames is solely determined by the camera triggering rate regardless the proceeding of the reconstruction/saving thread. Furthermore, graphic processing unit (GPU) parallel computing was implemented to improve the imaging processing speed. Different from CPU that processes task sequentially on a small number of processing units, GPU owns thousands of processing cores and processes the broken-down sub-tasks parallelly. To enable GPU parallel computing, CUDA, a parallel computing platform and programming model invented by Nvidia, was used which enables dramatic increases in computing performance by harnessing the power of the GPUs. CUDA platform also provides a complete toolkit for programming the CUDA architecture that includes the compiler, debugger, profiler, libraries and other information for developers.

Different from single buffer that was repeatedly overwritten in the previous structure, the ring buffer structure is a circular memory buffer array consisting of N buffers (e.g. N=100), each of which holds a single B-frame. Figure 2-5 demonstrates the schematic flow chart of the new buffer structure and data exchange between the data acquisition thread and the image processing thread. Once the **Acquisition** button (Figure 2-4) was clicked, both the data acquisition thread and the image processing/saving thread started. The data acquisition thread kept acquiring B-frame spectral data followed by the camera TTL triggering signal regardless of the incompletion in the processing thread and directly stored the acquired frames into the circular buffer array. At the meantime, the most recently available 2D spectral data (B-frame) stored in the buffer array was fetched by the image processing/saving thread in which the image processing was completed taking the advantages of GPU parallel computing. To reconstruct quantitative vascular flow velocity map in real-time, a commercial GPU (Geforce GTX 1050 Ti, Nvidia) was used. The right panel of Figure 2-5 shows the flow chart of image reconstruction in GPU that consists of 4 main CUDA kernels: 1) k space calibration 2) CUDA Fast Fourier Transform (cuFFT) 3) Intensity/Phase calculation 4) 2D medial filter and. The raw spectral data was parallelly processed in GPU yielding two output images: intensity and Doppler flow image which were copied back to the host memory for instantaneous display.

However, it is possible that the data acquisition thread is faster than the image processing/saving thread causing the overwriting of the unprocessed frame. To avoid this scenario, the ring buffer structure utilizes a "lock-release" mechanism with which the unprocessed memory buffer is "locked" and not allowed to be overwritten until it is "released" when the processing completes. Thus, each buffer in the circular buffer array was repeatedly "locked", "released" and overwritten until the camera triggering task completed that terminated both the data acquisition thread and the image processing/saving thread. Finally, the reconstructed intensity and Doppler flow image stored on the host memory were sent back to the main GUI panel for visualizing the tissue structure and blood flow.
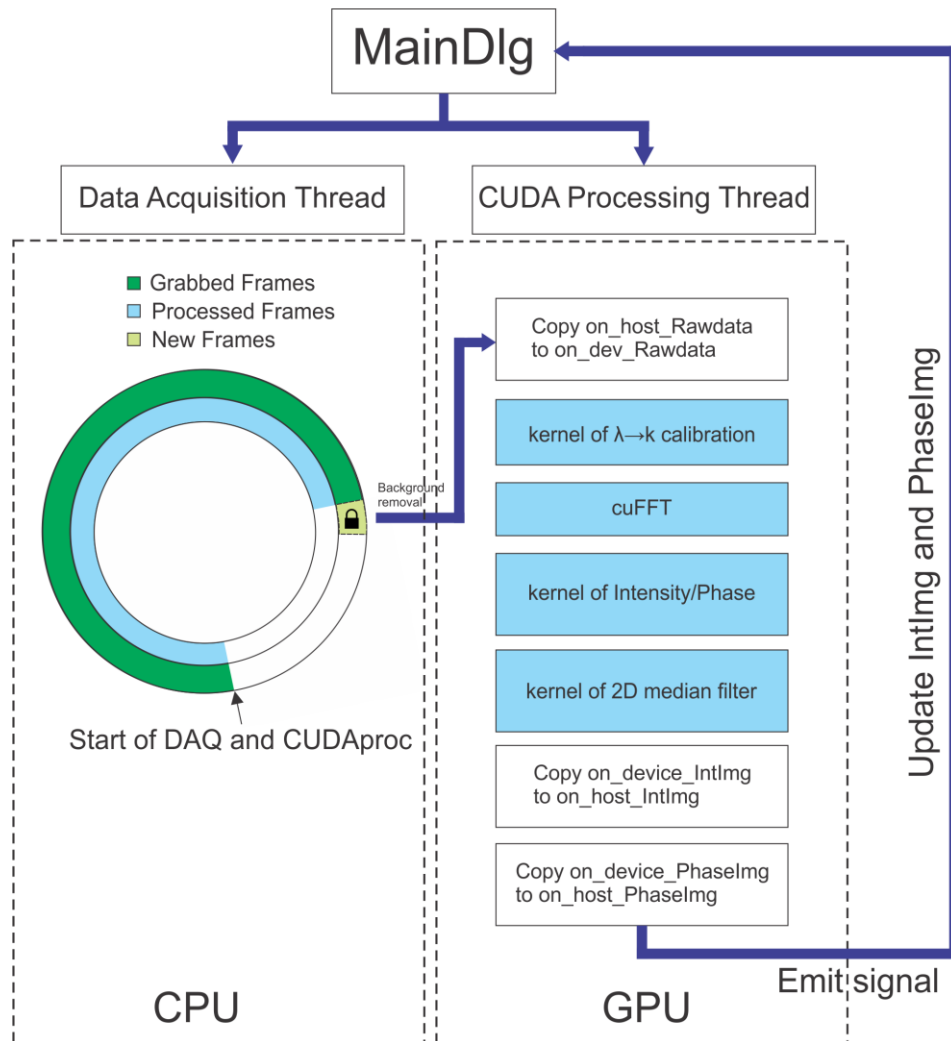
Figure 2-5 Schematic flow chart of data acquisition thread and image processing/saving in GPU. Left panel: the ring buffer structure with "lock-realease" mechanism. Each buffer in the circular buffer array is repeatedly "locked", "released" and overwritten until the camera triggering task completes. Right panel: Real-time image reconstruction thread consisting of 4 CUDA kernals including k-space linearization, CUDA FFT, Intensity/Phase calculation and 2D medial filter.

2. Results
2.1. Sensitivity roll-off

Sensitivity roll-off is one of the most important quality metrics for evaluating the custom spectrometer's performance that characterizes the reduced visibility of spectral fringes at high fringe frequency. Several factors affect the capability of resolving spectral fringe, for instance, optical resolution, the finite pixel width and inter-pixel cross-talk[56]. Mathematically, the acquired signal can be considered as the convolution of the interference signal with Gaussian beam profile and the finite pixel size. Therefore, in Fourier domain, the sensitivity roll-off rate R(z) is the production of a sinc function and a Gaussian function expressed by [54, 57, 58]:

$$R(\text{z}) = \left(\frac{\sin \varsigma}{\varsigma} \right)^2 \exp\left[-\frac{w^2}{2\ln 2}\varsigma^2 \right]$$

Eq. 2-3

Where $\varsigma = (\pi/2)\cdot(z/z_{max})$ characterizes depth position normalized to the maximum imaging depth $z_{max}=3.6$mm (Eq. 2-2) and $\Delta\lambda$ is the wavelength spacing $\Delta\lambda=\Delta\lambda_{10\%}$/pixel number$=244nm/2048=0.12$nm. $w=\delta\lambda/\Delta\lambda=0.6$ represent the ratio of spectral resolution to the wavelength spacing where spectral resolution $\delta\lambda=0.072$nm is determined by the spectrometer's optics design. To measure the sensitivity roll-off curve of the custom spectrometer, we recorded and reconstructed the OCT point spread function (PSF) of a single reflector (e.g. mirror) at various depths (500µm-3500µm) using the modified interferometer shown in Figure 2-6 a). Before the experiment, the optical system was well aligned reaching the maximum power output (I_{max}) from the detection arm. During the experiment, alignment was conducted for each time the second mirror was placed at the new position. When the power output from the detection arm was comparable to I_{max} suggesting the system was well aligned, the coherence fringes was recorded and OCT PSF was calculated. Theoretical sensitivity roll-off curve R(z) calculated by Eq. 2-3 is plotted in Figure 2-6 b) showing -15dB at $z_{max}=3.6$mm while the actual measured roll-off curve is much worse showing -30dB at z_{max}. Alternatively, 10dB roll-off depth is usually used as the metric for quantifying the spectrometer's performance which, for our case is, about 2 mm in free space and 1.5mm in biological tissue (n=1.38) sufficiently deep for imaging mouse cortex.

a)

b)
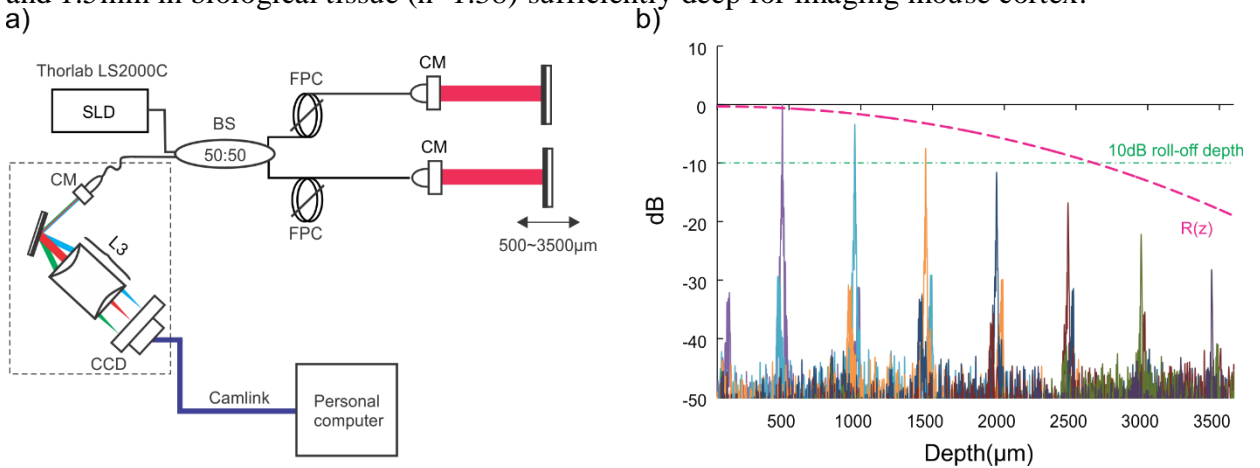
Figure 2-6 Meausrement of sensitivity roll-off. a): The modified interferometer for measuring sensitivity roll-off curve. b): OCT PSF at different imaging depths (500µm-3500µm). Dashed purple line: Theoretical roll-off curve as function of imaging depth. Dashed green line: 10dB roll-off line:

2.2. Phase variance v.s. A-scan number

Phase variance is commonly used to characterize the background noise level of ODT image and thus determines the sensitivity for flow measurement. As mentioned in Chapter 1, the overall phase variance ($\sigma_{overall}$) is the compound effect of the finite system SNR (σ_ϕ) and phase decorrelation between adjacent A-scans during lateral scan ($\sigma_{\Delta x}$). According to Eq. 1-30, oversampling can dramatically reduce the phase variance contributed by lateral scan and thus push phase stability towards SNR limit. To measure the system phase variance and its response to oversampling, 2% agarose gel adulterated with 1% Intralipid® 20% was imaged by µODT with different A-line numbers at scan frequency of 10kHz in order to mimic the scattering biological tissue in the actual case. Phase variance was determined by statistically analyzing the adjacent A-line phase difference of the central area of a fixed scanning range (~ 2mm). As A-line number increases, phase variance dramatically decreases. It is noteworthy that the improvement becomes minor when the oversampling rate was greater than 10 suggesting the variance component contributed by the decorrelation was already minimized and the overall phase variance was dominated by the system SNR. Therefore, by substituting the smallest overall phase variance into Eq. 1-29, the minimum detectable flow velocity v_{min} can be calculated. We found v_{min} is as slow as 3µm/s which is sufficiently sensitive to detect most of slow flow in cerebral microvascular networks even in the heterogeneous capillaries.
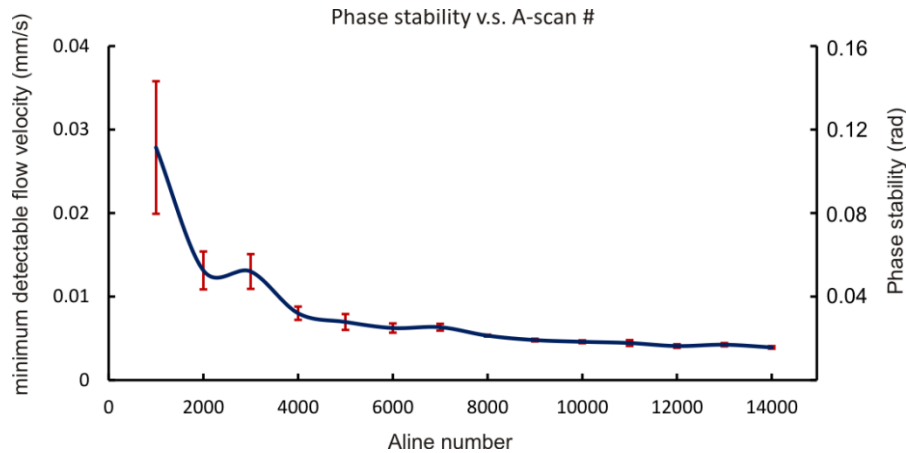
Figure 2-7 Phase stability as function of oversampling rate from 1.5 to 21. µODT images were taken at A-scan frequency of 10kHz.

2.3. Improved data acquisition speed and GPU parallel computing

To quantitatively evaluate the superior speed performance of our custom software, we first measured the time cost (s) for processing a B-frame consisting of various A-line number: 1000, 2000, 5000, 10000 with both CPU and GPU. To avoid system inconsistency, the results are averaged over 10 repeated measurements. Figure 2-8 a) compares the time cost for processing the

same B-frame by CPU and GPU. It is noteworthy that the CPU processing has to complete several tasks sequentially including k-space linearization, FFT, intensity mapping and Phase subtraction in which intensity mapping and phase subtraction are the most computationally intensive tasks taking 82.7% of total time cost for 10000 A-line number. The considerable time cost is mainly caused by pixel manipulation in multiple 2D loops which can be dramatically improved by using parallel computing. Expectedly, GPU parallel computing (GeForce GTX 1050 Ti) significantly reduced time cost by about 55 times in average over different B-frame sizes. In addition to the improved processing speed, we also quantified the improvement of B-frame rate by the circular buffer structure. Figure 2-8 b) compares the B-frame rate (1000*2048 pixel) at different A-line frequencies by the previous snap buffer structure and the circular buffer structure. At low A-line frequency of 10kHz equivalent to a theoretical B-frame rate of 10fps, the difference was minor and B-frame rate using circular buffer is only 1.6 times faster than that using snap buffer. However, a huge difference was found at high A-line frequency. For example, at A-line frequency of 147kHz equivalent to a theoretical B-frame rate of 147fps, data acquisition by circular buffer is 9.1 times faster reaching a practical frame rate of 146.67fps comparable to the theoretical speed. On the contrary, the frame rate of snap buffer is dramatically limited by the latency about 0.0621s leading to a frame rate limitation of 16.1fps.

fps	10	20	30	50	100	147
■ Snap Buffer	6.45	9.17	10.64	12.82	15.87	16.13
■ Circular Buffer	10.00	19.96	29.97	49.55	100.00	146.67
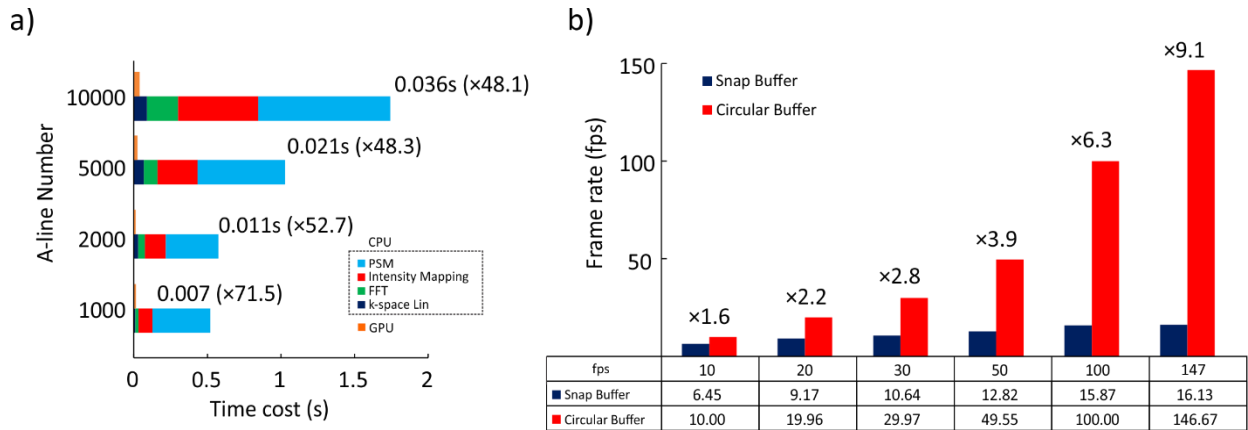
Figure 2-8 Speed performance of the custom software. a) Comparison of CPU and GPU processing speed for single B-frame of different A-line numbers. b) Comparison of averaged B-frame rate using snap buffer and circular buffer at different theoretical frame rate.

2.4. Extended penetration depth

In parallel, to assess the image-depth improvement of the new 1310nm µODT for deep flow detection, a prior 800nm µODT system was included for comparison. This 800nm system provides an axial resolution of 1.8µm in tissue (illuminated with an 8-fs Ti: Al_2O_3 laser with λ_0=800nm, $\Delta\lambda_{cs}$=154nm), a transverse resolution of 3.0µm, and A-scan rate of up to 27kHz. To avoid phase saturation and low sensitivity for capillary flow imaging, A-line rates for 1310nm µODT were set to 6kHz and 3kHz for imaging upper (0-200µm) and lower (>200µm) cortex, respectively. The equivalent A-line rate for 800nm µODT were utilized based on $\lambda_{800nm}\cdot f_{800nm} = \lambda_{1310nm}\cdot f_{1310nm}$ to match phase shift detected by the two systems.

Eight-week-old CD-1 mice (Charles River, Kingston, NY; male, 25-30g/each) were used to conduct the CBFv imaging studies. After being anethetized with inhalation of 2% isoflurane (in 100% O2), the animal wsa mounted on a custom stereotaxic frame to eliminate motion artifacts. A 3×3mm2 cranial window was created on the right side of the somatosensory motor cortex. The exposed cortical surface was immediately covered with 2% agarose gel and affixed with a 100-µm-thick glass coverslip using biocompatible cyanocrylic glue.

Figure 2-9 compares 3D CBFv images of mouse sensorimotor cortex acquired by 800nm vs. 1310nm µODT. Although MIP images show almost no difference except slightly higher capillary density in Figure 2-9(b') likely due to more detectable deeper capillary flows, their 3D renderings in Figure 2-9(a, b) clearly demonstrate the increase in CBFv image depth from ~300µm for 800nm µODT to ~1.4mm for 1310nm µODT, namely, over 4-time improvement. This improvement is crucial, because the new technique enables quantitative imaging of the CBFv networks across the entire cortex (I-VI layers), thus potentially allowing us to quantify their dynamic heterogeneity in response to functional brain activations. Detailed image analyzes presented in Figure 2-9(c-f) clearly indicate heterogeneous CBFv distribution along the depth in the cortex, e.g., 0-0.2mm, predominantly occupied by large, fast pial flows (c: layers I-II); 0.2-0.4mm, occupied mostly by densely populated short capillary flows likely perpendicularly oriented (d: layers III- top IV); 0.4-0.6mm, slightly less populated but longer capillary flows likely oriented more towards lateral directions (e: layers IV-V); 0.6-1.4mm, continuously less populated, slower capillary flows (layers: VI- corpus callosum). Figure 2-9(g) plots the statistical figure of the capillary flow networks in different cortical layers, showing that the capillary CBFv continued to increase from 0.14 ± 0.05mm/s on top to 0.20 ± 0.04mm/s at ~600µm, but then dramatically decreased to 0.08 ± 0.04mm/s within the bottom cortical layers. This rapid decline in capillary CBFv in the deep cortex (e.g., 0.6-1.4mm) could be caused by either the system sensitivity loss or the inherent CBFv reduction in the microcirculatory networks or by their confounds. Thus, further study may be needed to clarify this.
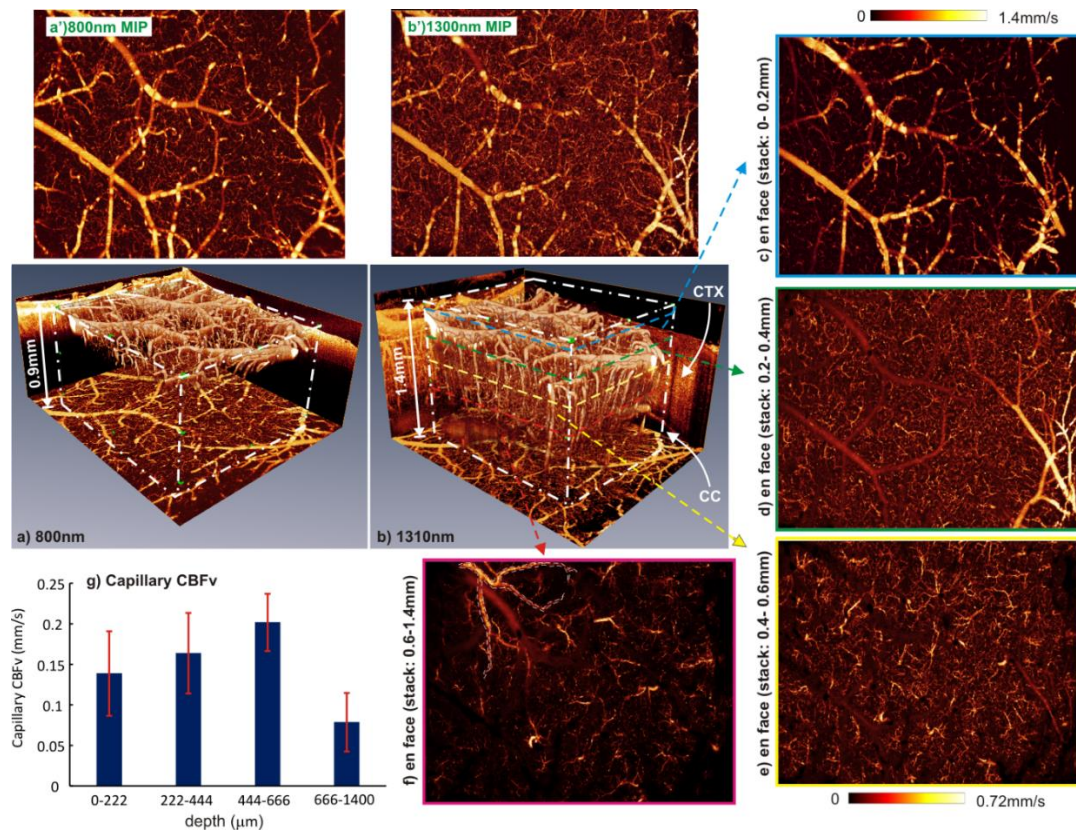
Figure 2-9 *in vivo* 3D CBFv networks on mouse sensorimotor cortex (2.4×2.0mm^2) imaged by 800nm μODT vs. 1310nm μODT. (a, b): 3D rendering to illustrate dramatically enhanced image depth by 1310nm μODT; (a', b'): the corresponding MIP images; (e-f): en-face CBFv images of sub-stack cortex at different depths from 0 -1.4mm; g) capillary CBFv at different depths. CTX: cortex, CC: corpus callosum. Low dose intralipid (0.5mg/kg/h) was given to the animal intravenously (i.v.) as an optical contrast agent to enhance capillary flow sensitivity for panels a) and b).

2.5. Microvasculature heterogeneity

In addition to enhancing the CBFv network image in Figure 2-9, the increased image depth of 1300nm μODT may allow us to analyze microvasculatural heterogeneity in the mouse cortex. Low dose intralipid (0.5mg/kg/h) was given to the animal via intravenously for flow contrast enhancement. Thus, cortical microvasculature was imaged by contrast enhanced μODT (c-μODT) which allows for high SNR and less shadow effects for quantifying capillary density, especially at the deep cortical area.   shows a side view of 3D image of cerebrovasculature on mouse sensorimotor cortex (a: 2.0×0.5 ×1.4mm^3). Interestingly, large pial vessels aligned along the cortical surface as well as those perpendicularly penetrating downward are readily seen and highlighted with light-blue arrows.

Also, the capillary beds were distributed highly heterogeneously in different cortical layers. To quantify the density distribution of the microcirculatory vessels, capillary skeletons were extracted automatically based on a distance map (e.g., $\phi<10\mu m$) in the MIP image so that the fill factor (FF) defined as

$$FF = \frac{pixel \,\#\,of\,microvasculature}{pixel \,\#\,of\,total\,ROI}$$

excluding those occupied by large vessels was computed to characterize the capillary density [ref]. The right panel plots the result, which shows that the capillary fill factor first increased from 0-400µm (layers I-III), reached plateau within 400-700µm, and then from 700-1200µm it gradually became sparsely populated as approaching the deeper areas (layers V-VI and below). This type of capillary density patterns is consistent with the TPM measurement previously reported [ref]. The combined merits of quantitative flow imaging and large FOV that covers the full-thickness cortical CBFv networks may place the new 1310nm µODT technique uniquely well suited for various brain functional studies.
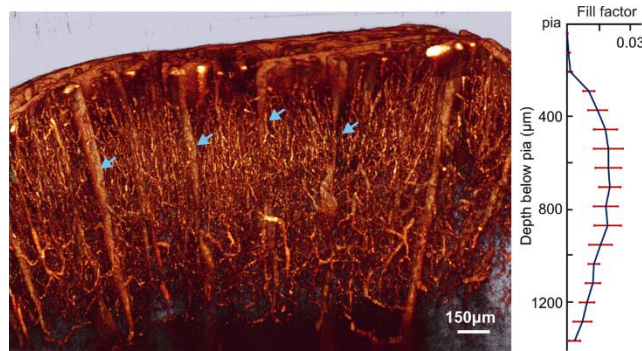
Figure 2-10 3D cerebrovasculature of mouse sensorimotor cortex (2.0×0.5 ×1.4mm3) acquired by 1310nm contrast-enhanced µODT. Right panel: statistical distribution of microvasculature density (fill factor) as a function of depth below the cortical surface. Arrows: penetrating pial vessels.

2.6. Cocaine-induced depth-dependent brain dysfunction

To validate the utility of 1310nm µODT for quantitative monitoring depth-dependent brain dysfunction, we performed CBFv imaging studies on the sensorimotor cortices of C57BL/6 mice after repeated cocaine exposure (30mg/kg/each, intraperitoneally). Different from the procedures described above, two 3×3mm2 cranial windows were created on the sensorimotor cortices of both hemispheres to correlate abnormal behaviors with local cerebral hemodynamic dysfunction of the mice.
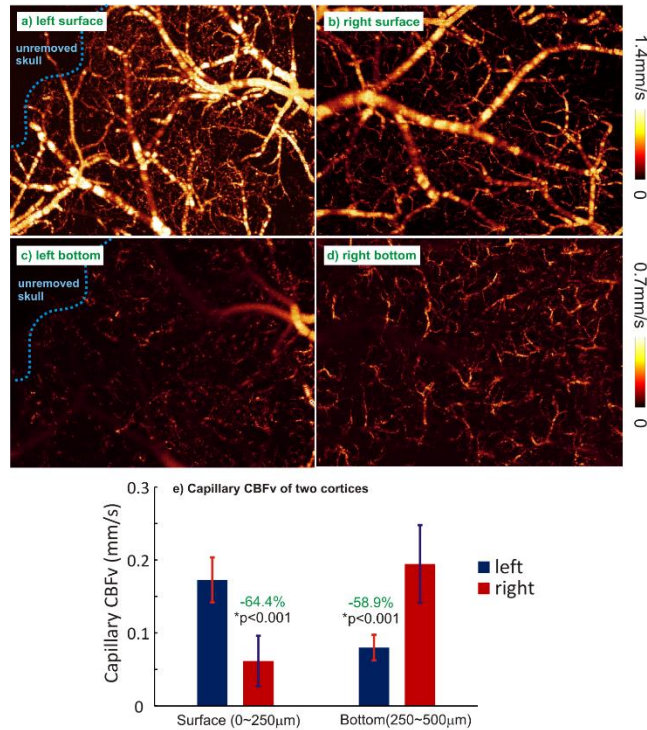
Figure 2-11 In vivo CBFv images of left and right sensorimotor cortices of a mouse after repeated cocaine exposures (30mg/kg, i.p.) acquired by 1310nm μODT. (a, b): upper cortices, (c, d): deeper cortices. e): Statistic comparison of capillary CBFv between left and right cortices.

Figure 2-11 compares the CBFv images of sensorimotor cortices on both left and right hemispheres of a mouse undergoing transient ischemic attacks as a result of repeated cocaine exposures. Interestingly, the upper panels show that CBFv (mostly large pial flows) in the upper left cortex (a) was much higher than that of the upper right cortex (b); whereas lower panels were the opposite, i.e., the microvascular CBFv in the deeper left cortex (c), CBFv was dramatically lower than that of the deeper right cortex (d). This was confirmed by the statistical analysis in Figure 2-11 In vivo CBFv images of left and right sensorimotor cortices of a mouse after repeated cocaine exposures (30mg/kg, i.p.) acquired by 1310nm μODT. (a, b): upper cortices, (c, d): deeper cortices. e): Statistic comparison of capillary CBFv between left and right cortices.(e) that the mean CBFv in the upper right cortex was 64.4% slower than the upper left cortex; the mean CBFv in the deeper left cortex was 58.9% slower than the deeper right cortex. The unbalanced microcirculatory CBFv between the left and the right sensorimotor cortices was likely associated with the observed transient cerebral palsy (paralyzing left paws). Although more study needs to be done, our previous work [28] on cocaine-elicited microischemia tends to suggest that local blood supply deficit (e.g., decreased capillary CBFv) in mouse sensorimotor cortex elicited by repeated cocaine might likely contribute to cerebral palsy.

3. Conclusions and discussions

In summary, we present 1310nm μODT to enhance quantitative 3D imaging of cerebral blood flow networks. In this new system, an ultra-broadband superluminance diode provides high axial resolution and a custom spectrometer was designed for acquiring the interference signal within the spectral range of 1176-1420nm. Additionally, a custom GUI software powered by GPU parallel computing and circular buffer was designed to improve data processing and acquisition speed.

Sensitivity roll-off is one of the important characteristics that determines µODT's imging depth. Although imaging depth is ultimately determined by the scattering properties of brain tissue and the total output power, the optimized sensitivity roll-off can proivde superior SNR in the deep cortical area. Theoretically, spectrometer's sensitivity roll-off is contributed by both finite pixel size and optical performance of the objetive lens. Without considering the optics, system sensitivity only drops 7.8dB at the maximum imaging depth when the Nyquist frequency of the line array camaera is applied[59]. However, in the pratical case, our spectrometer gave the sensitivity drop about 25dB at the maximum depth according to our measurement, worse than the theoretical calculation. The limited objective NA may lead to the enlarged spot size and aberration loss due to the objective lens group may further enlarge the spot which therefore worsen the system's resolving capability for high frequency interference pattern[59]. Although there still exists profound improvement room towards the theoretical performance, the measured results of our spectrometer are comparable to the reported results by other groups[60, 61]. Futhermore, our spectrometer is capable of imaging up to 1.5mm with only -10dB sensitivity loss which is sufficiently deep for imging mouse cortex whose maximum thickness does not exceeed 1.2mm[62].

Utilization of GPU parallel computing is increasingly popular for OCT real-time imaging owing to its superior processing speed over CPU[63, 64]. Taking advantage of GPU computing power, image processing speed for µODT image was significantly improved by more than 50 times (2000 A-line/B-frame) compared to CPU computing. In addition to the improvement of processing speed, data acquisition speed was also optimized by the aforementioned circular buffer memory structure. Different from the "snapping" buffer structure in which only one buffer of a single B-frame was repeatedly overwritten and long latency (~0.06s) of initialization for each frame acquisition added penalty to its frame rate, the circular buffer structure circumvents the low frame rate of sequential processing by initializing once before the start of data acquisition and separating data acquisition from image reconstruction thread. Therefore, data acquisition speed is solely determined by the scanning pattern and hitting theoretical frame rate e.g. 146.67fps while the snap buffer only provides 16.13fps about 9 times slower. However, it is possible that data acquisition speed is faster than data processing speed which may cause the delayed B-frame rate since data acquisition thread waits for the incompletes processing. To solve this problem, large circular buffer array is stongly recommended e.g. 16GB.

In vivo mouse brain validation studies demonstrate the utility of 1310nm µODT for effectively increasing the depth for quantitative 3D imaging (not angiography) of the capillary CBFv networks from ~300µm of prior 800nm µODT to ~1.4mm. Such technological capability is crucial for functional brain studies, because it enables us to quantitatively characterize the CBFv networks across the entire cortex (I-VI layers) and their dynamic, yet highly heterogeneous changes in response to brain activation, as well as the associated downstream behavior patterns. For instance, the new technique allows us to identify the correlation of repeated cocaine-elicited transient cerebral palsy with the flow redistribution across different cortical layers and the resultant unbalance in microcirculatory CBFv networks between the left and right sensorimotor cortices. Future work will focus on optimizing flow detection sensitivity and spatiotemporal resolution for various brain functional studies.

3. Improved capillary flow sensitivity by optical contrast agent: intralipid

The tight coupling between neuronal activity and cerebral blood flow (CBF) ensures that the blood supply meets the energetic needs of neurons and glia that are required for cerebral function and its disruption results in pathology [65-67]. This coupling serves as the basis for most imaging technologies currently used to study the function of the human brain [68-70]. Although two-photon microscopy (TPM)[71-73] enables the measurement of blood vessel diameters and RBC velocities in capillaries at ~300μm below the cortical surface, its small individual FOV (i.e., needed to scan few adjacent vessels for quantifying their RBC velocities) limits its ability to map the heterogeneity of microvascular network responses associated with regional functional brain activation [65].

Recent advances in optical coherence domain technologies [18, 30, 32, 74] permit *in vivo* 3D visualization of cerebrovascular networks (i.e., arterioles, capillaries and venules) and quantitative CBFv imaging of individual vessel compartments (of various diameters) over a large FOV (e.g., a volume of $2\times3mm^2$ with >1mm of depth). However, μODT requires ultrahigh phase stability for measuring slow v_{RBC} and suffers from poor sensitivity at capillary beds[74], which is crucial for studying not only neurovascular coupling (e.g., brain functional activations with specific stimulations) but also neuropathology that involves capillary disruptions. To address this limitation, we present a viable solution termed 'contrast-enhanced μODT' (c-μODT), which is based on the intravenous injection of an intralipid solution (e.g., a highly scattering lipid emulsion) that dramatically improves the detection sensitivity for quantitative 3D CBFv imaging of capillary networks. We show the principles that underlie the sensitivity enhancement for quantifying capillary v_{RBC} by c-μODT with intralipid. Then, we illustrate the value of c-μODT for quantifying capillary v_{RBC} in the mouse brain in three different models: one applied to study a tumor's microenvironment in the brain, one applied to study ischemia triggered by chronic cocaine, and one applied to study microcirculatory responses to physiological (mild hypercapnia) and pharmacological (cocaine) challenges.

1. Methods
    1.1. Animal preparation

Mice were anesthetized with inhalational 2% isoflurane (in 100% O_2) and mounted on a custom stereotaxic frame to minimize motion artifacts. A ~ϕ5mm cranial window was created above the right sensorimotor cortex. The exposed cortical surface was immediately covered with 2% agarose gel and affixed with a 100μm-thick glass coverslip using biocompatible cyanocrylic glue. The physiological state of the mice, including electrocardiography (ECG), respiration rate and body temperature, was continuously monitored (SA Instruments, NY). Mild hypercapnia was induced by swithching inhaled O_2(100%) to a mixture of CO_2 (5%) and O_2 (95%). A mouse tail vein was cannulated with a 30-gauge hypodermic needle connected to PE10 tubing, through which either a 100μl bolus of cocaine (2.5mg/kg, body weight) was rapidly injected (<15s) or a bolus of 20% Intralipid® (6ml/kg, body weight) was injected (30-60s). The physiology and blood gas of mouse were measured. Blood samples were acquired for hematological analysis.

1.2. Optical instrumentation

As illucidated in Figure 3-1, custom ultrahigh-resolution optical coherence tomography (μOCT) system which acquired 3D cross-sectional images of cortical brain architectures characterized by their backscattering properties at near real time and over a large FOV (e.g., $2\times2\times1mm^3$) through the cranial window (Figure 3-1), and applied post-image processing[28] to render μOCA and quantitative μODT images of the cerebral microcirculatory networks *in vivo*. Because of contrast enhancement by intralipid, the line scan rate in this study was increased from previously 5kHz to 20kHz.
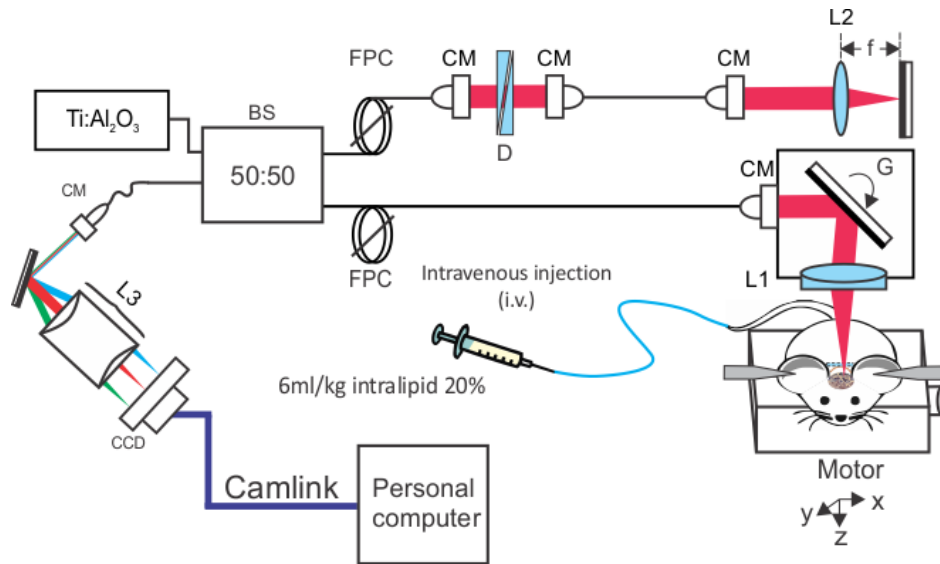
Figure 3-1 Schematic diagram of 800nm SD-OCT system. BS: beam splitter, CM: Collimator, FPC: Polarization controller, G: Galvo scanner L1: Sample arm objective, L2: Reference arm lens, L3: Detector lens group, D: dispersion compensation prism pairs. 6ml/kg 20% intralipid is given to animal via intravenous injection.

2. Results
2.1. Principle of c-μODT for enhancing capillary CBFv imaging

The principle by which intralipid injection increases the sensitivity for μODT to measure CBFv in the capillary beds is illustrated in Figure 3-2, in which 3D μODT images of a mouse cortex before and after intralipid injection are shown in panel a) and panel b), respectively. The cross-section of a ~ϕ7μm capillary at position P was chosen to perform particle-counting μODT (pc-μODT)[75], and the results are plotted in panel c). It is noteworthy that pc-μODT operates in a similar manner to TPM for capillary vRBC quantification in that the former measures the time-lapse Doppler phase transients upon which a RBC passes through a capillary cross-section[75] whereas the latter measures that of the fluorescence intensity profile (i.e., of fluorescence-labeled RBCs). Without intralipid, the phase transients (red trace) show discrete spikes, which reflect the passing of

individual RBCs. The measured RBC velocity by µODT (vRBC=0.25±0.06 mm/s; panel a) is 3-fold lower than that by pc-µODT (vRBC=0.78±0.28 mm/s; panel c). This underestimation of vRBC by µODT is due to various artifacts (e.g., Doppler angle effect), among which the long latency (γ: percentage of duration without the crossing of RBCs) between the transport of RBCs through a capillary was a major error source. For instance, $\gamma \approx 77\%$ in this case, which led to an underestimation of $\eta=(1-\gamma) \approx 23\%$. On the other hand, with intralipid (0.15cc/20mg, i.v.), the phase transients (blue trace) become continuous, as a result of the latency being largely filled with smaller intralipid scatterers flowing through the capillary along with the RBCs. For continuous flow, pc-µODT for vRBC computation is no longer applicable, yet this method corrects vRBC underestimation and provides a ~4.3-fold (i.e., $1/\eta$) contrast enhancement on µODT for imaging capillary flow. Interestingly, vRBC measured by µODT with intralipid (0.53±0.07 mm/s; panel b), although providing a 2-fold enhancement to that without intralipid, was still lower than that of particle-counting µODT (0.78±0.28 mm/s; panel c). This could be caused by uncorrected Doppler angle effect in µODT; it could also be caused by insufficient filling of scatterers for the dose of intralipid injection used, which led to residual spikes as seen in the phase transients. Additionally, we assumed that the scatterers of intralipid flew at the same speed as the RBCs.
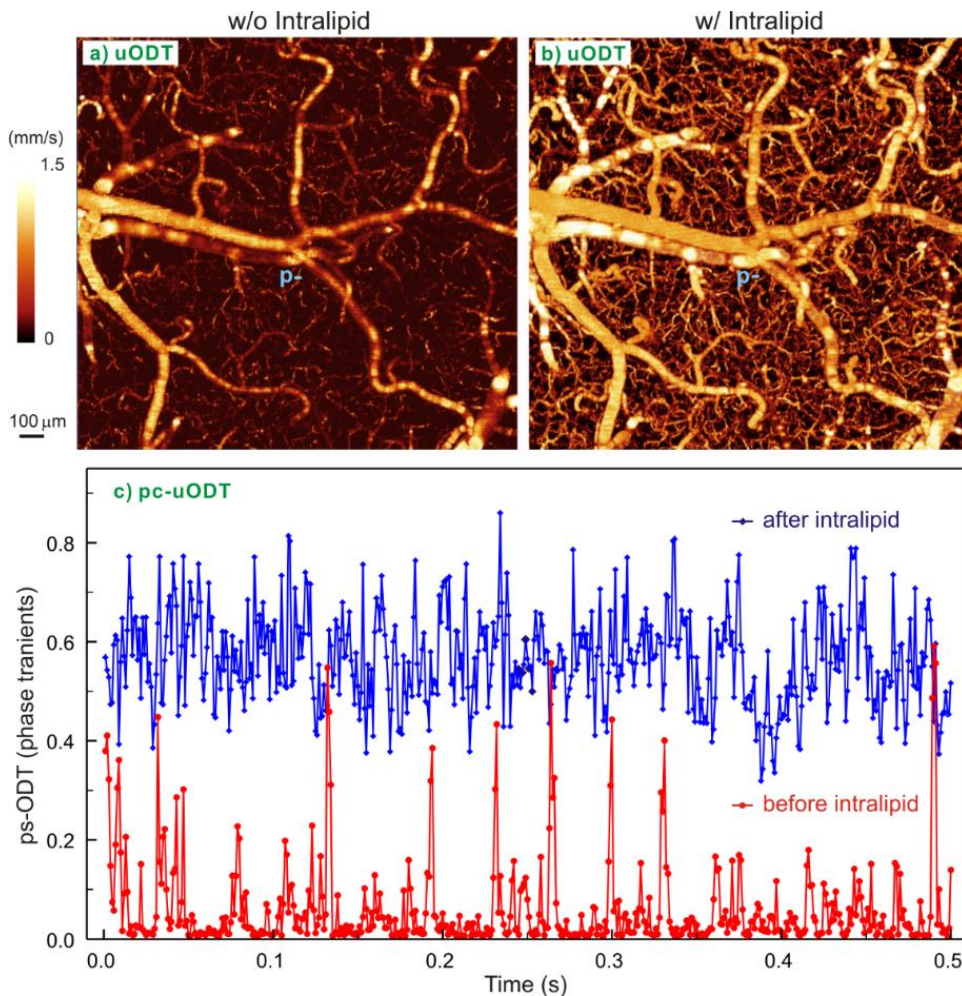
Figure 3-2 RBC velocities vRBC across a capillary vessel (CV: φ7 m) before and after Intralipid injection. a)–b) μODT images of themouse sensorimotor cortex ($2 \times 2 \times 1mm3$), in which a capillary (p) was chosen for pc-μODT to measure RBC velocity along the capillary during baseline and after Intralipid injection, respectively (duration: 0.5 s). c) Time traces of the phase transients. Without Intralipid (red curve), phase spikes induced by the crossing of individual RBCs (n= 16) were recorded and thus vRBC = 0.78 ± 0.28 mm/s was calculated. With Intralipid (blue curve), Intralipid scattering filled the latency between RBCs, thus resulting in an elevated phase trace. The measured total duration occupied by RBC spikes was ~0.12 s (i.e., 0.12 s/0.5 s = 23%) with the 50 s recording time, the long latency (0.38 s) led to severe vRBC underestimation (67%) by μODT. This error was effectively corrected by contrast-enhanced μODT with Intralipid (blue curve)

2.2. Intralipid to enhance microangiography and quantitative capillary CBFv imaging

Figure 3-3 compares 3D μOCA and μODT images of microcirculatory networks on the cortex of a mouse brain at baseline before (upper panels) and after intralipid injection (lower panels). The dramatic improvement with intralipid injection is apparent when comparing the μODT images in panels (d, f) vs panels (c, e), in particular for flow detection in capillary beds. To quantify these differences, we applied digital image processing to segment the flow boundaries after excluding the regions occupied by large branch vessels. We defined the fill factor (i.e., # pixels occupied by capillaries / # pixels in the entire region excluding large vessels) to statistically assess the detectable capillaries (μOCA) and capillary flows (μODT). Panel (g) shows that, while the fill factor of μOCA increased significantly (17.5%; p<0.002, n=20) from 53.74%±4.4% to 63.17%± 3.67% after intralipid injection, it was the increases in μODT that was most dramatic (230%; p<0.001, n=20) from 17.63%±4.76% to 58.21%±8.75%. This indicates that the major impact of contrast enhancement by intralipid is on quantitative Doppler flow of capillary networks (μODT), which is technically more challenging because of the abundant background phase noises induced by biological tissue *in vivo* and by the imaging system[28, 53]. Noteworthily, after intralipid injection, the fill factor of μODT was raised to approach that of μOCA (p=0.14), suggesting that c-μODT for Doppler flow detection has reached the sensitivity of μOCA. This is important because it provides a method for assessing shunting of capillaries with much higher accuracy and without confounds from background and system noise artifacts.
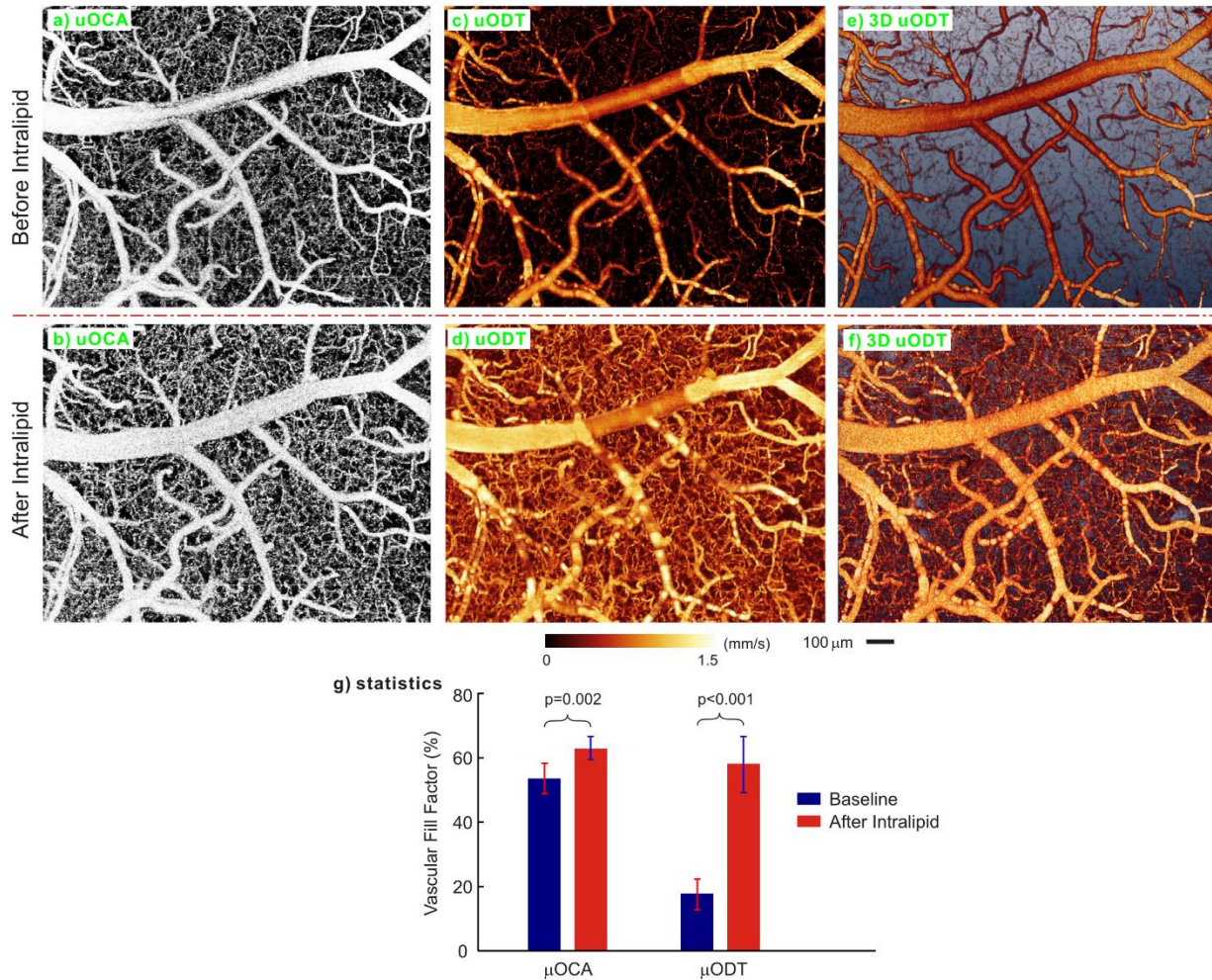
Figure 3-3 Comparison of cerebral vasculature and CBFv on the mouse sensorimotor cortex before (upper panels) and after (lower panels) intravenous injection of 20% Intralipid (6ml/kg). a),b) Maximum intensity projection (MIP) images of vasculature (μOCA); c)–d) MIP images of quantitative CBFv (μODT); e)–f) 3D μODT images. g) Capillary density (fill factor) detected by μODT increased significantly from 17.63% to 58.21% (p<0.001, n = 20), which almost reached the sensitivity of μOCA (63.17%; p = 0.14). Image size (FOV): $1.4 \times 2 \times 1$ mm^3.

2.3. Intralipid to enable quantitative imaging of CBFv change in response to mild hypercapnia

Since c-μODT provided detection of higher capillary flows at baseline, we wanted to ensure that it had the capability for quantifying further increases in CBFv (rather than saturated as imaged by μOCA), for example, in response to hypercapnia. Hypercapnia has been widely utilized to increase CBFv and thus was used as an intervention to compare ODT responses without and with intralipid enhancement.

The left panels (a, d) and the right panels (e, h) in Fig.5 are the en-face and side-view 3D μODT images (FOV: $1.2 \times 0.5 \times 1 \text{mm}^3$) obtained to assess hypercapnia-induced CBFv increases (i.e., $\Delta \text{CBFv} = \text{CBFv}_{\text{hypercapnia}} - \text{CBFv}_{\text{normocapnia}}$) without and with intralipid injection, respectively. A comparison in Panels (j, l) indicates that despite the higher baseline CBFv with intralipid (l), hypercapnia further increased CBFv from 0.49±0.13mm/s to 0.65±0.13mm/s whereas without intralipid (j) it changed from 0.27±0.08mm/s to 0.35±0.10mm/s. Interestingly, the relative change of ΔCBFv was similar with (32.1%) and without (30.8%) intralipid (p=0.51, rank sum test). This result indicates that contrast-enhanced μODT with intralipid preserves quantitative detection of further increases in CBFv even when baseline flows are much higher than without intralipid, which indicates that they are not saturated.
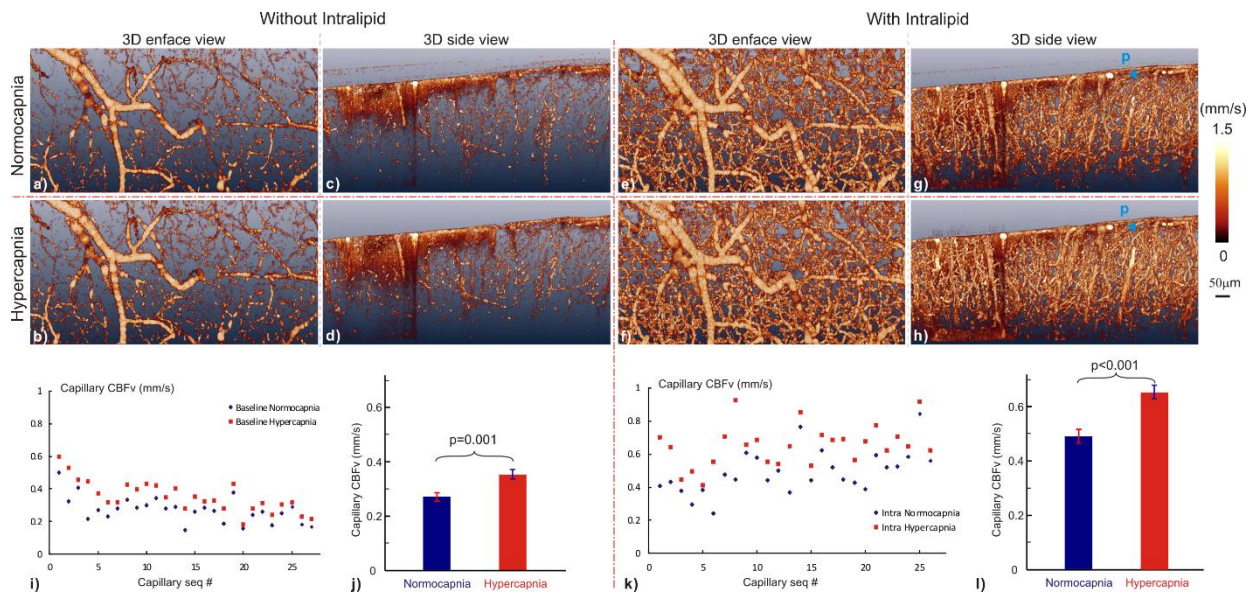
Figure 3-4 Mild hypercapnia elicited CBFv changes on themouse sensorimotor cortex without (left panels) and with (right panels) Intralipid (6ml/kg, i.v.). Upper/lower panels: normocapnia/hypercapnia. a)–h) En-face/side-view 3D images ($0.5 \times 1.2 \times 1 \text{ mm}^3$) of CBFv rates acquired by 3D μODT at 20 kHz. i)–l) CBFv rates (blue/red dots: normocapnia/hypercapnia) from 27 randomly selected capillaries and the corresponding statistical analyses without and with Intralipid, respectively. Hypercapnia-elicited capillary ΔCBFv increases were well correlated (p = 0.51) without (30.8%) and with (32.1%) Intralipid though absolute CBFv increases were significantly higher (p<0.05) with Intralipid (0.16 mm/s) that without Intralipid (0.08 mm/s).

2.4. Intralipid to enhance in vivo imaging of ultraslow CBFv in brain tumor

microenvironments

Tumor tissue usually associates with the appearance of hypoxia and thus shortage of blood flow supply. c-μODT is highly suitable for detecting such ultra-slow flow in tumor microenvironment. To illustrate this, a xenograft tumor model was used, based on implantation of HT1080-GFP cells in the brain cortex of immunodeficient mice. Due to the extremely low CBFv in the area surrounding the tumor, μODT without intralipid (a) failed to detect any capillary flow; whereas

after intralipid injection (b) it clearly showed capillary CBFv networks in the region adjacent to the tumor, which was distinct from the area within the tumor where flow was even lower. These results taken together with those obtained with hypercapnia suggest that the intralipid method is particularly useful for the detection and quantification of very slow flows as may occur within and adjacent to brain tumors.
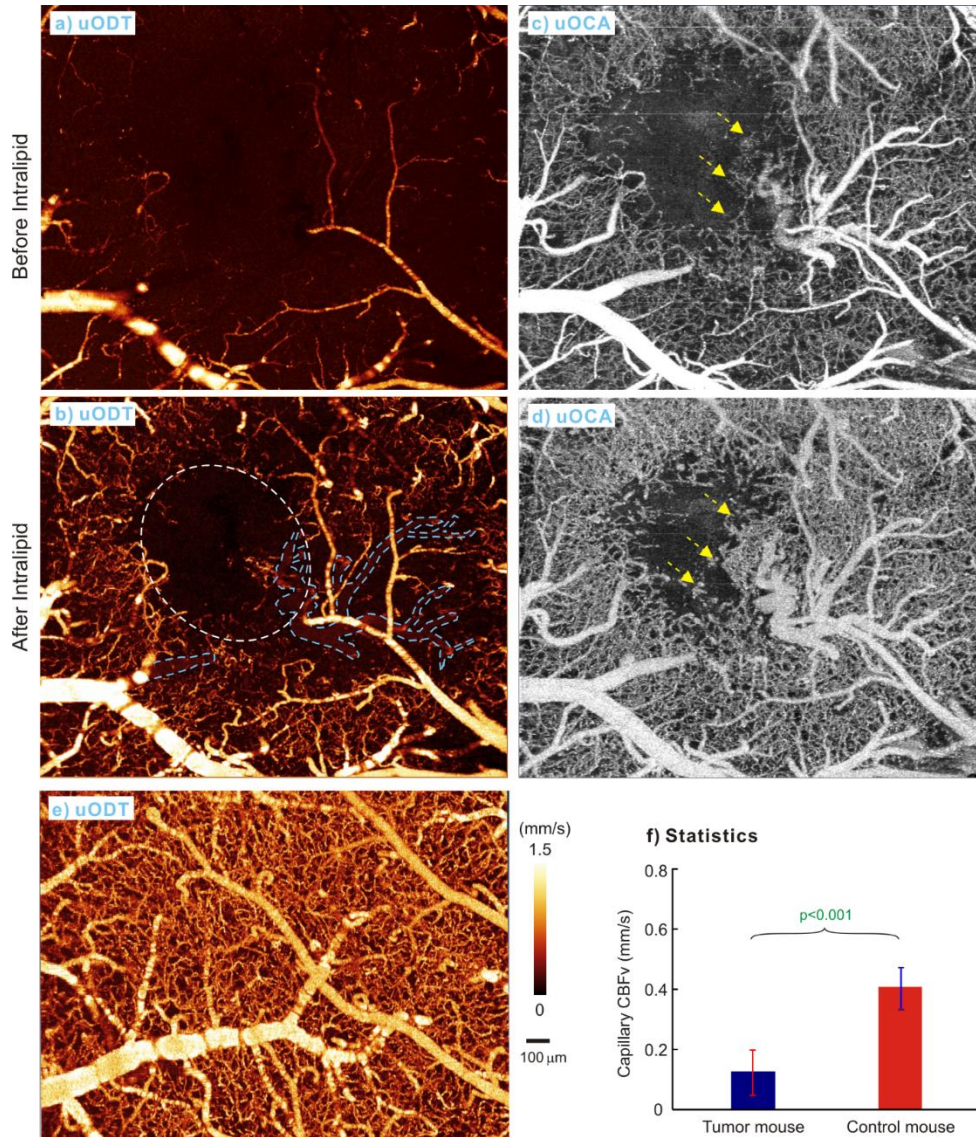
Figure 3-5 Quantitative CBFv and microvasculature images of the mouse sensorimotor cortex on day 16 after intracranial implantation of HT1080-GFP cells. a)–b) μODT images before and after Intralipid injection; c)–d) corresponding μOCA images; e) μODT image of a control mouse (without tumor injection) after Intralipid injection; f) capillary CBFv surrounding the tumor (0.12 ± 0.08 mm/s; n = 20) was 71.4% lower (p b 0.001, rank sum test) than that of control (0.42 ± 0.07 mm/s). White dashed area: tumor margin outlined based on disrupted CBFv, yellow arrows: vascular ingrowth with ultralow CBFv (0.04 ± 0.02 mm/s) from adjacent brain region, and blue dashed regions: collateral arterioles with ultralow CBFv (0.10 ± 0.03 mm/s). Image size: $2 \times 2 \times 1$ mm^3.

2.5. Intralipid to enhance in vivo imaging of ultraslow CBFv in chronic cocaine mice

c-μODT is also highly suitable for *in vivo* imaging of durg (e.g. cocaine) induced cerebral flow disruptions, owing to its ultrahigh sensitivity/resolution and large FOV. Fig. ?? shows 3D CBFv images on the sensorimotor cortex of mice after chronic cocaine administration and in control mice before and after intralipid injection. The CBFv images without intralipid showed that the mouse exposed to chronic cocaine (a) when compared to the control mouse (c), showed widespread vasoconstriction throughout the FOV ($1.9 \times 1.5 \times 1 mm^3$). Due to the extremely low CBFv in the chronic cocaine mouse, μODT without intralipid (a) showed areas of the cortex where almost no capillary flow could be visualized or measured; whereas after intralipid injection (b) it clearly uncovered capillary CBFv in areas that otherwise could not be detected and similarly enhanced the measurement of venular flows (e.g., dashed yellow lines). This reveals therefore that while chronic cocaine dramatically reduced capillary flows it did not abolish them, which would otherwise have led to ischemia and neuronal death. Quantitative analysis reveals that without intralipid the measured overall capillary CBFv in the chronic cocaine mouse (a) ($0.110 \pm 0.027 mm/s$, among which background phase noise v_n was $0.083 mm/s$) was significantly reduced (69.5%; $p < 0.001$, n=20) compared to that of the control mouse (c) ($0.230 \pm 0.058 mm/s$, $v_n = 0.148 mm/s$). It is noted that here the net change with subtraction of background v_n is computed, e.g., $[(0.230-0.148)-(0.110-0.083)]/(0.230-0.148)=69.5\%$. After intralipid, the measured overall capillary CBFv in the chronic cocaine mouse ($0.240 \pm 0.062 mm/s$, $v_n = 0.083 mm/s$) was $(0.240-0.083)/(0.110-0.083) \approx 8.6$ times higher than that measured without intralipid and readily detectable with dramatically enhanced SNR (b). These results suggest that c-μODT with intralipid is particularly useful for the detection and quantification of ultraslow flows as may occur in ischemic brain (e.g., due to chronic cocaine or other substances of abuse).

2.6. Intralipid to enhance spatiotemporal resolution of CBFv for functional brain imaging

As the phase shift detected by μODT is proportional to its time duration, c-μODT allows to reduce the time for 3D imaging of capillary CBFv networks and thus improve the temporal resolution for studying dynamic brain responses to functional and physiologic activation. Fig.?? shows the spatiotemporal changes in CBFv (i.e., 4D c-μODT) following an acute cocaine injection (2.5mg/kg, i.v.). Owing to contrast enhancement of the capillary networks with the image rate of μODT was increased by 4 times (i.e., with A-scan rate was increased from 5kHz in the previous study[28] to 20kHz), which enabled us to quantify cocaine-induced dynamic CBFv changes (b) in vessels of different calibers at a higher temporal resolution and over a larger FOV (e.g., $1 \times 0.35 mm^2$ per panel). Dynamic characteristics (c) were readily observed, including an immediate sharp CBFv increase (injection surge, first 1.5min) followed by CBFv decreases in most of the microcirculatory networks and their slow recovery starting at ~8 minutes post-injection in some vessels but not in others. The pattern of CBFv changes in venules (blue curves) was consistent (i.e., decreases in CBFv following cocaine injection) whereas in arterioles (red curves) it varied: some showed persistent CBFv decreases, some recovered, and some (e.g., arcade 8) showed CBFv increases perhaps, for local compensation. Capillaries (green curves) reacted to cocaine differently and most exhibited oscillating behaviors. Interestingly, unlike aterioles and venules, which spiked

immediately after injection, some capillaries (e.g., 6) did not spike and abruptly decreased their flow in response to cocaine.
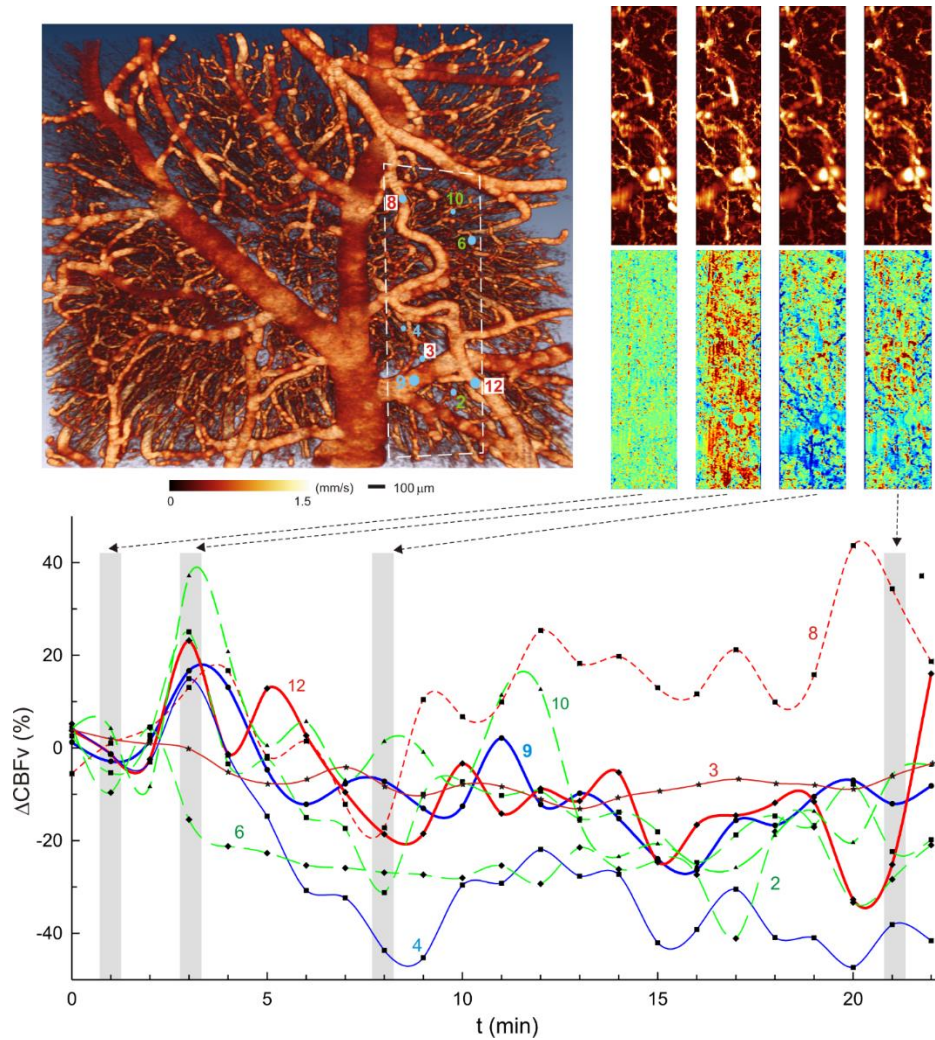
Figure 3-6 Spatiotemporal responses of CBFv to an acute cocaine challenge (2.5 mg/kg, i.v.; t=3 min). a) 3D μODT image ($1.5 \times 1.8 \times 1\text{mm}^3$) to illustrate vascular trees in the selected ROI (dashed area); b) Time-lapse CBFv and ΔCBFv ratio images ($1 \times 0.3 \times 1\text{mm}^3$/panel) at 4 characteristic time points (t: 1, 3, 8, 21 min); c) time-lapse ΔCBFv curves of 2 arterioles (coarse/thin red curves: branch/arcade arterioles), 2 venules (coarse/thin blue curves: branch/terminal venules), and 3 capillaries (dashed green curves). The initial overshooting was caused by artifacts induced by bolus cocaine injection.

3. Conclusions & Discussions

Here we show that contrast-enhanced μODT via intralipid injection dramatically improves the sensitivity for measuring RBC velocities (v_{RBC}) in cerebral capillaries. While μODT was able to image v_{RBC} in the capillary beds, its detection sensitivity was limited, leading to a low fill factor of 17.63%. This contrasts with c-μODT with intralipid injection, which significantly increased the fill factor to 58.21%, almost reaching the sensitivity of μOCA (63.17%). Such a dramatic

sensitivity improvement in quantitative CBFv imaging is crucial for studying vascular disruptions caused by cerebral pathology (e.g., tumorigenesis) and by physiological (e.g. hypercapnia) or pharmacological stimulations (e.g., cocaine exposures). However, we did not test intralipid performance for vasoconstrictors. Endothelin 1 (ET-1), also known as preproendothelin-1 (PPET1), is a potent vasoconstrictor and can be used in our future study to investigate intralipid's quantitative properties in response to vasoconstrictors.

To our knowledge no other current imaging techniques offer such potential (e.g., large FOV, v_{RBC} quantization of CBF on vascular networks of different calibers that include capillaries and arterioles and venules at high spatiotemporal resolutions). Owing to the increased v_{RBC} detection sensitivity, c-μODT also improves the temporal resolution (e.g., 4 times faster - limited by camera frame rate), which is important when monitoring dynamic vascular changes to physiological, functional or pharmacological interventions. Finally, we illustrate that the enhancement is predominantly due to the continuous flow from the intralipid in the capillary streams that obviates the errors from long latency between RBCs, i.e., low hematocrit (~20%) in capillaries (Slow μODT may improve detection of sparse RBCs in a capillary, i.e., v_{RBC} sensitivity -ultimately limited by tissue motion noise, it is unable to avoid low hematocrit induced errors for v_{RBC} quantization).

The increased temporal resolution of c-μODT allows to characterize the dynamic features of microcirculatory networks quantitatively, at capillary flow resolution/sensitivity. For example, our results with the acute cocaine challenge identify for the first time a heterogeneous response among blood vessels in response to acute cocaine that might reflect adaptation responses of the microvascular networks to a vasconstricting drug. Particularly intriguing was the response of arteriolar vessels because while in most vessels cocaine decreased CBFv in a couple of arterioles (e.g., arcade 8) cocaine increased flow, which could reflect a compensation to the widespread reductions in CBFv perhaps as a mechanism to protect the tissue from ischemia. It allowed to statistically analyze the dynamics of CBFv in the vascular tree, i.e., arterioles, venules and capillaries responding to cocaine.

Limitations from the technology include the clearance of the intralipid from blood streams. However, after a single injection high levels are maintained over a 60-min period and no noticeable change is observed in mouse systemic physiology (e.g., ECG, Resp, T, Hct). As study manipulations (e.g. cocaine injection) were performed ~10min after intralipid injection, artifacts such as concurrent blood volume increase were avoided. Moreover, additional continuous slow infusion of low-dose intralipid (e.g., 1mg/kg/hr) could extend the time window for studies that might require longer time measurements, but the influence of the concurrent blood volume increase by intralipid injection should be studied, which can potentially be studied by μOCA. Though in this study we did not evaluate the effects of the intralipid injection itself on brain function, this is unlikely to have side effects since lipid emulsions of similar density to the one employed in our study are routinely used clinically in patients that require intraparenteral nutrition. In our study, we only used 20% intralipid emulsion but further studies will be required to assess the optimal concentration. Although no reduced CBFv imaging depth induced by intralipid scattering was observed (e.g., Figure 3-4(c, g)), more detailed study should be performed. Additionally, intralipid was used in this study to demonstrate the efficacy of contrast-enhanced μODT for quantitative 3D imaging of mouse microcirculatory CBFv networks. This technique

should be applicable to other types of clinically approved total parenteral nutrition (TPN), which also comprise high-scattering lipid emulsions. For example, it could be used intraoperatively to confirm complete aneurysm clipping, which is currently performed by video angiography requiring repeated intravenous doses of indocyanine green (ICG, a fluorescence tracer) adsorbed to human serum albumin. Unlike administration of ICG, which can result in potentially adverse reactions[76], intralipid is safe and clinically available for use in parenteral nutrition. Thus, in addition to its value for research this technique is of translational potential for clinical applications.

4. Using phase summation and continuous angle tracking method to improve μODT dynamic range and decouple Doppler angle artifacts.

The common approach for phase-based optical coherence tomography (OCT) flowmetry [16, 77, 78] was based on the phase subtraction method (PSM) derived by Chen, et al., which reconstructs flow images by measuring the phase difference between successive A-scans [16]. Like any phase-based interference methodology, this method is confronted with two main problems. One is the limited dynamic range due to the 2π periodicity of phase (i.e., ambiguity) or phase ramping [47, 79]. To extend the dynamic range, we showed in our previous work that high flow rate can be retrieved by summing up the number of phase wrapped rings owing to high signal to noise ratio (SNR) of digital frequency ramping method (DFRM) [29]. Importantly, this was the first report of quantitative CBFv imaging from original OCT scan data by solely digital image processing (i.e., no additional phase modulation. e.g., by scanning reference mirror or dense A-scan scheme). Mathematically, the similarity of wrapped and true phase gradient modulo 2π was reported to solve the 1-D phase wrapping issue [80]. However, those approaches were developed to extend dynamic range "upwards" to recover faster flow, whereas the recovery of slow flow (e.g. capillary flow) was neglected, which plays a critical role in neurovascular coupling. Another remaining problem for quantitative CBFv imaging is the Doppler angle coupling that profoundly affects the accuracy of true velocity measurement, especially, when the vessels are oriented horizontally along the cortical surface, resulting in serious underestimation of the flow rates. Therefore, it is of great importance to trace the Doppler angle accurately for retrieving absolute flow velocity.

Several approaches estimated full velocity by introducing transverse velocity based on the Doppler spectrum broadening instead of calculating the phase shift only [33-35, 81]. However, the limited sensitivity for numerical aperture dependent spectrum broadness may restrict the detection of minimal transverse velocity for common low-NA optical systems or may require focal tracking of flows from different depths, i.e., additional imaging time. In addition, more sophisticated ODT systems have been developed with dual or multi-axis detections to potentially improve the estimate of Doppler angles [82, 83].

A phase summation method was introduced to extend the ODT dynamic range downwards (e.g., enhancing the detection of minimal flow, vmin) without sacrificing the upper flow detection range. Continuous vessel tracking and Hessian matrix method were applied to improve the angle ($\cos\theta$) correction and thus the retrieval of true flow velocity. These methods were validated first in an intralipid flow phantom study and then applied to quantify the flow disruption to the rat brain secondary to acute cocaine challenge and to chronic cocaine exposures.

1. Methods
   1.1. Phase summation method

As the phase shift ($\Delta\phi$: [-π, π]) measured by Doppler flowmetry is a product of flow velocity (ν) and time duration (T)[16], i.e.

$$v = \frac{\lambda_0 \Delta\phi}{4\pi n T \cos\theta} \qquad \text{Eq. 4-1}$$

where λ_0 is central wavelength, n is refractive index, and θ is the angle between light propagation and the flow direction. The flow detection sensitivity and the dynamic range contradicts to each other (e.g., phase wrapping artifacts). In the previous study, we reported frequency binning (upward, i.e., T→2T, 3T, ...) [28] to effectively enhance the sensitivity for slow capillary flow detection, but this method restrains its dynamic range (causing faster flows to saturate). Here, we present a new downward binning method that enhances the detection sensitivity of minimum detectable flow (v_{min}) without degrading the dynamic range (e.g., reducing phase wrapping threshold). Because of oversampling (commonly used in ODT to improve the phase stability), the spatial separation between two adjacent A-lines is likely as small as a fraction of the lateral resolution, and thus the phase difference (decorrelation) between 2 stationary spots is negligible. Then, the phase shift $\Delta\phi_{2T},z(i)$ between double spaced A-line lines (2T) can be calculated by a summation of phase shifts of 2 adjacent single-spaced A-lines (T), $\Delta\phi T,z(i)$, $\Delta\phi_T,z(i+1)$, using the autocorrelation algorithm [44],

$$\Delta\phi_{T,z}(i) = \arctan\left\{\frac{\text{Im}(A_{i+1,z})\text{Re}(A_{i,z}) - \text{Im}(A_{i,z})\text{Re}(A_{i,+1z})}{\text{Im}(A_{i+1,z})\text{Re}(A_{i,z}) + \text{Im}(A_{i,z})\text{Re}(A_{i+1,z})}\right\}, \quad -\pi \leq \Delta\phi_{T,z}(i) \leq \pi \qquad \text{Eq. 4-2}$$

where Re(Ai,z) and Im(Ai,z) refer to the real and imaginary parts of the i-th A-scan signal after FFT, and

$$\Delta\phi_{2T,z}(i) = \Delta\phi_{T,z}(i) + \Delta\phi_{T,z}(i+1), \quad -2\pi \leq \Delta\phi_{2T,z}(i) \leq 2\pi \qquad \text{Eq. 4-3}$$

This implies that by summing up the successive phase shift $\Delta\phi T(i)$ and $\Delta\phi T(i+1)$, the detectable phase range can be extended to [-2π, 2π] because each A-line pair $\Delta\phi T,z$ contributes a phase range of [-π,π]. The extension of Doppler velocity dynamic range(VDR) results in preserved phase wrapping threshold (v_{wrap}) and a lower (1/2) minimal detectable flow (v_{min}→v_{min}/2), where v_{wrap} and v_{min} are defined by the following equation

$$v_{wrap} = \frac{\lambda_0 \Delta\phi_{max}}{4\pi n T \cos\theta} \qquad \text{Eq. 4-4}$$

$$v_{min} = \frac{\lambda_0 \sigma_{\Delta\phi}}{4\pi n T} = \frac{\lambda_0 (\text{SNR})^{-1/2}}{4\pi n T} \qquad \text{Eq. 4-5}$$

$$VDR[\text{dB}] = 20\log\left(\frac{V_{wrap}}{v_{min}}\right)$$
Eq. 4-6

where $\sigma_{\Delta\phi}$ refers to system phase variance[46]. Also, the decrease of v_{min} to half is a result of the doubled time interval ($T\rightarrow 2T$), and importantly the SNR is preserved by this linear summation algorithm. It is noteworthy to point out the difference of this method from previously reported phase binning method [84] by which, without phase summation Eq. 4-3, the system dynamic range is still limited within $[-\pi,\pi]$ even though the time interval used for phase shift calculation is doubled from T to 2T. Thus limited dynamic range due to doubled time interval could easily cause phase wrapping for high speed flows in the binning method.

1.2. Single vessel angle correction

Since vessels in the cortical brain can be horizontally oriented, angle correction is needed to correct measurement errors. Previously θ correction was implemented by using the upper edge or centroid positions of the flow profile across 2-3 adjacent B-scans (cross-sectional images), this method works reasonably well except for flat vessels where $\theta\approx90°$, which may lead to severe correction errors (i.e., $\cos\theta\rightarrow0$, $1/\cos\theta\rightarrow\infty$ in Eq. (1) for v computation). Here, we apply vessel tracking to numerically approach the flow gradient $\cos\theta_z$. Vessel skeleton is extracted by tracking the centroid of flow cross-section frame by frame which can be discontinuous due to flat angle of flow direction (Figure 4-1(a,b)).
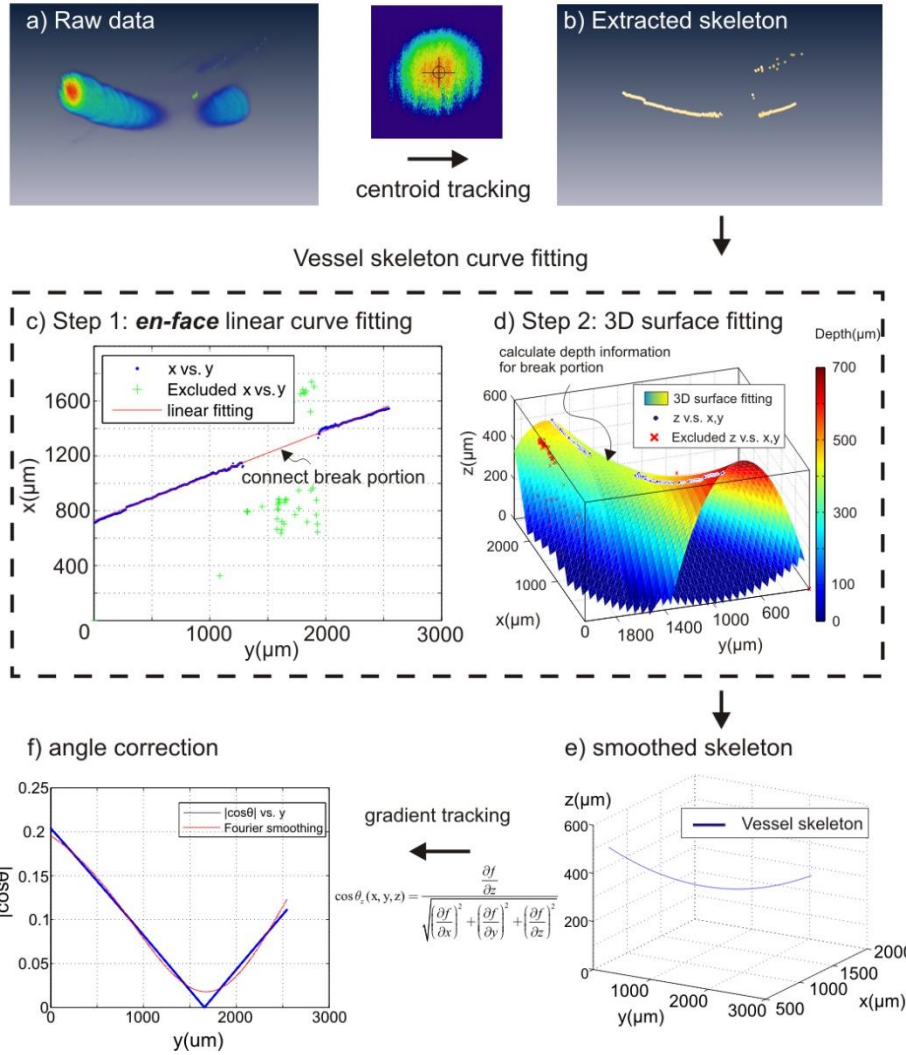
Figure 4-1 Numerical method for vessel tracking and least-squares fitted angle correction. Vessel skeleton (b) was generated by centroid tracking of the raw data (a). 2D (c) and 3D (d) curve fitting was applied to smoothen raw vessel skeleton extracted by centroid tracking technique, i.e., blue dots in (d). As result of two-step fitting, a vessel skeleton f(x,y,z) was obtained in (e). (f): Doppler angle $|\cos\theta_z(x,y,z)|$ was calculated by Eq. 4-9 and further smoothened by Fourier curve (red line) to avoid extreme case when $\cos\theta_z=0$.

It is aimed to obtain a clean and smooth vessel skeleton without a break segment, which can be accomplished by different algorithms. Here we used simple 2-step curve fitting to connect the break segment and further smoothen the vessel skeleton:

Step 1. 2D curve fitting fills the skeleton blank on en-face projection image (x-y plane)(Fig.3(c))

$$x = a \cdot y + b$$

Eq. 4-7

Step 2. Combing a polynomial 3D surface fitting (Figure 4-1(d)) and result of step 1,

$$z(x,y) = p_{00} + p_{10} \cdot y + p_{01} \cdot x + p_{20} \cdot y^2 + p_{11} \cdot xy + p_{02} \cdot x^2 \qquad \text{Eq. 4-8}$$

where p_{ij} (i, j=0, 1, 2) are polynomial coefficient. one can obtain the continuous skeleton function f(x,y,z) in 3D (Figure 4-1(e)). Thus the cosine of Doppler angle $\cos\theta_z(x,y,z)$ can be easily calculated as:

$$\cos\theta_z(x,y,z) = \frac{\dfrac{\partial f}{\partial z}}{\sqrt{\left(\dfrac{\partial f}{\partial x}\right)^2 + \left(\dfrac{\partial f}{\partial y}\right)^2 + \left(\dfrac{\partial f}{\partial z}\right)^2}} \qquad \text{Eq. 4-9}$$

where f(x, y, z) is a 3D skeleton curve and $\partial f/\partial x$, $\partial f/\partial y$, $\partial f/\partial z$ are the gradients with respect to the corresponding axes. At $\theta \approx 90°$, the evaluated $|\cos\theta_z(x,y,z)|$ is further smoothened to avoid $\cos\theta = 0$ by Fourier curve (Figure 4-1(f)). Doppler velocity (v_z) was also tracked by averaging a disk area of radius equal to 10μm at flow centroid, and the true velocity(v_T) was obtained by dividing cosine of Doppler angle, i.e.,

$$v_z = \frac{\lambda_0 \Delta\phi}{4\pi nT} \qquad \text{Eq. 4-10}$$

$$v_T = \frac{v_z}{\cos\theta_z} \qquad \text{Eq. 4-11}$$

1.3. Volumetric Doppler angle correction

Most of conventional method are limited to only correct the Doppler angles of a few large vessels (e.g. MCA) and are unable to calculate $\theta_z(x, y, z)$ of individual micro flows within 3D CBF networks. Here, we propose a method for tracking Doppler angle matrix $\theta_z(x, y, z)$ based on 3D Hessian matrix. Although 2D Hessian filter has been shown to greatly enhance *en-face* microangiographic images,[10] its unique properties to retrieve 3D orientation of tubular object (e.g., blood vessel) is so far neglected. Our method relies on analysis of eigenvalues of 3D Hessian matrix at each pixel whose smallest eigenvector corresponds to the longitudinal direction of a tubular shape.

To retrieve an arbitrary Doppler angle $\theta_z(x, y, z)$ within the entire 3D volumetric μODT image, 3D Hessian matrix $H_{o,\sigma}$ was applied to compute the 2nd-order derivative of a pixel of interest based on its local phase shift variation, i.e.,

$$H_{o,\sigma} = \begin{vmatrix} \dfrac{\partial^2 I}{\partial x^2} & \dfrac{\partial^2 I}{\partial x \partial y} & \dfrac{\partial^2 I}{\partial x \partial z} \\[3mm] \dfrac{\partial^2 I}{\partial x \partial y} & \dfrac{\partial^2 I}{\partial y^2} & \dfrac{\partial^2 I}{\partial y \partial z} \\[3mm] \dfrac{\partial^2 I}{\partial x \partial z} & \dfrac{\partial^2 I}{\partial y \partial z} & \dfrac{\partial^2 I}{\partial z^2} \end{vmatrix}$$

Eq. 4-12

where I(x, y, z) is the raw (apparent) flow value. For a tubular object (e.g., blood flow), $H_{o,\sigma}$ is along the longitudinal (flow) direction shows less change than those along the radial directions, namely, whose λ_1 is smaller than the other two, i.e., $|\lambda_1|<<|\lambda_2|$, $|\lambda_1|<<|\lambda_3|$, and usually $|\lambda_2|\approx|\lambda_3|$. Each eigenvalue corresponds to its own orthogonal eigenvector. For example, the eigenvector v_1 (v_x, v_y, v_z) corresponds to the lowest eigenvalue λ_1 as illustrated in Figure 4-2, thus the longitudinal or the flow direction of individual pixel (x, y, z) within a tubular flow can be represented by the eigenvector v_1. With v_1 extracted from Eq. 4-12, the Doppler angle θ_z(x, y, z) can be readily computed assuming the direction of light is incident along the z-axis.
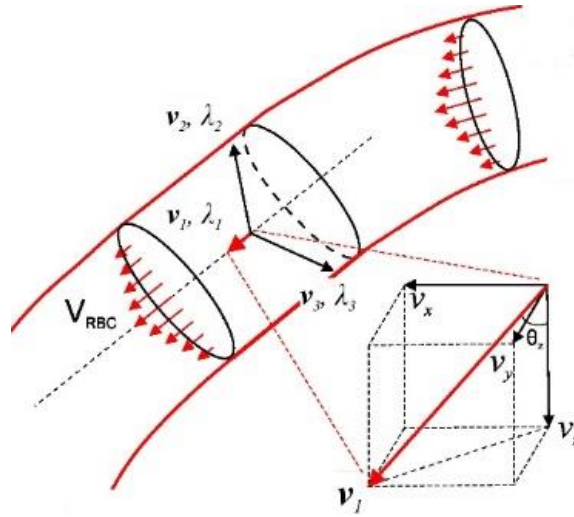
Figure 4-2 A sketch to illustrate Hessian matrix for 3D Doppler angle detection. v_1 is the vector with lowest eigenvalue λ_1 corresponding to the longitudinal direction of tubular vessel.

2. Results
    2.1. Phase summation to enhance CBFv quantification

A flow phantom study using 1% intralipid solution pumped through PE10 tubing (CMA400, Microdialysis) was performed to validate the performance improvement of the phase summation method. Fig.5 shows the comparative results of the phase images reconstructed using 3 different methods for fast flow (15µL/min, or line axial velocity of $v_{max/f}$=0.99mm/s) and slow (3µL/min, $v_{max/s}$=0.19mm/s) flow rates at Doppler angle of θ≈83°. PSM at 10kHz provides the best flow velocity profile and accuracy (0.96mm/s, 96.5% of $v_{max/f}$) for fast flow showing no phase wrapping artifact (a) but suffers poor sensitivity for slow flow (46.9µm/s) (d), even though the system

sensitivity is v_{min}=10.3µm/s (SNR=33.2dB) according to Eq. (5). As a result, only 12% of full dynamic range (π) is detected and the flow profile is barely distinguishable from the background (d). By applying frequency binning to 5kHz as previously reported[28], the detection sensitivity for slow flow increases to 22.1µm/s (e) and the detected phase is doubled to 24.2% of the full range (π), yielding a measured velocity of 0.18mm/s to 93.1% of $v_{max/s}$=0.19mm/s. However, it fails to retrieve the full velocity profile for fast flow (b) because of reduced phase wrapping threshold v_{wrap} Eq. (4) that leads to phase wrapping artifacts. The detected flow rate (0.34mm/s) is severely underestimated, i.e., only to 33.8% of $v_{max/f}$=0.99mm/s. Interestingly, phase summation method preserves the parabolic velocity profile of the fast flow (c) and the measured maximum velocity of 0.91mm/s is 92.5% of $v_{max/f}$=0.99mm/s; meanwhile, it increases the sensitivity for slow flow (f) to the 26.5µm/s (equivalent to that by frequency binning (e)), yielding a measured velocity of 0.20mm/s and phase shift over 27% of the full range (π). Interestingly, its dynamic range as defined by 20log($v_{max/f}/v_{max/s}$) is enhanced by 17.5% in method 3 (30.7dB) compared to method 1 (26dB). More dramatic enhancement (i.e., 30.4%) is found in comparison between method 2 (23.5dB) and method 3 (30.7dB) because of phase wrapping. It should be noted that nonlinear pseudocolor map was applied in method 3 to project the extended phase range [0, 2π] onto [0, π] for comparison purpose.
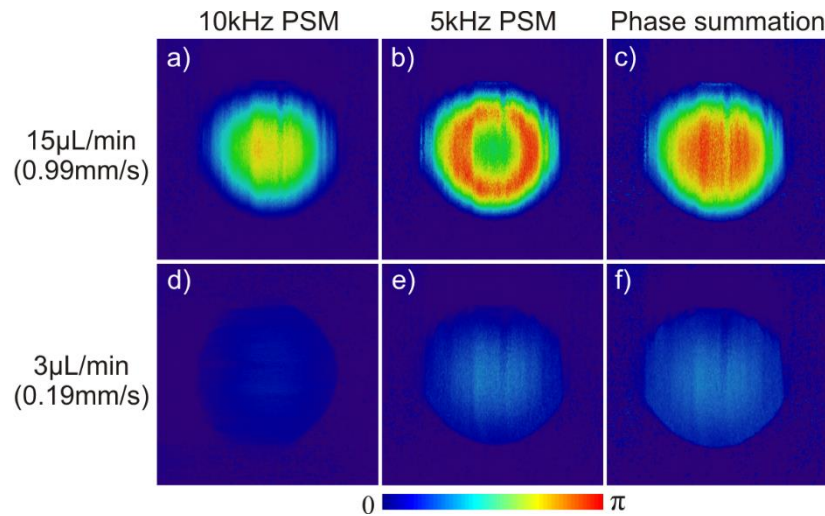
Figure 4-3 Phantom flow study (1% intralipid, ϕ280µm tubing) to demonstrate that phase summation method enhances the sensitivity for slow flow detection and increases the dynamic range for fast flow detection. All images are projected onto same phase scale [0,π] for comparison.

2.2. Angle correction by gradient tracking method

Gradient vessel tracking method improves the accuracy of ODT for CBFv quantification. A phantom flow study was performed with 1% intralipid pumped at a constant flow rate of 20µL/min or equivalently v_{max}=10.8mm/s in ϕ280µm micro tube. Assume that the phantom follows laminar flow phenomena, then its velocity distribution is characteristic of a parabolic profile that obeys[85]:

$$v(\mathrm{r}) = v_{max}(1 - \frac{r^2}{R^2}) = \frac{2F}{\pi R^2}(1 - \frac{r^2}{R^2})$$ Eq. 4-13

where F is the instantaneous flow rate of the cross-section, R is radius of the inner surface of the micro tube and r is distance away from flow centroid. Fig.6 compares the images of the raw flow profile reconstruction by PSM (a), velocity-smoothened flow profile before (b) and after (c) angle correction using our vessel tracking method. The corresponding cross-sectional flow velocity profile at $\cos\theta=0$ was plotted in the inset of each image. The corresponding maximal velocity (v_{max}) profiles on flow centroid are plotted in panels (d). The v_{max} measurement accuracy after angle correction using gradient vessel tracking approach is dramatically increased by ~11.5 fold from 8.0% (0.86±0.60 mm/s) to 91.3% (9.86±0.94 mm/s) of the theoretical v_{max}=10.8mm/s (note that the underestimation could be induced by v_{max} itself which sis theoretically derived rather than measured). It is noteworthy that gradient vessel tracking method shows superior performance over previous 2- or 3- point correction method with 6.1-fold improved accuracy from 14.9% (1.60±1.43mm/s, 3-point correction) of v_{max}. This method also yields much improved measurement precision, i.e., the coefficient of variation (i.e., CV=standard deviation/mean) of the measured velocity was 9.3-fold smaller, from CV=0.89 (3-point method) down to CV=0.096 (gradient vessel tracking).
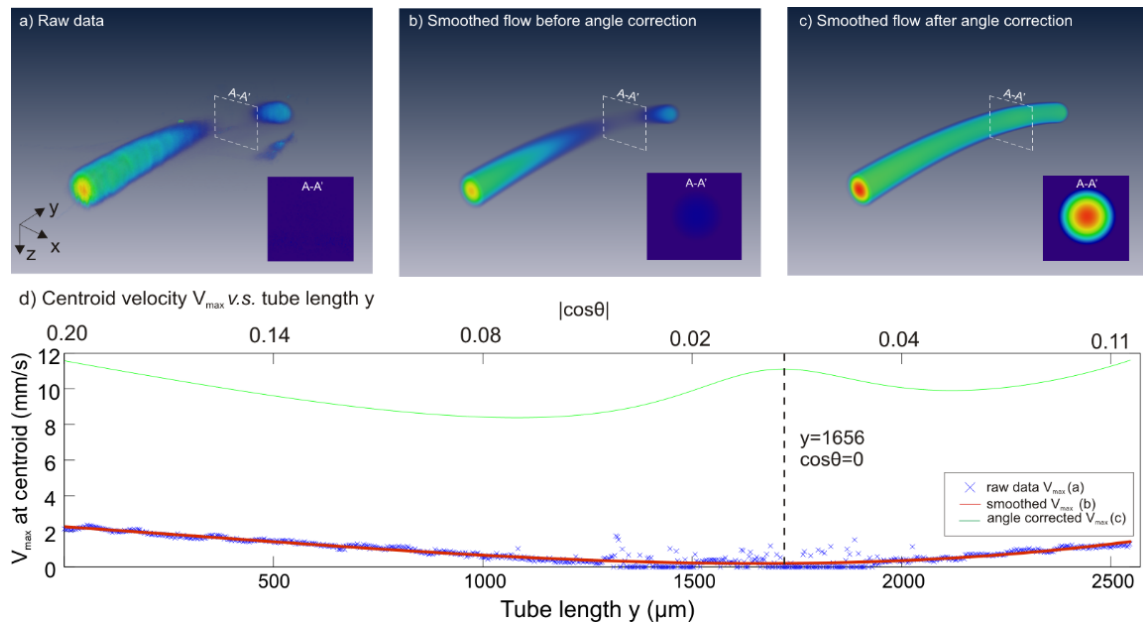
Figure 4-4 Results of flow phantom study (1% intralipid, ϕ280µm tubing) to show that angle correction using gradient vessel tracking dramatically ~9.3-fold reduces the error in flow rate quantification.

In addition to phantom validation, gradient vessel tracking was used to retrieve the absolute CBFv within individual branch vessel along a vascular tree by continuously correcting $\cos\theta_z$ of vessel mesh function f(x, y, z). Fig.7 shows a 3D µODT image of a mouse somatosensory motor cortex (1.9×1.5×1mm³) acquired at 10kHz A-scan rate, which included artifacts because of no angle correction. A vein (highlighted by dashed blue lines) and an artery (highlighted by dashed red lines)

showing flow discontinuity due to angle-velocity coupling were corrected by our gradient tracking method. After correction, CBFv of the vein increased by ~31-fold from v_{VF}=0.35±0.25mm/s to v_{VF}=11.07±3.12mm/s, whose measurement precision evaluated by its standard deviation (CV=0.28) was 4.4-fold smaller than its counterpart (CV=1.24) using 3-point correction method (v_{VF}=6.90±8.54mm/s). CBFv of the artery also increased dramatically (66.3-fold) from un-corrected velocity v_{AF}=0.36±0.13mm/s to v_{AF}=23.92±2.88mm/s, whose CV=0.12 was 10.8-fold smaller than CV=1.30 by 3-point method (v_{AF}=6.14±7.96mm/s). Both corrected AF and VF flow rates are close to the physiological parameters for the mouse cerebral cortex [8, 86].
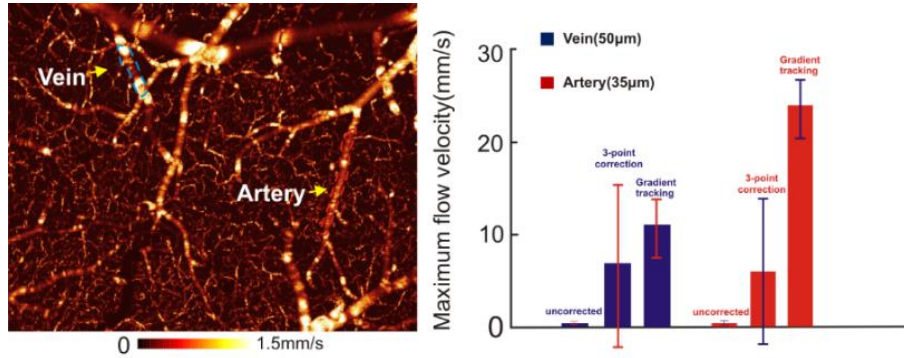
Figure 4-5 3D ODT image of quantitative CBFv network on a mouse somatosensory motor cortex (1.9×1.5×1mm^3). Left panel: 3D CBFv image without angle correction; Right panel: comparison of flow rate correction for a vein and an artery

2.3. Angle correction by Hessian matrix

To validate this method, we first applied it to a simulated helix H(cφ, rsinφ, rcosφ; 0≤φ≤5π) whose longitudinal angle is defined as:

$$\cos\theta_{z,Theoretical} = \frac{|r\sin\varphi|}{\sqrt{r^2 + c^2}}$$

Eq. 4-14

where r and c denote the radius and the helical pitch, respectively. Figure 4-6 shows the simulated helix (a) and the 3D color coded longitudinal angle θ_z(x, y, z: 0°-90°) derived from the 3D Hessian matrix method. The three planar images in Figure 4-6(b) are the corresponding MIP images of the 3D angle map projected onto the x-z, y-z, and x-y planes. Quantitative comparison between the theoretical and the modeled θ_z presented in Figure 4-6(c) demonstrates the efficacy of our method to restore the angle with an overall accuracy for x from 0 to 5πc to less than 1.18º±0.60º error for SNR=37.4dB and 5.73º±3.99º for SNR=4.4dB.
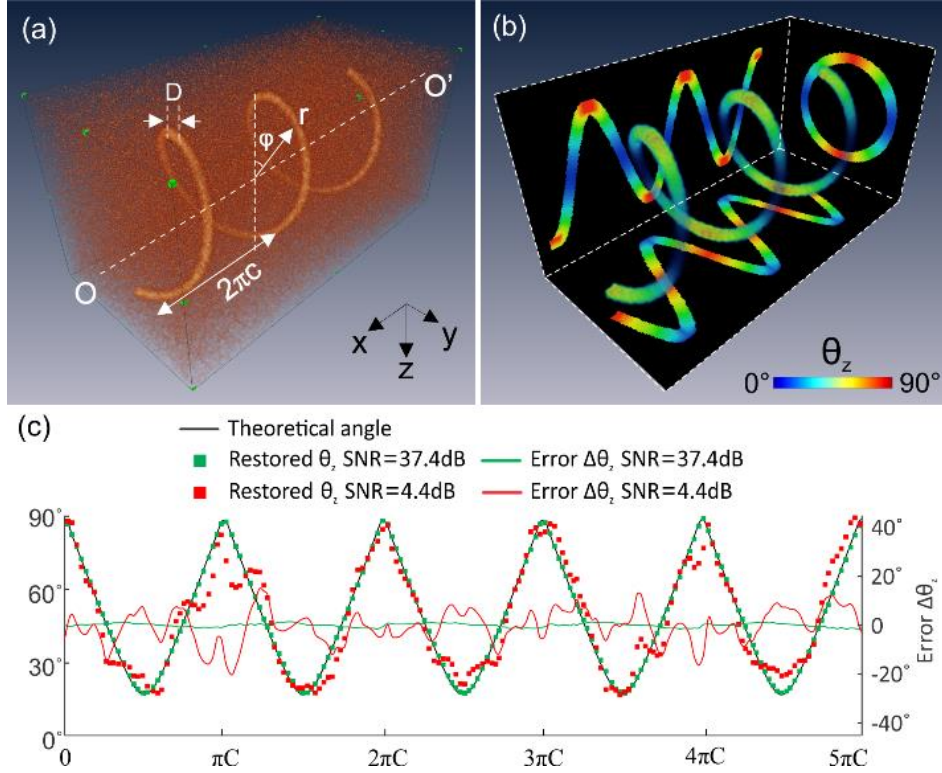
Figure 4-6 3D θ_z detection for a simulated helix. a) Simulated helix curve H(cφ, rsinφ, rcosφ: r=50pixels, c=15pixels, D=9pixels, $0\leq\phi\leq5\pi$, $\Delta\phi$=0.01rad/step) with salt & pepper noise (i.e., SNR$\approx$37.4dB), b) 3D longitudinal angle calculated by Hessian method, c) Quantitative θ_z comparison between theoretical (black line) and restored angles (green, red dots for SNR=37.4, 4.4 dB, respectively) and their errors (green, red lines for SNR=37.4, 4.4 dB, respectively). Image size (cropped): 150×150×300 pixels.

In addition, a flow phantom experiment was performed to assess the utility of this method to retrieve the θ_z matrix for absolute flow correction. In this experiment, 1% intralipid emulsion (Intralipid® 20%) in a ϕ280µm translucent micro-tube was driven by a precision syringe pump (CMA400, Microdialysis) at a constant pump rate of v_p=8.12mm/s. The microtube was wound onto a cylinder (e.g., ϕ10mm) to provide continuously varying θ_z from 70° to 90° to allow for Doppler angle tracking and flow correction.

Figure 4-7 compares the phantom flow images before and after Doppler angle correction. As expected, the apparent flow v_z acquired by 3D µODT exhibited obvious artifacts (a), i.e., v_z decreased with θ_z and diminished when θ_z→90°. Angle correction by Hessian matrix (c) or continuous gradient (b) tracking method (averaging number M=5) was effective for θ_z=71°-81°, which raised the severely underestimated flow rates to v_{Hess}=7.2-7.93mm/s and to $v_{Grad,M=5}$=5.23-9.30mm/s (M=5), both of which are close to v_p=8.12mm/s. As a result, the corrected flow velocity profile appeared more uniform (b, c) with varying θ_z. Quantitative analysis (d) revealed that both methods able to accurately trace the skeleton gradients or the θ_z matrix (e.g., with error less than 10% for θ_z=71°-81°); however, correction of v_z, to v by $v=v_z/cos\theta_z$ was less accurate for θ_z>82.6°. For instance, deviation of v_p by gradient tracking (v_{Grad}, M=5) drastically increased from -7.7% at θ_z=82.6° to >-47.6% when θ_z>85.0°. By comparison, deviation by Hessian (v_{Hess}) was <2% at θ_z=83.5°, then increased to 7.1% at θ_z=86°.

Despite that both gradient tracking and Hessian matrix methods can effectively correct angle-induced errors of Doppler flow in a single vessel, it is noteworthy that gradient tracking of multiple flows is cumbersome and impractical for the capillary CBF networks. Meanwhile, the Hessian method is voxel-based and therefore potentially suitable for tracking the complex microvascular networks. To further validate the present method, we applied the method to the flow images of C57BL/6 mice *in vivo*. In the experiment, mice were anesthetized by inhalation of 2% isoflurane and mounted onto a custom stereotaxic frame. A cranial window was surgically created on the mouse sensorimotor cortex with the dura remained intact, and the exposed cortex was filled with 1% agarose and sealed by a glass coverslip to minimize motion artifacts. To enhance capillary sensitivity, 6ml/kg intralipid was injected into the animal's circulation system through tail vein before µODT imaging.[13] 3D µODT was acquired at 10kHz A-scan rate to reconstruct the CBFv images over $2.4 \times 2 \times 1.4 mm^3$ (6k A-lines by 400 B-scans) on the mouse cortical brain.
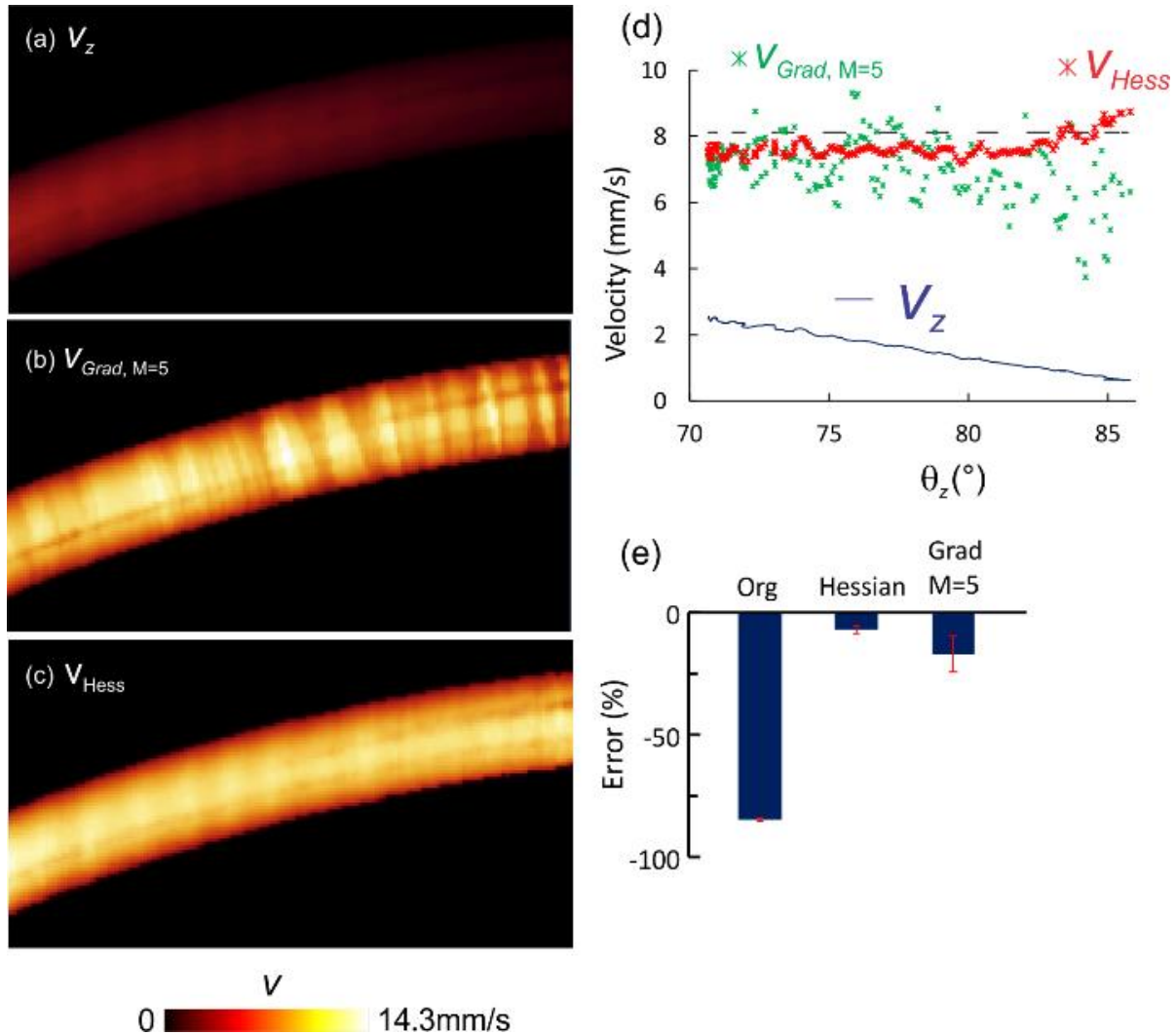
Figure 4-7 3D θ_z correction for phantom flow with 1% intralipid in a $\phi 280 \mu m$ micro tubing at a pump rate of 30µl/min or v_p=8.12mm/s. a) Side view of original flow image acquired by 3D µODT at 25kHz A-line rate, b) Flow image after θ_z correction with Gradient tracking method c) Flow image after θ_z correction with Hessian method. d) Comparison of flow rates with θ_z among original flow velocity v_z (blue), after Hessian

correction v_{Hess} (red) and gradient tracking v_{Grad} (green) (M=5), and pump rate v_p (dashed black). d) Errors before and after Hessian or gradient tracking correction ($80° \leq \theta_z \leq 81°$).

Figure 4-8 compares the 3D CBFv images before and after Doppler angle correction. Because of overwhelming vascular turnouts, pie-cut cross-sections are presented to illustrate the effects on flow quantitation. Without angle correction, the apparent CBFv image (a) showed severely underestimated flow rates, especially for most pial arterial and venous flows that were perpendicular to the direction of incident light beam ($\theta_z \to 90°$, $\cos\theta_z \to 0$). 3D Doppler angle image (b) computed from the Hessian matrix ($\sigma=1,2,3,4,5$) tracked the θ_z distributions of these flow compartments and thus allowed for angle correction to retrieve the absolute 3D CBFv image (c) based on matrix computation $v_{RBC}=v_z/\cos\theta_z$. After angle correction, pial venous flows were dramatically increased from under 1.08 ± 0.21mm/s (a) to over 5mm/s as highlighted by white arrows (c). Moreover, horizontally oriented capillary flows in deep cortical layers which were usually weak (a) can be readily restored by Doppler angle correction as highlighted by the yellow arrows (e.g., at ~1.2mm below cortical surface)
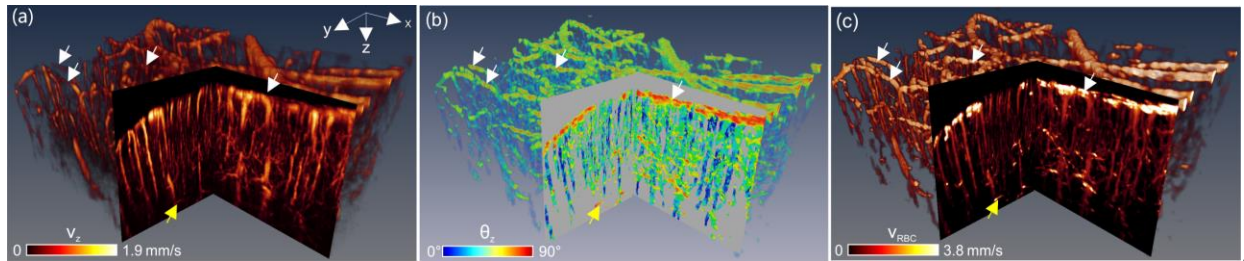
Figure 4-8 3D CBFv network image of mouse sensorimotor cortex (2.4×2.0×1.4mm3) before and after θz correction. a) Raw 3D μODT image (i.e., vz) without θz correction, b) 3D Doppler angle θz image c) 3D absolute vRBC image after θz correction by 3D Hessian matrix. Yellow arrow: horizontally oriented capillary flow in deep cortex usually undetectable without angle correction; White arrows; correction of pial flows. 2D pie-cut images are MIP images of 200μm-thick sub-volume.

3. Conclusions & Discussions

Neuroimaging techniques that enable high spatiotemporal resolution and quantitative imaging of the cerebral blood flow network and dynamics are of high clinical relevance and may provide important insight into brain physiology (hemodynamics, metabolism), brain function and to understand the mechanisms underlying neurovascular dysfunction of disease progression. Unlike conventional brain imaging techniques such as PET or MRI that allow for noninvasive whole brain diagnosis, intravital optical imaging may be restricted for deep brain imaging due to limited penetration depth, but it has many unique merits such as high sensitivity, superior spatiotemporal resolutions that compliment fMRI and PET modalities. For example, the high spatiotemporal resolutions can be used to help delineate the different vessel compartments that contribute to fMRI BOLD signals, and assess whether the BOLD changes are due to flow rate (CBFv) and/or changes in vessel diameters (dilation or contraction). In recent years, intravital TPM has been widely used to visualize the cerebral microcirculatory distribution and to assess cellular vascular interactions. By tracking fluorescently labeled RBC movement, TPM is capable of accurately measuring the RBC velocity within individual micro-vessels. Alternatively, optical coherence Doppler tomography is a relatively new high-resolution imaging technique that can provide tracker- or

label- free quantitative imaging of CBFv (i.e., RBC velocity) based on Doppler frequency shift generated by moving scattering particles (presumably RBCs in the bloodstream). Recent studies of our labs and from others show that quantitative ODT can be uniquely useful for imaging the highly heterogeneous CBFv network responses to brain activations, such as cocaine elicited vasoconstriction and microischemic events. Despite recent technologic advances and some preclinical imaging studies, several remaining technical problems may hinder its applications in brain functional imaging studies, among which limited dynamic range for Doppler phase detection and Doppler angle correction may prevent it for simultaneous imaging of vastly different flow rates in the cerebrovascular network (e.g., fast flows over 30mm/s in large AF and VF vs. slow flows under 0.05mm/s in minute capillaries) and accurately measuring absolute flow values. Methods such as dual-beam ODT and frequency binning algorithms have been reported to tackle the problems. Here, we apply two relatively simple but effective methods, i.e., phase summation algorithm and gradient vessel tracking method to address the problems and validate the effectiveness of these methods in both flow phantom studies and in vivo 3D mouse CBFv imaging studies. Phase summation method enhanced the detection of the minimal detectable flow while preserving the dynamic range, i.e., the upper threshold for fast flow (causing phase wrapping).

Gradient vessel tracking technique continuously traced the Doppler angle $\cos\theta_z(x,y,z)$ of a vessel by tracking the gradients of the extracted vessel skeleton $f(x,y,z)$. In the phantom study, we showed that it improved the accuracy for true flow velocity measurement by 11.5-fold over uncorrected flow value and 6.1-fold over conventional 3-point correction method. Although not shown here, the over-correction around $\theta_z \approx 90°$ can be further suppressed by removal of background noise. For in-vivo validation studies, we showed the neurotoxic effects of acute and chronic cocaine on the CBFv network on the mouse somatosensory motor cortex, clearly documenting drastic vasoconstriction and microischemia elicited by chronic cocaine administration or by repeated acute cocaine challenges. For instance, the results showed $22.49\pm8.71\%$ (p<0.05; n=3 vessels) decrease in arterial CBFv, $68.47\pm6.00\%$ decrease (p<0.05, n=3 vessels) in veinal CBFv, and an overall $49.06\%\pm17.88\%$ (p<0.05, n=20 capillaries) decrease in capillary CBFv networks.

Unlike the previously reported skeleton gradient methods[37, 38], the Hessian matrix method is voxel-based and retrieves θ_z matrix by utilizing eigenvalue analysis of 3D Hessian matrix. For proof of concept, we presented simulation result that clearly demonstrated the efficacy of this method to trace θ_z of a Gaussian profiled helix with an overall error less than $1.18°\pm0.60°$. Then we evaluated the algorithm on flow phantom (1% intralipid) with θ_z ramping from 70° to 85° and showed that it was able to accurately restore the absolute flow rate with error less than 7.1% even at a very flat angle of θ_z=86°, while gradient tracking method showed escalating deviation (>47%). Lastly, we performed in vivo validation study on mouse sensorimotor cortex and showed that unlike previous methods such as gradient tracking that only corrected individual vessels, 3D Hessian matrix approach is voxel-based and was thus able to correct the entire microcirculatory CBFv networks, which included the correction of severely underestimated pial flows (mostly horizontally oriented) and uncovering those horizontally oriented capillary flows in the deep cortical layers (e.g., >1.2mm of depths). Additionally, the present method is reasonably robust for low and intermediate noise (e.g. SNR≈4) and therefore allows for detecting axial angle of complex capillary networks which usually suffer low SNR. Such a capability for quantitative imaging of the absolute CBFv networks is important to understand the cortical hemodynamics and the related disease progressions (e.g., ischemia). The limitation of this method occurs in the extreme cases when Gaussian kernel scale and targeted vessels are mismatched[87].

5. Detecting early tumor boundary using ultrahigh-resolution optical coherence tomography

According to the average annual age-adjusted incidence rates for cancers (2009-2013), brain and central neuron system tumor are the commonest and the 3rd commonest cancer among children (Age 0-14 Years) and adults (Age 15-39 Years) in U.S.[88]. Additionally, brain tumor is one of the most dangerous cancers with high mortality rate and short median length of survival (40.9weeks)[89]. To improve the survival rates of brain cancer, early diagnosis and treatment is strongly encouraged. Therefore, evaluating tumor size and detecting the tumor boundary is of great clinical implication [90] which not only provides early diagnosis but also enables access to therapy outcomes[91] However, there remains a huge challenge for both macroscopic and microscopic imaging modalities. The conventional macroscopic technologies, for instance, positron-emission tomography, single-photon emission computerized tomography and diffusion MRI, have demonstrated their capability for assessing the response to cancer therapies [91-93]. However, their spatial resolution, typically greater than 5mm, fail to image capillary and cannot provide detailed change of the tumor microenvironment. On the contrary, multiphoton laser scanning microscopy can provide a stunning insight into tumor pathophysiology including gene expression, angiogenesis and metabolic microenvironment however its limited field of view prevents it from being the ideal tool for detecting the tumor boundary in a relatively large scale[71].

Recent advances in optical coherence domain technologies permit quantitatively imaging cerebral blood flow velocity (CBFv) with both large field of view (FOV) and the capillary spatial resolution and thus are playing increasingly important role in cancer research. OCT intensity image characterizes the depth dependent scattering properties of biological tissue and 3D morphological information which can be used as criteria for identifying soft tissue sarcomas[94, 95]. Additionally, Valery P.Z. et.al. integrated Raman spectroscopy into OCT system to further improve the diagnosis of cancer cells[96]. Benjamin J V. et.al. demonstrated the scattering difference between the highly scattering necrotic core and low scattering healthy tissue [97]. However, using its highly scattering property to segment tumor boundary is debatable and requires more diagnostic evidence. Although being widely discussed, the scattering based method for identifying tumor region is heavily dependent on the focus position and field curvature of objective. Alternatively, hemoglobin saturation and oxygenation map are also promising biomarker for tumor detection and characterizing tumor progression [48, 98].

Here we propose an alternative approach that identifies tumor boundary by analyzing the instinct features of microvascular networks in the tumor microenvironment. Noteworthily, angiogenesis, triggered by hypoxic environment, is a process of recruiting new micro-vessels to supply rapid growth of tumor[99, 100]. It is one of common features of the tumor microenvironment and, most importantly, is a detectable feature by OCT. Thus, we utilized the difference of vascular density between highly angiogenic tumor and health tissue as the image contrast for identifying early tumor boundary since the recruit of micro-vessels occurs at the early phase of tumor progression before the formation of necrotic core and the commence of avascular process [101]. Furthermore, we compared the sensitivity/specificity of the present method with those of other imaging technologies including μODT image, μOCT intensity image, white light image taking GFP fluorescence image as the standard-of-care. Moreover, to reveal the progression of the tumor microenvironment during tumor growth, a longitudinal study was conducted monitoring multiple

parameters including capillary flow velocity, microvascular density and fluorescence area from which the correlations of those parameters was derived.

With extended penetration depth [102] and improved capillary sensitivity [103], μOCT provides a stunning insight into the tumor microenvironment and tumor progression. In this chapter, we demonstrate a new method for detecting tumor boundary by analyzing the vascular morphological features of the tumor microenvironment. Additionally, the unique capability of longitudinally imaging tumor angiogenesis provides a new approach to assessing tumor therapy outcomes which is of great clinical implication for developing novel anti-angiogenic therapies.

1. Methods
   1.1. Animal preparation

The mouse (C57/B6, male, 12-14 weeks, Jackson lab, n=3) was anesthetized with the mixture of 2.0-2.5% isoflurane and 100% oxygen and its head was firmly fixed on a custom stereotaxic frame to minimize motion artifacts. A rectangular skull (~2.5mm × ~2.5mm) above sensorimotor cortex was carefully thinned and removed leaving an exposed area of cortical surface which was then immediately covered by 2% agarose gel and affixed with a 100μm-thick glass coverslip using biocompatible cyanocrylic glue. For the chronic case, the surgical procedure is similar to the aforementioned protocols [104] except dental cement was spread around the edges of the glass coverslip to secure its attachment with its skull for long term optical access. The whole wound was sutured and sterilized and the mouse was given antibiotic and anti-inflammation treatments if necessary. The physiological states of the mouse including electrocardiography (ECG), respiration rate and body temperature were continuously monitored during the experiment (SA Instruments, NY). The animal protocols were approved by Institutional Animal Care and Use Committees of Stony Brook University and followed the National Institutes of Health (NIH) Guideline for Care and Use of Laboratory Animals.

   1.2. Intracranial tumor transplantation

For the longitudinal tumor study, a total of 1.5×10^4 GL261-GFP tumor cells in 100 μl of DMEM was slowly injected into the mouse's cortex (~300μm below cortical surface) using a 30-gauge hypodermic needle whose injection rate was controlled by a precision Infusion pump (PHD-2000, Harvard Apparatus).

   1.3. μOCT system and image reconstruction

A 1310nm ultrahigh-resolution optical coherence tomography (μOCT) system was used for imaging cerebral microvascular networks and the 3D structure of cortical surface in vivo[102]. Specifically, the new μOCT system used a superluminescent diode broadband laser (λ=1310nm; ΔλFWHM≈200nm) to illuminate a 2×2 wavelength-flattened fiberoptics Michelson interferometer providing an axial resolution of 2.5μm in biological tissue (Lc=2(ln2)1/2/π·λ2/Δλcp). The sample arm light was focused on the subcortical layers of mouse sensorimotor cortex by an achromatic doublet (NIR f18mm/NA0.25, Edmound Optics) yielding a maximum lateral resolution of 3.2μm.

Vasculature image (μOCA) and blood flow image (μODT) were post-reconstructed by speckle variance based angiography [105] and phase subtraction method[16], respectively. During data acquisition, the en-face maximum intensity projection of cerebral vascular networks was instantaneously reconstructed and monitored by a graphic processing unit (GPU) boosted custom GUI programming allowing for B-scan processing (cross-sectional scan, 2M pixels) as fast as 473fps.

1.4. GFP fluorescence imaging

A custom lighting module was developed based on a modifed fluoresence zoom microsope (AZ100, Nikon) which comprises of 488nm LED light for GFP excitation. The 488nm LED light illuminated the cortical window (ϕ3 mm) via fiber bundle (NA/0.25). The backreflected light was collected by a 2× Plan Apo objective (NA=0.22, WD=45 mm, FOV=ϕ5 mm) and projected onto a cooled 12-bit CCD camera (14bits sCMOS camera, Zyla 4.2, Pixel size: 6.5um, Andor) after passing through an GFP emission (CWL=530nm, BW=39nm).

1.5. Removal of motion artifacts for SV-OCA

Suppression of bulk motion artifacts is critical for ensuring the precise vasculature detection by Frangi-Hessian filter because it tends to enhance the stripe-like motion artifacts. For speckle variance based optical coherence angiography (SV-OCA), the motion artifacts are the results of the substantial image decorrelation across multiple B-scans (N) due to the sudden displacement in x,y,z direction or even the tilted angle[106] (Figure 5-1a). Here we applied redundant scans (N'>N) and calculated SV-OCA only based on the most correlated B-scans to minimize the artifacts induced by the outliers. Figure 5-1 demonstrates the improved image quality by comparing the original SV-OCA image (Figure 5-1a) with the motion-removed SV-OCA image (Figure 5-1b). Figure 5-1 c) and d) are the corresponding cross-sectional images before and after motion removal. To identify the most correlated B-scans among the multiple repeated B-scans e.g. N=6, we calculated the averaged correlation coefficient r(i) using Eq. 5-1 and Eq. 5-2. Those B-scans with the 6 largest correlation coefficients were picked for calculating SV-OCA which are highlighted by black arrows in Figure 5-1e)

$$r(i,j) = \frac{\sum_x \sum_y \left(I_i(x,y) - \overline{I_i} \right)\left(I_j(x,y) - \overline{I_j} \right)}{\sqrt{\left(\sum_x \sum_y \left(I_i(x,y) - \overline{I_i} \right)^2 \right)\left(\sum_x \sum_y \left(I_j(x,y) - \overline{I_j} \right)^2 \right)}}, i,j \leq N', i \neq j \qquad \text{Eq. 5-1}$$

$$\bar{r}(i) = \frac{\sum_{j=1}^{N'} r(i,j)}{N'}$$

Eq. 5-2

Where r(i,j) represents the correlation coefficient across different images. i and j are the frame index. x and y denote the pixel index of each individual B-scan. After bulk motion removal, the signal to noise ratio (SNR) was drastically improved from 2.11dB to 19.03dB for the cross-sectional image shown in Figure 5-1d).
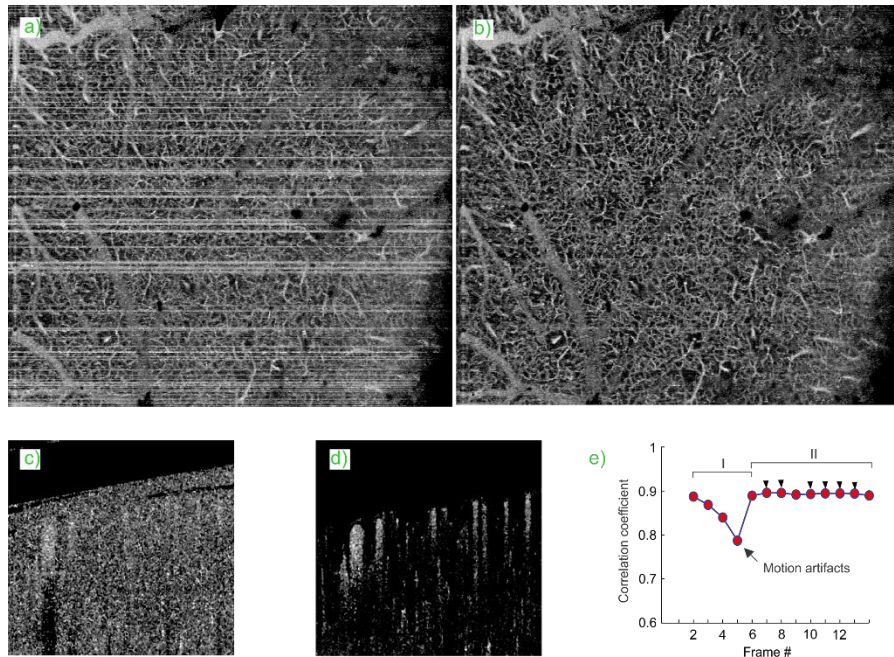
Figure 5-1 Motion artifacts removal. a) and b) are SV-OCA images before and after motion removal c) and d) are cross-sectional SV-OCA image before and after motion removal. e) Plot of averaged correlation coefficient. I: Declined correlation due to motion artifacts; II: High correlation for stable frames. Black arrows highlight the 6 largest correlation coefficients.

1.6. Hybrid Hessian filter

Micro-motion of animal's brain tissue induces background noise which deteriorates system's signal to noise ratio (SNR) for both μODT and μOCA images. When the weak signal is competing with its surrounding noise floor, the conventional grey-level thresholding segmentation technique is clumsy to extract the true vascular information. On the contrary, morphological features based algorithms, e.g. multi-scale Frangi-Hessian filter, [107] provide robust access to abstracting vessel-like features by analyzing eigenvector and eigenvalue of its Hessian matrix. Its mathematical theory starts with local Taylor expansion meaning that the imaging intensity I(x) at a point x_0 is also dependent on the derivatives of neighborhood pixels (Eq. 5-3).

$$I(\vec{x}_0 + \delta\vec{x}_0, \sigma) \approx I(\vec{x}_0, \sigma) + \delta\vec{x}_0^T \nabla_{0,\sigma} + \delta\vec{x}_0^T H_{0,\sigma}\delta\vec{x}_0 \qquad \text{Eq. 5-3}$$

$$\delta x_0^T H_{0,\sigma}\delta x_0 = \left(\frac{\partial}{\partial\delta x_0}\right)\left(\frac{\partial}{\partial\delta x_0}\right)I(x_0, \sigma) \qquad \text{Eq. 5-4}$$

Where $\nabla_{0,\sigma}$ and $H_{0,\sigma}$ represents the gradient vector (1st order derivative) and Hessian matrix (2nd order derivative) at scale σ, respectively. Frangi-Hessian algorithm analyzes eigenvalues and eigenvectors of Hessian matrix (Eq. 5-4) from which the principal direction of local structure can be decomposed.

Additionally, the 2nd derivative of discrete matrix can be obtained by convolving the original image with the 2nd derivative of a Gaussian filter. Thus

$$\delta x_0^T H_{0,\sigma}\delta x_0 = \left(\frac{\partial}{\partial\delta x_0}\right)\left(\frac{\partial}{\partial\delta x_0}\right)I(x_0, \sigma) = \sigma^{2\gamma}I(x_0, \sigma)\frac{\partial^2}{\partial x^2}G(x, \sigma) \qquad \text{Eq. 5-5}$$

Where $G(x,\sigma)$ and γ denote the D-dimensional Gaussian kernel and derivative normalization parameter.

$$G(x, \sigma) = \frac{1}{\left(2\pi\sigma^2\right)^{D/2}}e^{-\frac{\|x\|}{2\sigma^2}} \qquad \text{Eq. 5-6}$$

By applying the eigenvalue equation

$$u_{\sigma,i}^T H_{0,\sigma}u_{\sigma,i} = \lambda_{\sigma,i} \qquad \text{Eq. 5-7}$$

We can obtain eigenvalue decomposition λ_1, λ_2, λ_3 corresponding to their eigenvectors $u_{\sigma,1}$, $u_{\sigma,2}$, $u_{\sigma,3}$ in 3 orthonormal directions. Taking the assumption $|\lambda_1| \leq |\lambda_2| \leq |\lambda_3|$, 3 eigenvalues and their relations characterize the 3D local morphological feature. In particular, λ_1 is the eigenvalue in vessel direction and thus close to zero, and λ_2, λ_3 are eigenvalues in the radial direction. In 3D image, eigenvalues of a tubular structure are supposed to satisfy: $|\lambda_1| \approx 0$, $|\lambda_1| << |\lambda_2|$, $\lambda_2 \approx \lambda_3$.

To calculate the vessel likeness of image, two geometric ratios are defined:

$$R_A = \frac{|\lambda_2|}{|\lambda_3|} \text{ and } R_B = \frac{|\lambda_1|}{|\lambda_2||\lambda_3|} \qquad \text{Eq. 5-8}$$

Where R_B is applied to differentiate bold-like structure because in this scenario it attains its maximum otherwise $R_A \approx 0$ since $|\lambda_1| \approx 0$ for vessel-like structure. R_A is defined to distinguish the plate-like structure from line-like structure since it accounts for the aspect ratio of two 2nd order

derivatives perpendicular to vessel orientation. To eliminate the background noise, another matrix norm is defined to measure "second order structurenesss" whose amplitude is low for background noise pixels.

$$S = \|H\|_F = \begin{cases} \sqrt{\lambda_1^2 + \lambda_2^2} \ \textit{for 2D image} \\ \sqrt{\lambda_1^2 + \lambda_2^2 + \lambda_2^2} \ \textit{for 3D image} \end{cases}$$
Eq. 5-9

Vessel-likeness function of 3D image is defined as

$$v_0(\text{s}) = \begin{cases} 0 & \textit{if } \lambda_2 > 0 \textit{ or } \lambda_3 > 0 \\ \left(1 - \exp\left(-\dfrac{R_A^2}{2\alpha^2}\right)\right)\exp\left(-\dfrac{R_B^2}{2\beta^2}\right)\left(1 - \exp\left(-\dfrac{S^2}{2c^2}\right)\right) \end{cases}$$
Eq. 5-10

Where $v_0(\text{s})$ characterizes the vessel-likeness of 3D vascular network which attains its maximum when the targeted vessel size is comparable to the kernel scale σ. α, β, c are three thresholding parameters that control the filter's sensitivity for tubular shape.

1.7. Vascular network segmentation

Calculating vessel-likeness map with huge variance of vessel size remains a great challenge for the Frangi-Hessian method. Although multi-scale Hessian matrix were used in calculation, simultaneously detecting small capillary ($\phi < 8\mu m$) and large veins ($\phi > 100\mu m$) induces either meshed artifacts in large vessels or blurring artifacts for small capillary. Figure 5-2 shows two artifacts due to the mismatch between the Frangi-Hessian scale factor and vessel size. For example, in Figure 5-2(a), Hessian filter with small scale factor σ ($1 \leq \sigma \leq 3$) can only enhance small vessels ($\phi < 8\mu m$) remaining undetected large branches. On the contrary, if a large range of scale factor was used ($1 \leq \sigma \leq 15$), blurring effect can be induced leading to fatness of small capillary (Figure 5-2b').

To address this problem, Siavash et. al. used a hybrid method that combines the Frangi-Hessian filter with the thresholding segmentation to segment large and small vessel separately[87]. Here, with considering the heterogeneity of small vessel intensity, we used the region grow algorithm to detect large branches and used the Frangi-Hessian filter for segmenting capillary network. Briefly, the region grow algorithm is to expend or grow 'seeds' region by comparing the image intensity of the test pixel $I(x)_T$ with that of the already-known 'seed' pixel $I(x)_S$. Then the test pixel is marked as new 'seed' pixel if the intensity difference is smaller than a pre-defined threshold t. Until no more test pixels can be included in 'seeds' domain, the iteration for "seeds" growing stops. As shown in Figure 5-3, the original OCA image was separated into two portions: large vessel network and small vessel network. The former was segmented by region grow algorithm and the latter was enhanced by Hessian filter and then was further binarized into black and white image Figure 5-3(d). Then, the binary images of large vessel network and microvascular network were remerged together to form the binary image of whole vascular network Figure 5-3e).
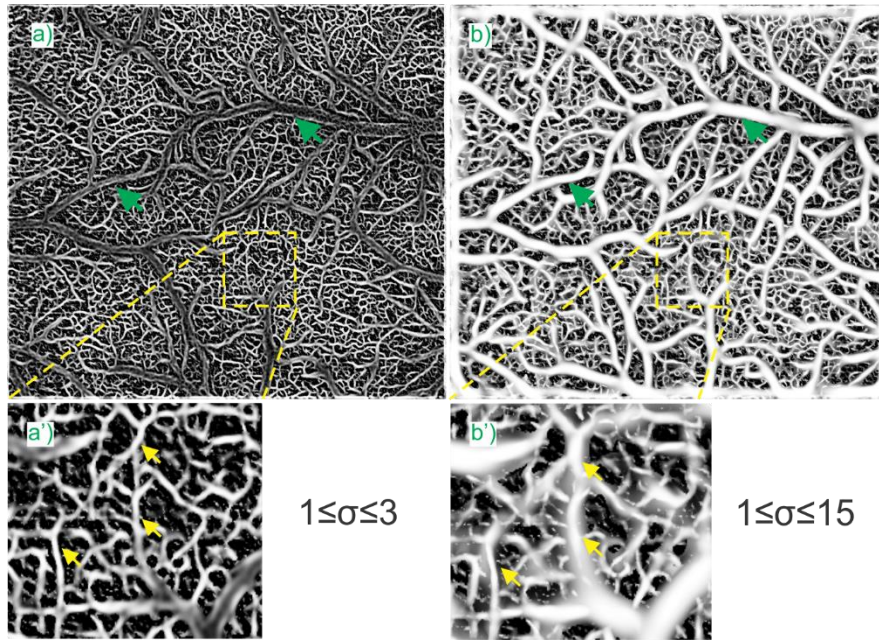
Figure 5-2 Artifacts induced by scale mismatch between Hessian matrix and the target vessel. a) and b) are Vessel-likeness map processed by multi-scale Frangi-Hessian filter of small scale factors ($1 \leq \sigma \leq 3$) and large scale factors ($1 \leq \sigma \leq 15$) a') and b') are the corresponding zoom-in images. Green arrows in a) point out the undetected large branches which are, on the contrary, clearly identified in b). Yellow arrows in a') point out several small capillaries which are fatter and blurring in b').
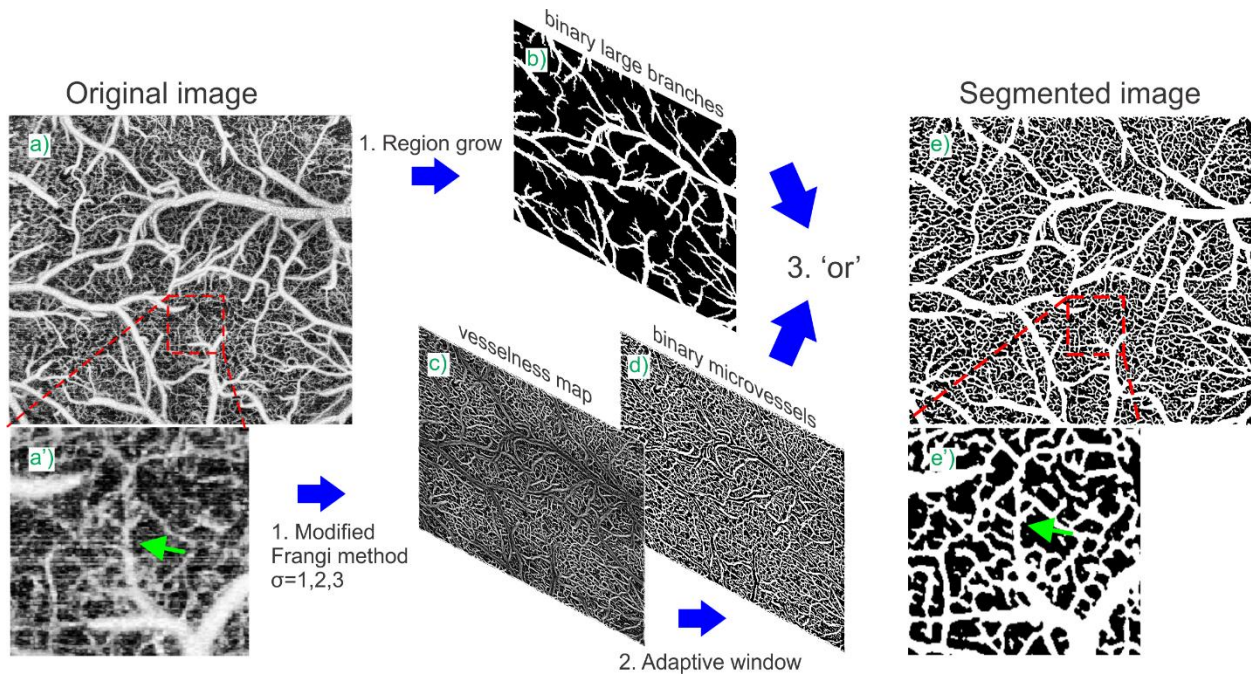
Figure 5-3 Schematic diagram of hybrid segmentation combining Frangi-Hessian method and region grow algorithm. a) and a') Original µOCA image of mouse sensorimotor cortex and zoon-in image. b) Binary image of large vessel network obtained by region grow algorithm c) Vessel-likeness map calculated with small scale factor σ. d) Binary image of microvasculature segmented by an adaptive window. After merging

60

two binary images b) and d), the final segmented image e), e') is obtained. Green arrows in a') and e') point out the segmentation details.

Figure 5-4 shows the processing flow for tumor boundary detection. The binary image of entire vascular network Figure 5-4b) was first calculated based on the original OCA image Figure 5-4a) using the aforementioned hybrid segmentation algorithm. Then we calculated its skeletonized image and converted it to spatial resolved density map Figure 5-4c) characterized by fill factor (FF) of a rolling window (50*50 pixel) using the following equation:

$$FF = \frac{Pixel \, \# \, of \, Capillary}{Pixel \, \# \, of \, Total \, Area}$$

Eq. 5-11

Then, the normalized density map was calculated by the follow equation for tumor boundary detection:

$$R(x, y) = \frac{D(x, y) - \overline{D}}{\overline{D}}$$

Eq. 5-12
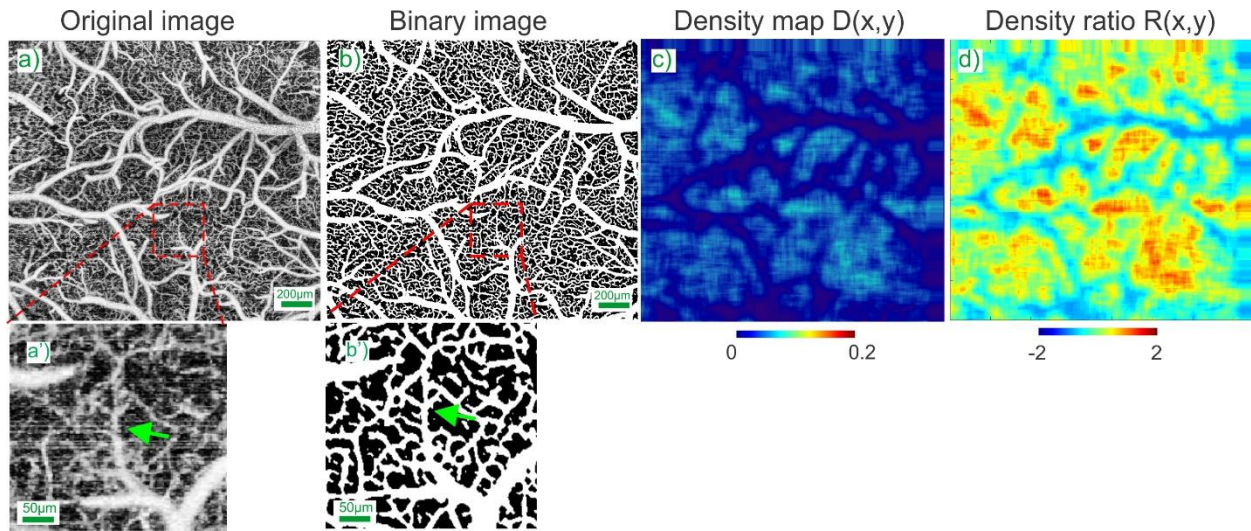
Figure 5-4 Flow chart of vascular segmentation method. a) and a'): Original μOCA image of mouse sensorimotor cortex and zoom-in ROI. b) and b') Binary image of vascular network and zoom-in ROI c) Density map of capillary network d) Density ratio map. Green arrows in a') and b') point out the uncovered microvascular details.

2. Results
   2.1. Detection of early tumor.

We identified the boundary of a transplanted tumor on mouse sensorimotor cortex based on the density ratio map of tumor microvascular network. Figure 5-5 compares the in-vivo and ex-vivo

images of control, saline injected and tumor injected mouse cortex. Figure 5-5a), e) and i) are their original μOCA images from which the distance maps Figure 5-5b), f), j) were derived to characterize the vessel size. Figure 5-5c), g), k) are the corresponding density ratio images. As shown in these images, both control and saline demonstrate uniform microvasculature distribution and smooth branch pattern except avascular area due to the injection injury (green dashed circle in Figure 5-5e). On the contrary, the vascular network of tumor demonstrates obvious angiogenic cluster and is surrounded by tortuous pial vessels. Additionally, the newly grown vessels inside of the tumor are larger than normal capillary showing blue-green in a distance map Figure 5-5j). Furthermore, we found the density ratio of the tumor center (black dashed circle) is $109.10 \pm 35.64\%$, profoundly higher than that of normal area far away from the center (red dashed circle) ($-10.92 \pm 27.76\%$). Furthermore, the density ratio of tumor area is also significantly greater than the mean level of control ($27.36 \pm 22.20\%$) and saline case ($29.14 \pm 13.48\%$).

Additionally, H&E staining image were used to cross-validate the tumor detection by μOCA in which d), h) and i) were imaged with low magnification (x4) while d_1), h_1) and i_1), i_2) were imaged with high magnification (x40). Owing to the large FOV in low magnification image (i), a solid tumor is readily seen which yields clear boundary against surrounding healthy tissue. Furthermore, a huge blood lake (black dashed circle) is readily identified beneath the tumor suggesting the recruit of massive blood flow during the early stage of tumor progression. It is noteworthy that more red blood cells were found in the tumor area (black arrows in i_1) compared to the control region (black arrow in i_2) which highly agrees with the active angiogenic region detected by μOCA. On the contrary, both the control and saline injected cortex are normal expect minor accumulation of RBCs due to the injection injury (h_1).
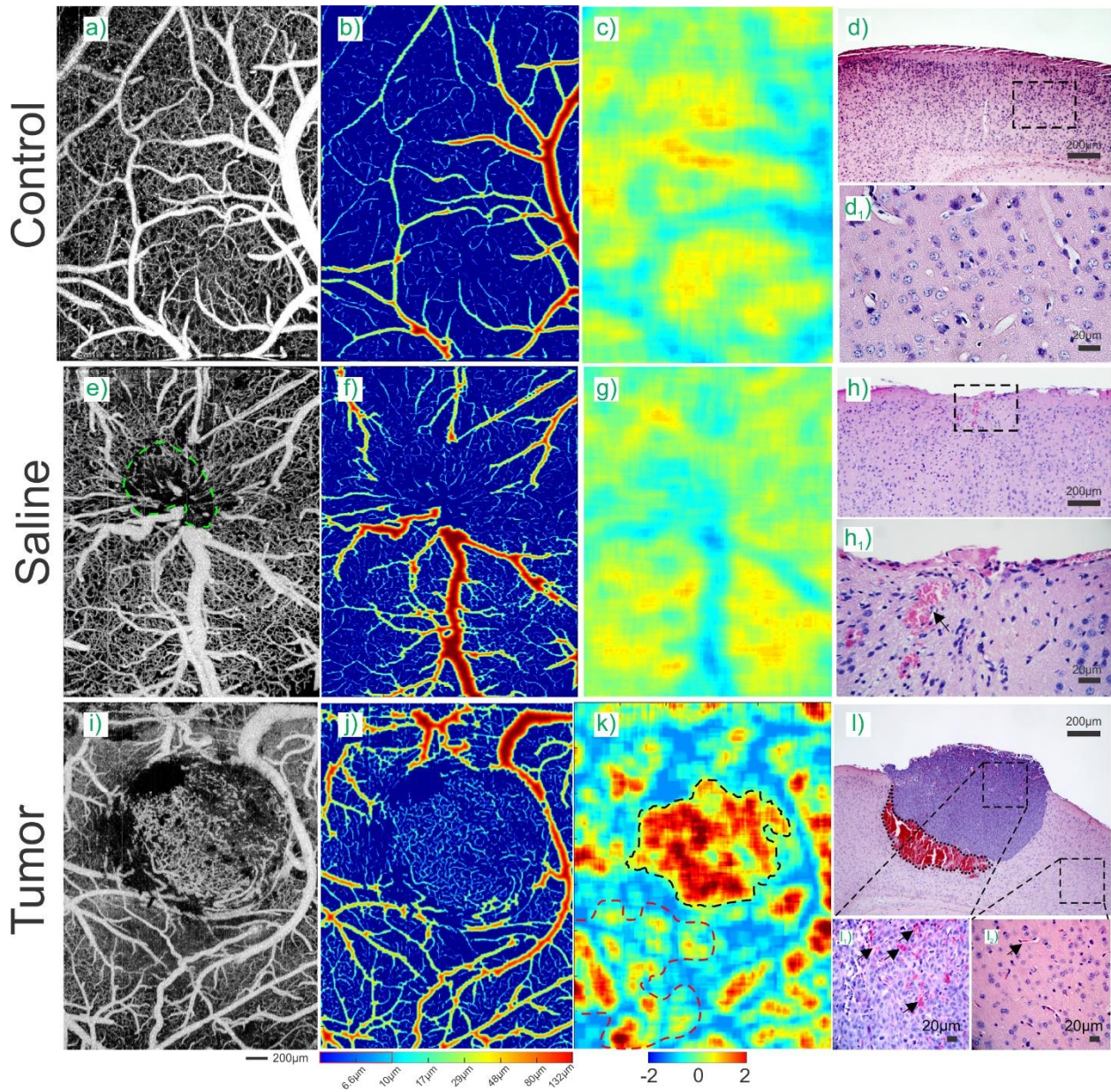
Figure 5-5 Comparison between control, saline sham and tumor injected mouse cortex. a) µOCA image of vascular network of mouse sensorimotor cortex. b): Euclidean Distance map shows the vessel size heterogeneity of vascular network c) Density ratio image d) H&E stain of brain tissue (magnification x4) d_1) Zoom-in H&E stain of brain tissue (magnification x40). e-h) and i-l) are the corresponding images acquired for a saline sham and a tumor mouse, respectively where i_1) and i_2) are zoom-in H&E stain image of tumor healthy tissue.

2.2. Tumor boundary comparison

Figure 5-6 compares the tumor boundary identified by different imaging technologies including en-face µOCT, µOCA, µODT, RGB image, white light image and GFP fluorescence image as standard of care. Here, detection sensitivity and specificity are defined as:

63

$$\text{Sensitivity=}\frac{\text{True Positive area}}{\text{GFP area}}$$

Eq. 5-13

$$\text{Specificity=}\frac{\text{True Negative area}}{\text{Total area-GFP area}}$$

Eq. 5-14

The change of tissue scattering properties during cancer progression has been used for early cancer detection[108]. For example, the highly scattered area (a_1 green arrows) implies the formation of necrotic core which, however, only occupies a fractional portion of the solid tumor and fails to provide the precise prediction of tumor boundary. Due to the intensity variance of en-face µOCT image, scattering based tumor detection only provides sensitivity and specificity as low as 34.48% and 55.90%, respectively. The limited detection sensitivity can be readily addressed by µOCA based ratio density map which demonstrates the highest specificity (98.18%) followed by µODT (97.87%). However, µODT fails to provide the comparable high sensitivity. On the contrary, RGB image provides superior sensitivity (97.83%) by showing the large radish area (Figure 5-6d). In Figure 5-6f, we merged all boundaries detected by these modalities for comparison in which RGB image gives the larges boundaries detection while µODT provides the most conservative prediction compared to the GPF boundaries. The boundary given by intensity image is random. Interestedly, density ratio image by µOCA provides the most correlated tumor area prediction that ensures the practicality of early cancer detection.
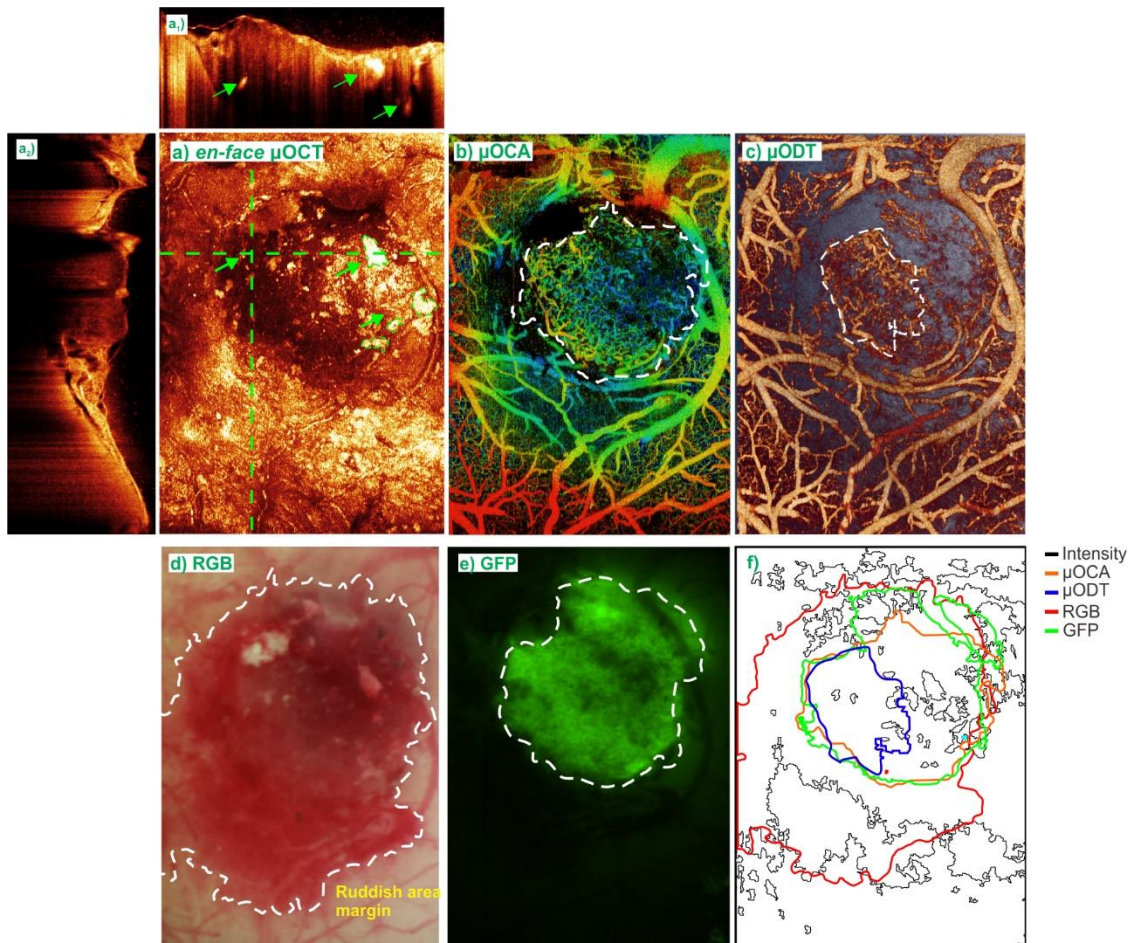
Figure 5-6 Comparison of tumor boundary detection by different technologies. a) OCT scattering image. a_1), a_2) are cross-sectional images whose locations in a) are highlighted by the dashed horizontal and vertical green line. Green arrows point out the highly scattering necrotic core b-e): Depth coded μOCA, μODT, RGB, GFP image with tumor boundary marked by white dashed line. f) Tumor boundaries detected by 5 different modalities.

2.3. Longitudinal tracking of GL261-GFP

To characterize the dynamic change of the tumor microenvironment, we used μODT and μOCA to track the change of microvascular network and used GFP fluorescence imaging to track the tumor cell proliferation. Figure 5-7 shows the dynamic monitoring of GL261 tumor progression acquired Day 7, 14, 18, 24 after tumor cell injection. On Day 7, the vasculature surrounding the injection spot had no difference from that of the saline sham shown in Figure 5-5e) in which neither angiogenesis nor fluorescence signal were present. Interestedly, during the 2nd week, the fluorescence area did not grow while both the capillary flow and capillary density kept increasing steadily. Specifically, capillary flow reached its maximum level 0.65 ± 0.19mm/s at Day 14, approximately one fold faster than its control counterpart 0.37 ± 0.07mm/s. At the meantime, capillary density achieved a plateau FF=0.31 ± 0.03 at Day 14 which was 43% higher than day 7. The tight coupling between capillary flow and angiogenesis suggested that tumor progression created a huge demand for blood flow supply and therefore recruited neovessels to support the rapid tumor growth. On the contrary, the growth of fluorescence area was delayed which did not start to boost until Day 14 when its size increased substantially to 0.49mm^2. During the 3rd and the 4th week, the tumor cell proliferated exponentially showing a fluorescence area of 4.15mm^2 on Day 18 and 17.16mm^2 on Day 24. Interestingly, both capillary density and flow rate in the tumor center started to decline after day 18 which were considered as the sign of apoptosis.
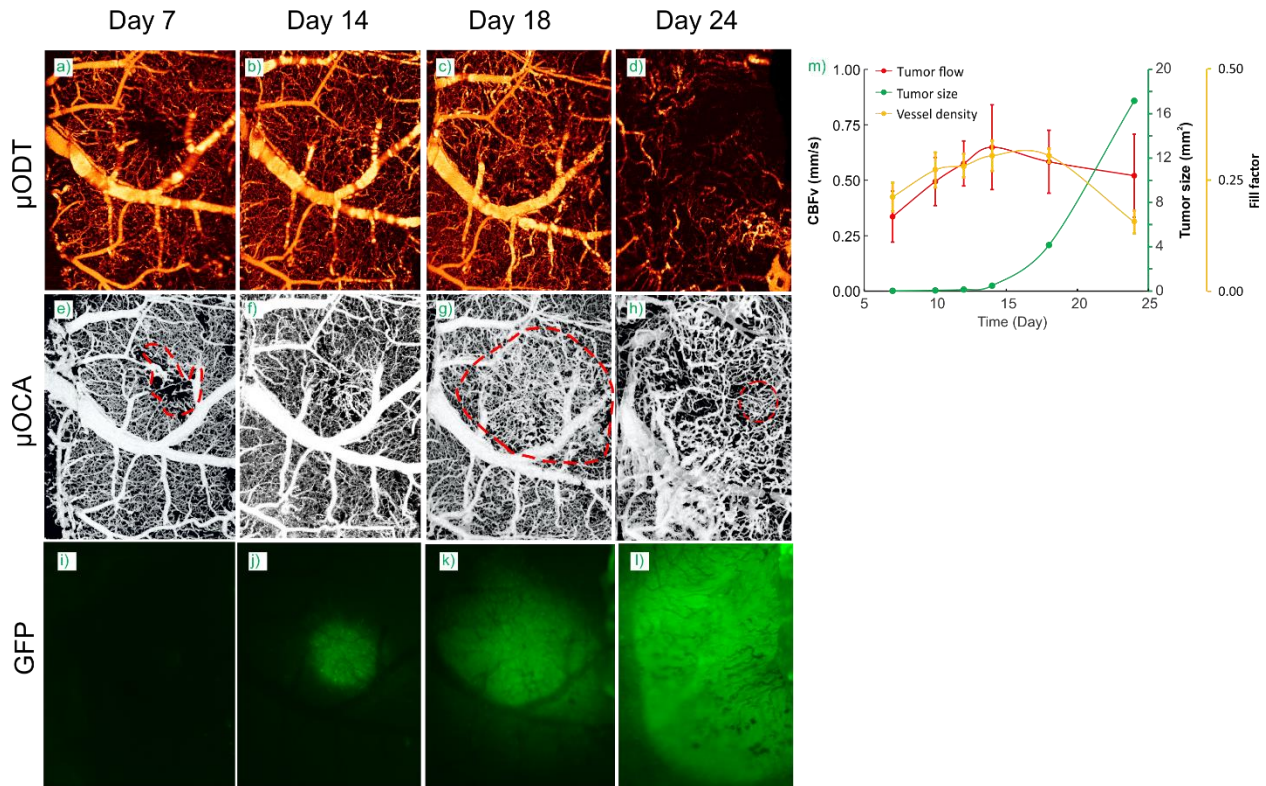
Figure 5-7 Longitudinal tracking of tumor progression with μODT/μOCA and fluoresence imaging. a-d) μODT images of Gl261 tumor acquired on Day 7, Day 14, Day 18, Day 24 after the injection of tumor cells. e-h) and i-l) are the corresponding μOCA and GFP fluoresence images acquired on the same day. m) Time course plots of capillary flow, capillary density (Fill Factor) and tumor size (GFP area).

3. Conclusion and Discussion

In this study, we detected the boundary of solid tumor by analyzing the morphological feature of microvascular network in the tumor environment. Additionally, we compared the tumor boundary detected by the present method with those by other imaging technologies. We found the density ratio map based on μOCA provides superior sensitivity and specificity (≥80%) for detecting tumor boundary over other technologies. A longitudinal study of tumor progression was conducted to dynamically characterize the change of the tumor microenvironment by multi-parameters and revealed the correlation of capillary flow rate, angiogenesis and tumor cell proliferation. We found there existed a steady increase of capillary flow and density during the first two weeks which reached their own peak 0.65± 0.19mm/s and 0.31±0.03 on Day 14, respectively. The increase of tumor angiogenesis was then followed by the boost of tumor size which started to expand exponentially on Day 14 and reached a measurable size of 17.16mm^2 on Day 24.

Analyzing the morphological feature of microvasculature in tumor microenvironment allows for identifying early tumor boundary during or before the formation of necrotic core. In the present study, we detected angiogenesis region with markedly high microvascular density ratio (109.10±35.64%) suggesting the tumor core massively recruited neo-micro vessels to meet the demand for fast proliferation and metabolism of cancer cells. Comparing to the conventional OCT that relies on the optical scattering contrast of necrotic core against the surrounding viable tissues[97], the μOCA based density ratio map provides superior sensitivity and specificity.

66

Because the necrotic core is still a small portion of the whole solid tumor during the early stage of tumor (Green Arrows, Figure 5-6a) and thus inaccurately reflects the true tumor size. On the contrary, the microvascular morphology based method relies on the intrinsic properties of angiogenesis tightly associating with the cell metabolism that started in the early stage of the tumor progression (Figure 5-7m) and therefore allows for precise detection of tumor boundary.

The longitudinal monitoring of tumor progression revealed the correlation between capillary flow, angiogenesis and tumor cell proliferation. Interestingly, the boost proliferation of tumor cells did not occur in the first two weeks however both capillary flow and density were actively growing. In addition, angiogenesis entered a plateau stage with slight decline in density and flow on Day 18 while the tumor size, however, increased exponentially to $4.15mm^2$. We hypothesized that the substantial difference between rapid cell proliferation and stagnating angiogenesis led to a huge deficit in metabolic supply and thus created hypoxic environment. Furthermore, as tumor growth continuing, the continuous metabolic deficit will lead to central apoptosis/necrosis and boundary angiogenesis which yields a ring shape in the density ratio map and thus can be used as a biomarker for boundary detection in the late stage of tumor growth [101].

In summary, we detected the early tumor boundary by analyzing the morphological feature of microvascular networks which allows for a superior sensitivity and specificity over the scattering based μOCT and white image. Additionally, the longitudinal tracking of tumor progression with multiple parameters characterizes the phase correlation between cell proliferation, angiogenesis and metabolic supply and provides the important clues for developing novel angiogenic or anti-angiogenic therapies for cancer treatment.

6. Cerebrovascular adaptation to cocaine-induced transient ischemic attacks in the rodent brain

Cocaine effects on the vascular system significantly contribute to the morbidity and mortality associated with its abuse [109-111]. In the brain the cerebrovascular effects of cocaine are associated with transient ischemic attacks (TIA) - a transient episode of neurological dysfunction without acute infarction, as well as full blown strokes (2). Clinically TIA is regarded as a portent of risk for subsequent ischemic stroke. In cocaine abusers TIAs are likely to reflect cocaine's vasoconstricting effects [112]. Indeed cocaine-induced vasospasm has been associated with sudden ischemia [113], and we recently showed that in rodents repeated cocaine exposures leads to microischemia and microvascular dysfunction [28]. Additionally, platelet aggregation[114] and accelerated atherosclerosis[115] contribute to vascular abnormalities in cocaine abusers. However, as of now there have not been any studies on cocaine induced TIA in animal models and hence information regarding the temporal course of cocaine-induced TIA and its recovery is not available [116]. Here we investigated the temporal course of cocaine-induced TIA in mice taking advantage of newly developed optical imaging tools.

Specifically, recent advances in optical imaging techniques, e.g., ultrahigh-resolution optical coherence angiography (µOCA) and Doppler tomography (µODT), have demonstrated their value for studying ischemic injury and neurovascular dysfunction[117], revascularization after traumatic brain injury (TBI)[118], capillary hypoperfusion after arterial occlusion[119], and microischemia after repeated cocaine exposures[28]. Here we used µODT/µOCA to study cocaine associated microvascular hypoperfusion, vasoconstriction and angiogenesis. We employed a chronic cranial window for longitudinal imaging of cerebral blood flow velocity (CBFv) in the mouse's sensorimotor cortex and in parallel monitored behavior (motor function) both during chronic cocaine exposure (35mg/kg/day, i.p.) and after cocaine withdrawal. We document that mice exposed chronically to cocaine showed vasoconstriction and hypoperfusion, which were abruptly exacerbated following an acute cocaine challenge that manifested as a TIA episode characterized by hemiparalysis. We also show evidence of vascular adaptions following a TIA that resulted in angiogenesis and cortical CBFv reorganization.

1. Methods
    1.1. Animals preparation

A total of 24 C57/B6 mice (male, 12-14 weeks of age, Jackson lab) were divided into two groups, controls and chronic cocaine groups in which animals received daily intraperitoneal (i.p.) injection of 0.9% saline (0.7cc/100g/day, N_{ct}=12) or cocaine (35mg/kg/day, N_{cc}=12) for 34 consecutive days, respectively. We this dose because it resulted in cocaine plasma levels consistent to those observed in cocaine abusers [120]. For the acute cocaine challenge procedure, animals received either an injection of 0.9% saline (0.7cc/100g, i.p.) or cocaine (35mg/kg, i.p.).

Mice were anesthetized with a mixture of 2.0-2.5% isoflurane in 100% oxygen. Then their heads were firmly affixed on a custom stereotaxic frame to minimize motion artifacts. In 7 control and 7 chronic cocaine mice, we placed two cranial windows (~2.5×2.5mm^2) above the left (0.25 to 2.75 lateral and -0.25 to -2.75 anterior to bregma) and the right (-0.25 to -2.75 lateral and -0.25 to -2.75

anterior to bregma) sensorimotor cortices and in 5 control and 5 chronic cocaine mice we placed 1 cranial window above the left sensorimotor cortex. The exposed cranial surface regions were covered with 2% agarose gel and affixed with 100μm-thick glass coverslip using biocompatible cyanocrylic glue. The physiological state of the mice, including electrocardiography (ECG), respiration rate and body temperature, was continuously monitored (SA Instruments, NY).

1.2. Behavioral recording

A behavioral recording chamber consisting of two 720p color video cameras placed orthogonally from top and one side of an uncovered rat cage was employed to record locomotor behavior. Locomotor behavior was recorded daily starting 5min prior to saline (0.7cc/100g, i.p.) or cocaine (35mg/kg, i.p.) injection (baseline period) and followed for 35min after injection (post-injection session). A total of 7 control and 7 chronic cocaine mice were recorded.

1.3. μODT/μOCA imaging

A custom ultrahigh-resolution optical coherence tomography (μOCT) system was used to acquire 3D cross-sectional dynamic images of the sensorimotor cortex through the cranial window over a relatively large field of view (e.g., FOV> 2×2×1mm^3) and at up to 147kHz axial scan rate (Chapter 2). The axial resolution of the μOCT image - determined by the coherence length ($L_c=2ln2/\pi\cdot\lambda^2/\Delta\lambda_{cp}$, λ=1310nm, cross-spectrum bandwidth $\Delta\lambda$cp≈200nm) of an ultra-broadband superluminescence diode - is 2.5μm, and its transverse resolution is 3.2μm as determined by the focal spot size of the microscope objective (f18mm/NA0.25). GUI programming for accelerating FFT image reconstruction and processing [28] was implemented to facilitate immediate display of microvascular morphology (3D μOCA) and blood flow velocity networks (3D μODT) at a B-scan updating rate of up to 473fps (2M pixels/s), a feature that is useful for locating regions of interest (RIOs) with disrupted/constricted vessels or microsichemia during image acquisition. Figure 6-1 illustrates the protocols for recording both behavioral videos and μODT/μOCA image sets during chronic cocaine administration.

1.4. Statistical analysis

Statistical tests were performed with SYSTAT Software (Chicago, IL, USA). Sample size for all in vivo experiments was determined using experimental data from other studies to approximate number of mice necessary to give >85% confidence for a twofold change in any given parameter at the P<0.05 significance level. Differences of CBFv, vessel diameter, flow decrease slope, VEGF upregulation were tested by 2-tailed t-tests or rank sum test. Rest-state flow differences before and after cocaine challenge of control was tested by paired t-test and the differences of CBFv decline between control and TIA mice was tested by unpaired t-test. Correlation coefficients between cortical hypoperfusion and locomotion were calculated using Pearson statistics. In the chronic window study, CBFv and microvascular density were tested for significant difference using one way repeated measure ANOVA followed by a post-hoc test (Holm-Sidak method). *P<0.05; **P<0.01,***P<0.001; NS denotes not significant. All data are presented as mean ± s.t.d.
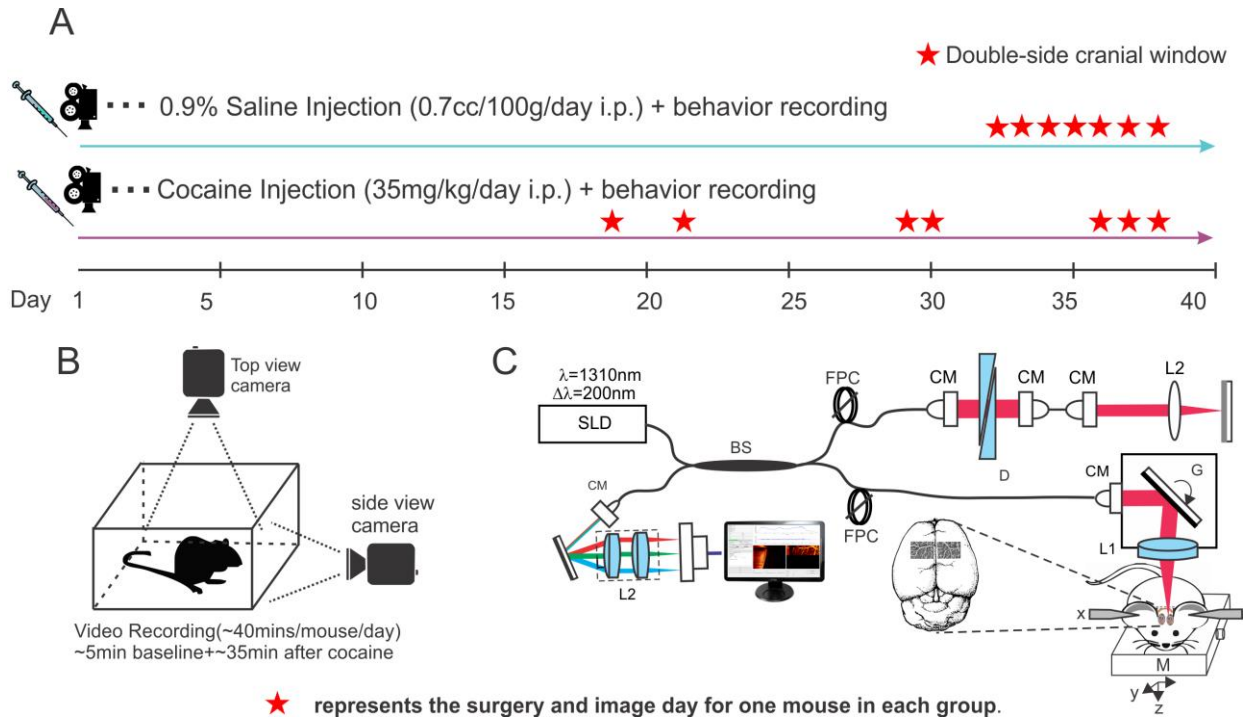
Figure 6-1 (**A**)14 C57BL/6J mice were split into two groups: control (n=7) and chronic cocaine (n=7) group, which were treated daily with 0.9% saline and with 35mg/kg cocaine (i.p.), respectively. (**B**) The behavioral motor responses were measured 5min pre-injection (used as baseline) and 30min post-injection using a dual-perspective camera system. (**C**) in vivo imaging by μODT/μOCA was conducted within 24 hours after the first appearance of hemiparalysis (described as TIA phase II).

2. Results
   2.1. Behavioral recording of TIA elicited by chronic cocaine:

The top panels in Figure1 compare snapshots of behavioral videos captured from the side-view and top-view cameras of control (Figure 6-2A upper two rows) and chronic cocaine mice (Figure Figure 6-2A lower two rows). Abnormal motor behaviors were observed in the chronic cocaine mice following an acute cocaine challenge. Specifically, after a short latency (3'17"±35", n=7) of increased locomotor activity following cocaine injection, all of the chronically cocaine exposed mice (n=7) exhibited disrupted motor behaviors that appeared as the onset of a TIA, which we describe as "Phase 1 TIA". Phase 1 TIA was characterized by slow and unsteady gait due to weak and clumsy hind limbs but no obvious hemiparalysis (Figure 6-2A Phase 1 TIA) and lasted 2'17"±46". Some mice developed more severe locomotor disruption, which we describe as "Phase 2 TIA" with symptoms of hemiparalysis (Figure 6-2A Phase 2 TIA). Phase 2 TIA was characterized by unilateral paralysis of the front and hind limbs that jeopardized the animal's forward movements and lasted 5'11" ± 2'19". During Phase 2 TIA, mice lost balance and kept turning in unilateral circles contralateral to the paralyzed limbs or laid on the floor (hemiparalysis). As the effects of acute cocaine subsided, the mice gradually recovered, which we describe as "Phase 3 TIA" regaining body balance but still showing stiff and staggering locomotion that lasted 8'21"±4'39", before they fully restored limb function. In contrast, the control animals after a

70

saline challenge maintained body balance and normal locomotion during the entire 33min monitoring period.
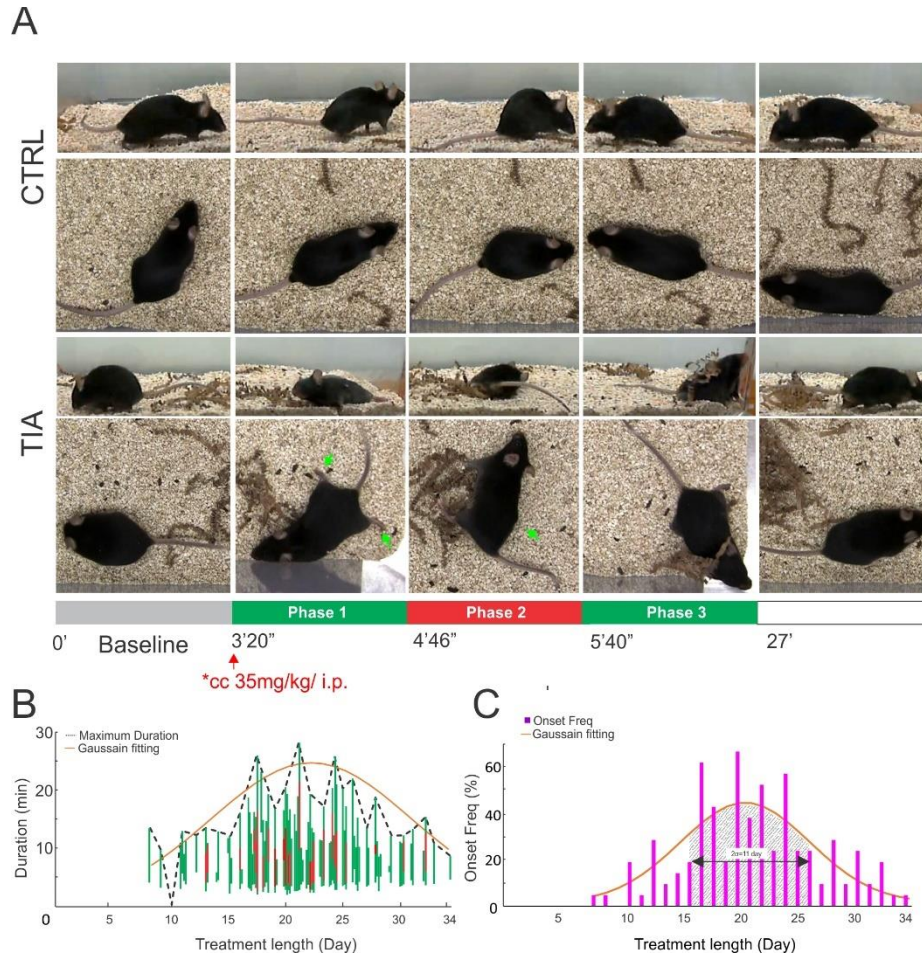
Figure 6-2 Behavior recording of difference TIA phases and its histogram distribution as a function of time (A) upper two rows: time-lapse video (side view and en-face view) snapshoots of a naïve mouse after saline injection (0.2cc, ip).(A) lower two rows: time-lapse video snapshoots of a chronic cocaine (TIA) mouse (day 18) showing TIA after an acute cocaine injection (35mg/kg, ip). TIA phases 1, 3, and 2 are highlighted by green and red bars, respectively. (**B**) TIA incidence rates and Phase 1, 2, 3 duration as a function of days of chronic cocaine treatment (n=7). (**C**) TIA severity index compounded by the TIA incidence rate and total TIA duration

Figure 6-2B plots the averages for the prevalence and duration of TIA behavioral episodes in response to acute cocaine as a function of the days of cocaine exposure. The TIA severity index (Figure 6-2C) expressed as the rate of TIA and the duration of Phases 1, 2 and 3, started to increase after day 8, reached its extremes near days 17-24, but gradually declined thereafter. The decline in TIA's severity with time suggests that there was some degree of vascular recovery or of tolerance to cocaine's vascular effects with chronic administration.

2.2. Hypoperfused sensorimotor cortex contralateral to TIA hemiparalysis

71

The analysis of locomotor behavior suggested that hemiparalysis was an eminent behavioral pattern characteristic of TIA, which led us to hypothesize that it would be associated with cerebrovascular dysfunction in the contralateral sensorimotor cortex. To test this hypothesis, we opened two cranial windows over the sensorimotor cortices of each hemisphere on mice (on 7 control and 7 cocaine mice, we opened only one chronic cranial window on the left sensorimotor cortex, see Table 1) who had exhibited locomotor signs of TIA onset the day before so that we could perform µODT/µOCA scans. Unlike the bilateral CBFv networks of a control mouse, which were high and comparable (Figure 6-3A upper panels), those in a TIA mouse (Figure 6-3B upper panels) were drastically reduced leading too bilateral cortical hypoperfusion and unbalanced lateralized perfusion. For example, for a mouse showing right hemiparalysis (Figure 6-3B lower panels) the CBFv disruption and ischemia on the contralateral (left) sensorimotor cortex was significantly (p<0.001, Figure 6-3B upper left) larger than that in the ipsilateral cortex (right) (Figure 6-3B upper right). Moreover, there was a strong correlation (r=1, n=7) between hemiparalysis and CBFv dysfunction (ischemia) in the contralateral sensorimotor cortex. Specifically, among the 7 chronic cocaine mice in whom we recorded motor behavior and performed µODT scans of CBFv in left and right sensorimotor cortices, 5 showed right hemiparalysis and lower CBFv in left sensorimotor cortex, 2 showed left hemiparalysis and lower CBFv in right sensorimotor cortex. Thus, hemiparalysed limb locomotion was associated with a more severe hypoperfusion of the contralateral than the ipsilateral sensorimotor cortex consistent with the notion that the motor disruption reflected a TIA. Interestingly, the left sensorimotor cortex appeared to be more vulnerable to chronic cocaine elicited TIA (n=5) than the right (n=2) (p=0.008).
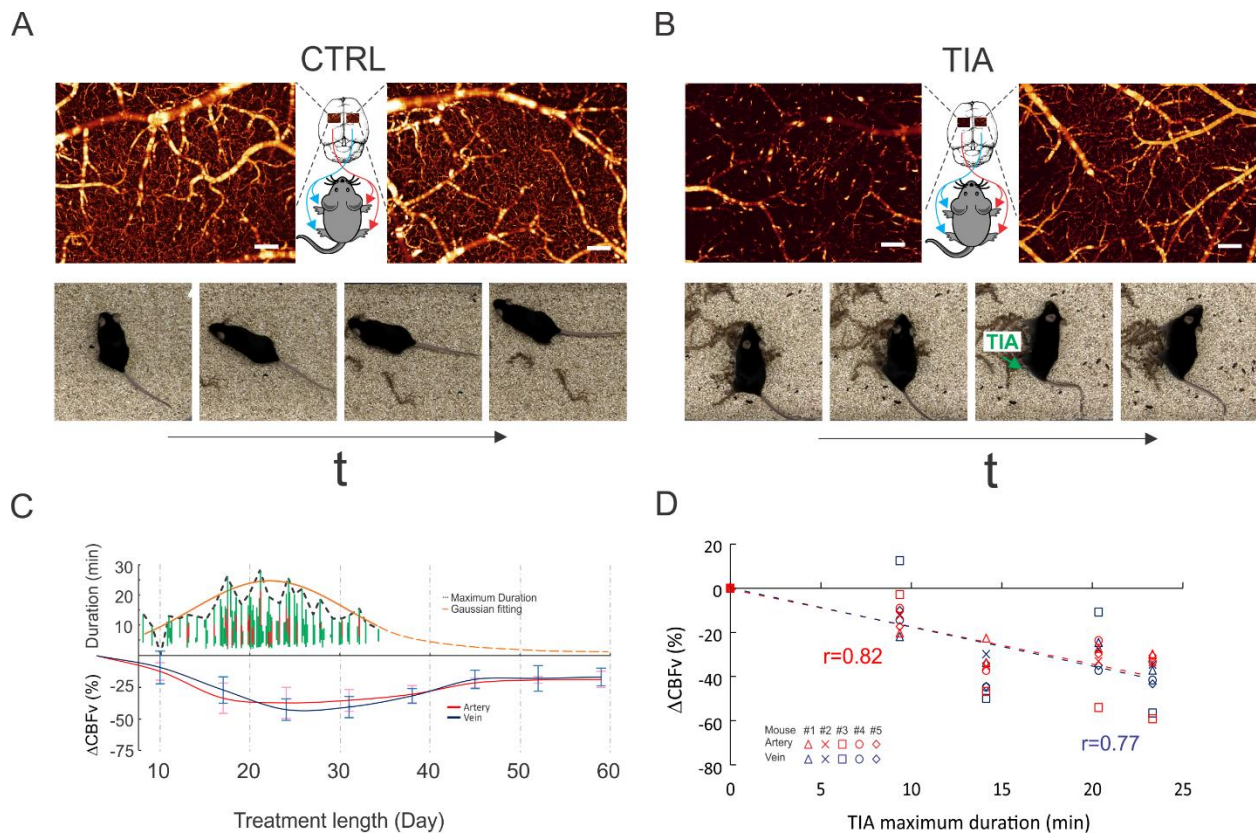
Figure 6-3 Representative μODT images of the sensorimotor cortex with behavioral images between a control mouse (A) and a TIA mouse (B) after chronic cocaine exposures, and temporal relationship between the TIA incidences and the cortical CBF changes of animals. (A) μODT images of left and right sensorimotor cortices of a control mouse and behavior recording of normal limb locomotion after saline injection .**(B)** μODT images of left and right sensorimotor cortices of chronic cocaine mouse and behavior recording of hemiparalysed limb after acute cocaine (35mg/kg, ip). **C).** Time courses of TIA incidences (n=7) and the CBFv decreases in arteries and veins of the brains (n=5), indicating that ΔCBFv decreases precede the TIA. **D)**. Correlation analysis between ΔCBFv (%) and the maximal duration of TIAs, indicating that TIA were associated with the CBF decrease in the cortical vessels (r=0.82 for arteries, and 0.77 for veins). Scale bar: 200μm.

Figure 6-3C summarizes the longitudinal assessments of TIA episodes and vascular CBFv changes (ΔCBF). It shows that TIAs started to emerge approximately after 11 days of chronic cocaine exposure at which point CBFv in arteries and veins was about 12.38±6.88% and 9.17±12.92% lower than baseline, respectively. Continued repeated exposure led to progressive hypoperfusion in arteries and veins in parallel to an exacerbation of the TIA. Figure 6-3D shows the correlation between TIA duration and CBFv decreases (compared to baseline) revealing that the greater the flow decrease the longer the duration of the TIA (r=0.733, p<0.0001).

2.3. Imbalanced flow deficit

Figure 6-4 shows quantitative comparisons of CBFv between the left and the right sensorimotor cortex of a control (upper panels) and of a TIA mouse (lower panels). Figure 6-4B and 3C show the comparisons of the absolute flow rates in arterial, venous and capillary compartments between the TIA side and non-TIA side of the sensorimotor cortices of TIA mice (n=7).

Overall, CBFv in sensorimotor cortices were significantly diminished in TIA mouse compared to control mouse and were lower in the contralateral side to the paralysis than in the ipsilateral side (Fig 3A). Specifically, capillary CBFv was 0.23±0.03mm/s in somatosensory cortex of control mice (n=7) whereas it was 0.08±0.05mm/s on the contralateral side (67.67±19.01% lower; p<0.001) and 0.17±0.05mm/s on the ipsilateral side (30.15±15.30% lower; p=0.014) of the TIA side (n=7).
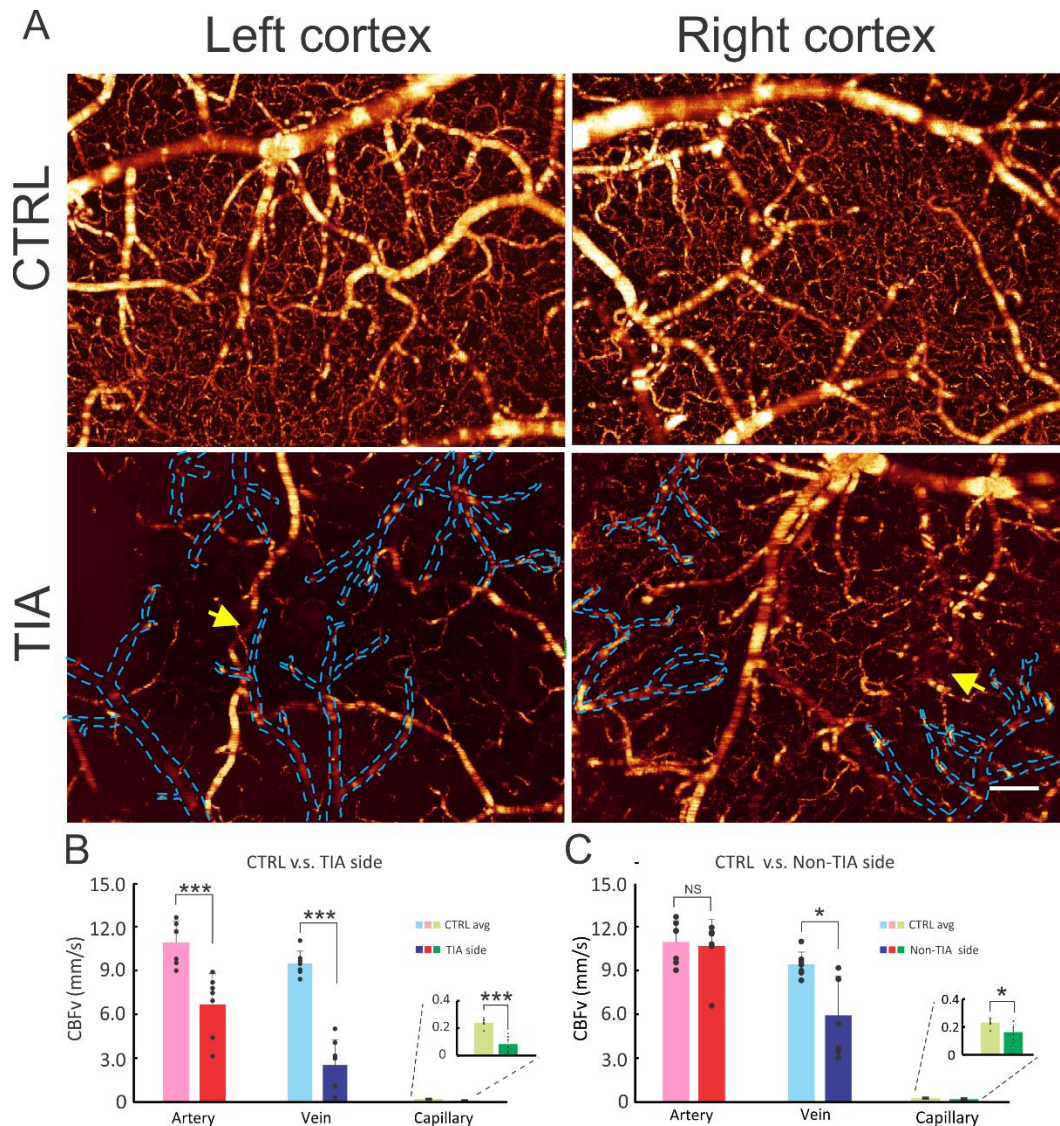
Figure 6-4 Disparity of cocaine elicited CBFv decreases between left and right sensorimotor cortex by 3D μODT. (A) CBFv network of mouse sensorimotor cortex imaged by 3D μODT (upper row: control mouse lower row: TIA mouse). TIA in left sensorimotor cortex correlated with the right limb hemiparalysis. (**B**) and (**C**) statistic figures of CBFv rates in arterial, venous, and capillary compartments of left (TIA) and right (non-TIA) sides, respectively. Yellow arrows point to suspected arterial stenosis and dashed blue lines outline undetectable venous flows. n=7 for each group, *P<0.05, **P<0.01, ***P<0.001, and NS denotes not statistically significant. Unpaired 2-tailed Student's t tests or rank sum test were performed for statistical analysis and average values are shown as the mean + s.t.d in **B** and **C**. Scale bar: 200μm.

Venous flow was also markedly decreased in mouse suffering from a TIA when compared to control mice (9.45±0.85mm/s), corresponding to 2.57±1.75mm/s on the TIA side (decline of 73.96±16.27%; p<0.001) and 5.98±2.66mm/s on the non-TIA side (decline of 38.15±23.44%; p=0.011). Similarly, arterial flow was significantly decreased from 10.99±1.45mm/s in controls to 6.74±2.12mm/s on the TIA side (decline of 39.88±13.86%, p<0.001), though the non-TIA side did not differ from control (10.71±1.85mm/s; p=0.620).

In addition to hypoperfusion in both sensorimotor cortices, a severe flow disparity was observed between the TIA and non-TIA sides. For instance, the arterial, venous, and capillary flows on the TIA side were 38.25±12.30% (p=0.011), 61.39±16.27% (p=0.015), and 56.87±18.57% (p=0.010) lower than on the non-TIA side, which is consistent with the findings of a predominant presentation of hemiparalysis rather than of complete paralysis (Figure 6-2A TIA phase 1).

2.4. Vasoconstriction as a portent of TIA onset:

Chronic cocaine is likely to elicit hypoperfusion in part by triggering vasoconstriction. In order to assess the contribution of vasoconstriction to TIA we conducted vascular images using µOCA. Figure 6-5 shows the corresponding 3D vasculature images (µOCA) of Figure 6-4, in which the vessel sizes of arterial and venous compartments of control and chronic cocaine mice are compared. Statistical analysis across different animals shown in Figure 6-5B and C indicate vasoconstriction in TIA mice. The analyses revealed that vasoconstriction occurred predominantly in the venous compartment. Specifically, the mean diameter of veins was most markedly decreased on the TIA-side from 72.45±11.06µm to 50.81±14.4µm (30.8±11.6%, p=0.008) and less so on the non-TIA side to 58.46±11.26µm (19.7±5.7%, p=0.037). In contrast, vasoconstriction in arterial vessels was not significant, which were reduced by only 9.7±7.8% (p=0.385), from 38.66±9.34µm to 34.57±7.54µm on the TIA side, and 4.3±15.6% (p=0.480) to 35.85±4.11µm on the non-TIA side.

It is noteworthy that in contrast to the marked laterality in the CBFv decreases (Figure 6-4), the laterality differences in vasoconstriction, though showing some degree of diameter decrease on the TIA side compared to contralateral side (5.7±11.2% for arteries, 17.94±13.19% for veins), were not significant.
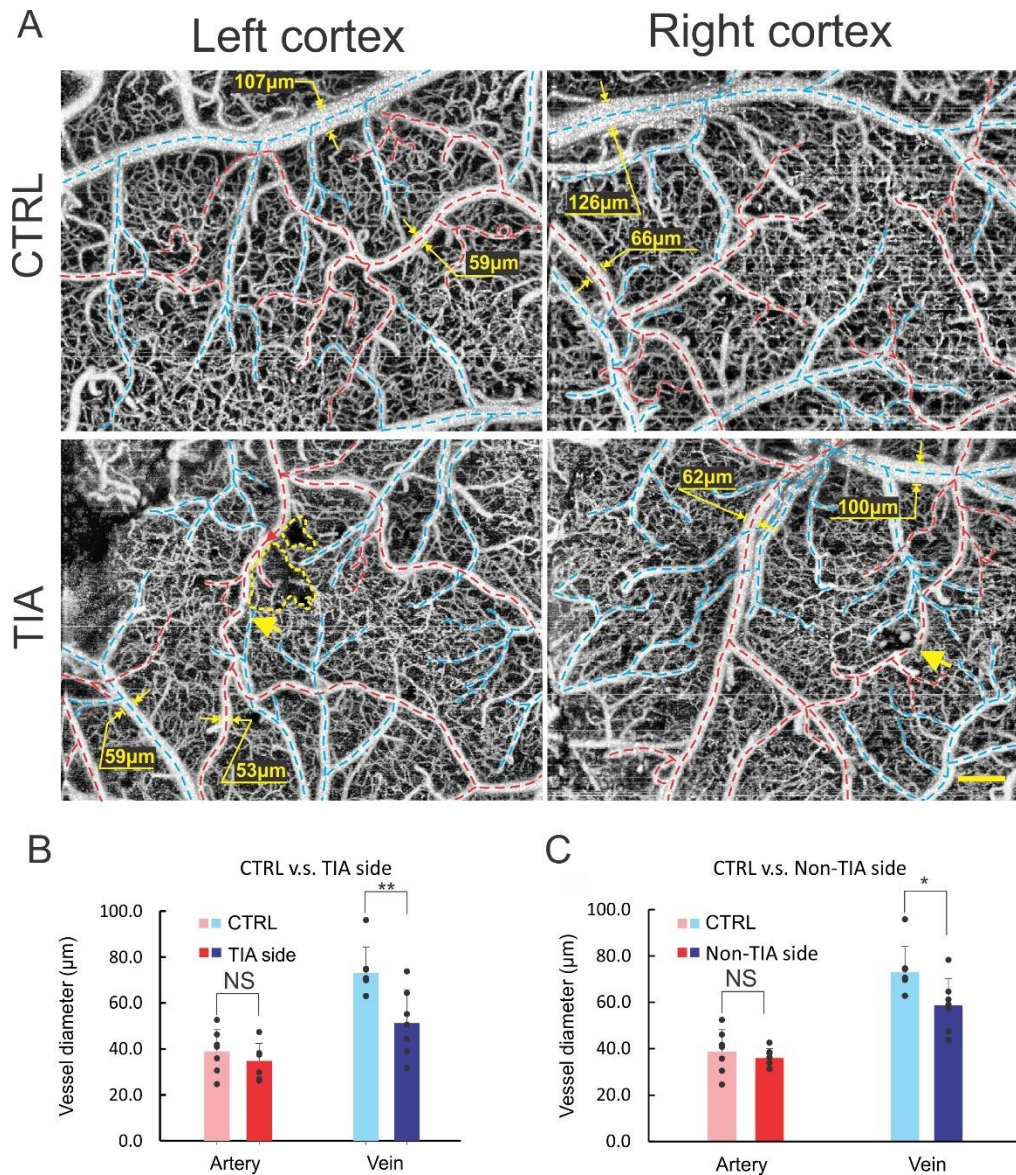
Figure 6-5 Cocaine elicited vasoconstriction of left and right sensorimotor cortices by 3D μOCA. (A) Cerebral vascular network of mouse sensorimotor cortices imaged by 3D μOCA (upper row: control mouse lower row: TIA mouse). (**B**) and (**C**) statistic figures of arterial and venous vessel sizes in left (TIA) and right (non-TIA) cortices, respectively. Yellow arrows point to arterial stenosis and dashed yellow lines outline the resultant disruption of local capillary networks. Dashed red/blue lines: arterial/venous vessels. n=7 for each group, *P<0.05, **P<0.01, ***P<0.001, and NS denotes not statistically significant. Unpaired 2-tailed Student's t tests were performed for statistical analysis and average values are shown as the mean + s.t.d. in **B** and **C** Scale bar: 200μm.

The discrepancies between the association of flow decreases and vasocontraction for veins but not for arteries might reflect the fact that arterial stenosis can occur on a regionally localized section of the arterial vessel whereas vasoconstriction of veins is more likely to be present throughout the entire length of the vessels. Indeed, the μOCA reveals highly localized areas of stenosis in the arterial vessels (e.g., 2 yellow arrows in Figure 6-5A, left side of TIA panel), which appear as areas of flow discontinuity in the μODT images (yellow arrows in Figure 6-4A, left side of TIA panel).

In addition, the local capillary networks near the arterial stenosis were disrupted as shown in Figure 6-5A (e.g., the area marked by the yellow dished-lines, left side of TIA panel). In contrast, the µOCA reveals narrowing of veins throughout the length of the vessel. The significant decreases in venous diameters in the chronically cocaine exposed mice is likely to reflect both adaptations to accommodate the reduced flow to the tissue to avoid inflow/outflow, as well as the direct vasoconstricting effects of cocaine to venous vessels[121, 122].

2.5. CBFv dynamic response to acute cocaine challenge

Figure 6-2 reveals that the TIA onset including the emergence of hemiparalysis in the chronic cocaine mice were transient and occurred 2~3min after acute cocaine (35mg/kg, *i.p.*) recovering in <~20min. The occurrence of the TIA following an acute cocaine injection only after the mice had received repeated cocaine doses suggests that it is likely a compounding effect of both severe basal hypoperfusion (Figure 6-4) secondary to chronic vasoconstriction (Figure 6-5) plus the additional CBF disruption triggered by the acute cocaine injection. Thus, we assessed the normalized dynamic response of CBFv in chronically cocaine exposed mice following an acute cocaine injection, i.e., $\Delta CBFv(t)=[CBFv(t)-CBFv(t_b)]/CBFv(t_b) \times 100\%$, where $CBFv(t_b)$ is the averaged CBFv value before the acute cocaine injection ($t_b \leq 0$ min), and compared them to the responses of control mice when given an acute cocaine injection. Figure 6-6 shows the dynamic CBFv responses of a control mouse (upper panel) vs a TIA mouse (lower panel) to an acute cocaine injection (35mg/kg, *i.p.*), in which panels (**B, E**) plot the time-lapse $\Delta CBFv$ in arteries (red traces), veins (blue traces) and capillaries (green traces), respectively. As expected, $\Delta CBFv$ decreased in both control and TIA mice in response to acute cocaine. However, quantitative analyses by linear least squares fits (dashed lines) show a ~9.5-fold steeper slope of the arterial $\Delta CBFv$ decrease in the TIA mouse (-11%/min) than in the control mouse (-1.23%/min), indicating that the flow disruption in the sensorimotor cortex of the TIA mouse was significantly faster than in the control mouse (*p=0.014 and *p=0.016 for arterial and venous flows, respectively). Interestingly, despite the basal hypoperfusion in TIA mice (e.g., Figure 2), they still show greater ΔCBF decreases in response to acute cocaine than the control mice, in arteries -38.56% v.s. -22.97%, veins -46.76% v.s. -24.82%, and capillaries -60.55% v.s. -29.72%. These results reveal that the low basal CBFv due to chronic cocaine is further disrupted by acute cocaine, which leads to an abrupt flow decrease that triggers the TIA and the associated hemiparalysis.
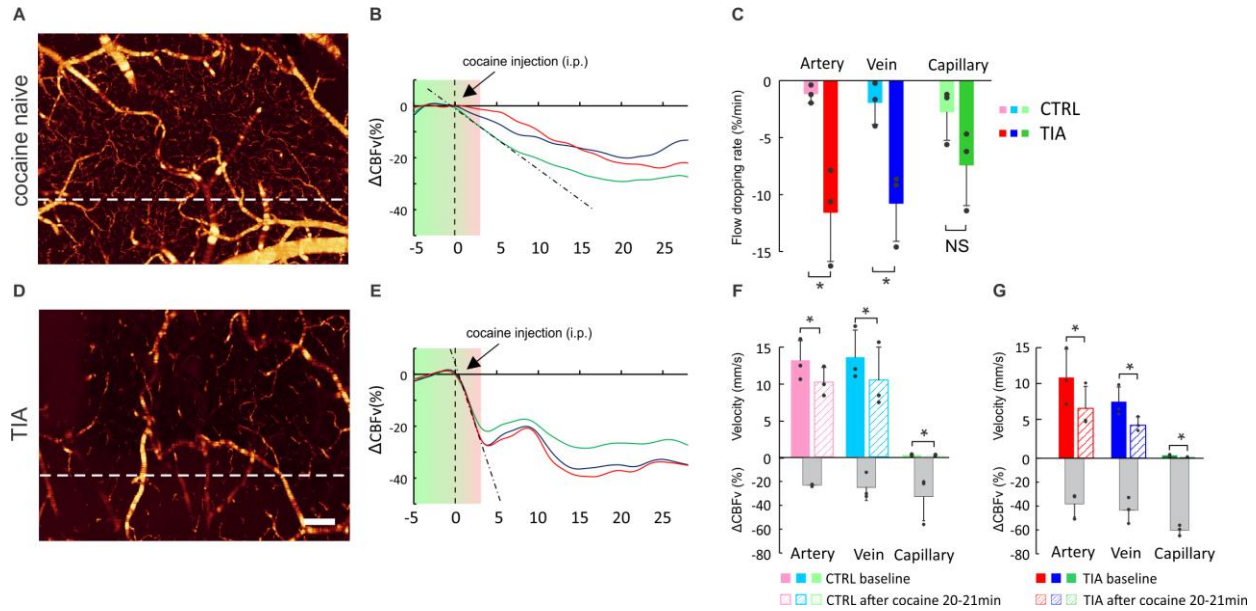
Figure 6-6 Comparison of CBFv dynamic responses to acute cocaine challenge between control and TIA mouse. (A) and (D) are the baseline μODT image of control and cocaine mouse with B-scan position highlighted by white dashed line whose time-course curve are plotted in (**B**) and (**E**) containning multiple artery (red), vein (blue) and capillary (green). The black dashed lines in b) and e) are the linear curve fitting for artery flow decrease within the first 2.5min after cocaine injection whose statistical comparision is presented in (**C**). The period shaded with green-to-red gradient represents the latency. (**F**) and (**G**) are CBFv comparison of artery, vein and capillary between pre- (-5~0min) and post injection (20~21min) session for control and cocaine treated mice, repsectively, in which the oranges bars show relative decreases in flow (%). n=3 for each group, *P<0.05, **P<0.01, ***P<0.001, and NS denotes not statistically significant. Unpaired 2-tailed Student's t-tests were performed for (**C**) and paired t-tests were performed for **F**) and **G**) Average values are shown as the mean + s.t.d in (**C**), (**F**), and (**G**). Scale bar: 200μm.

2.6. CBFv reorganization in deep sensorimotor cortex

Figure 6-2 shows that cocaine-elicited TIA occurred most frequently within 17-24 days of chronic cocaine exposures but then the incidence and severity decreased despite continuous cocaine daily exposures. Such intriguing behavioral patterns led us to investigate the underlying mechanisms that prevented TIA deterioration. For this purpose, we performed longitudinal *in vivo* μODT/μOCA imaging of mice every 4 days during chronic cocaine exposures through a chronic cranial window. Specifically, focal tracking was implemented to image both superficial layers (L1, L2/3: 0-300μm) and deep layers (L4, L5: 400-600μm) where thalamocortical inputs play a critical role in motor control[123, 124]. Surprisingly, we observed that chronic cocaine elicited CBFv network reorganization across superficial and deep cortical layers as shown in Fig. 6. For control mice (left panels), μODT images show almost no difference between day 8 and day 28, e.g., high CBFv in superficial layers and low in deep layers. In contrast, in chronic cocaine mouse, the CBFv networks (e.g., in arterial, venous and capillary vessels) in superficial layers were significantly decreased (p=0.028, n=5) consistent to those shown in Figure 2-3 that imaged superficial cortical layers, whereas the capillary ΔCBFv (i.e., $\Delta CBFv=[CBFv-CBFv_b]/CBFv_b\times100\%$, (where $CBFv_b$ is the flow rate on day 0), in deep layers was significantly increased.
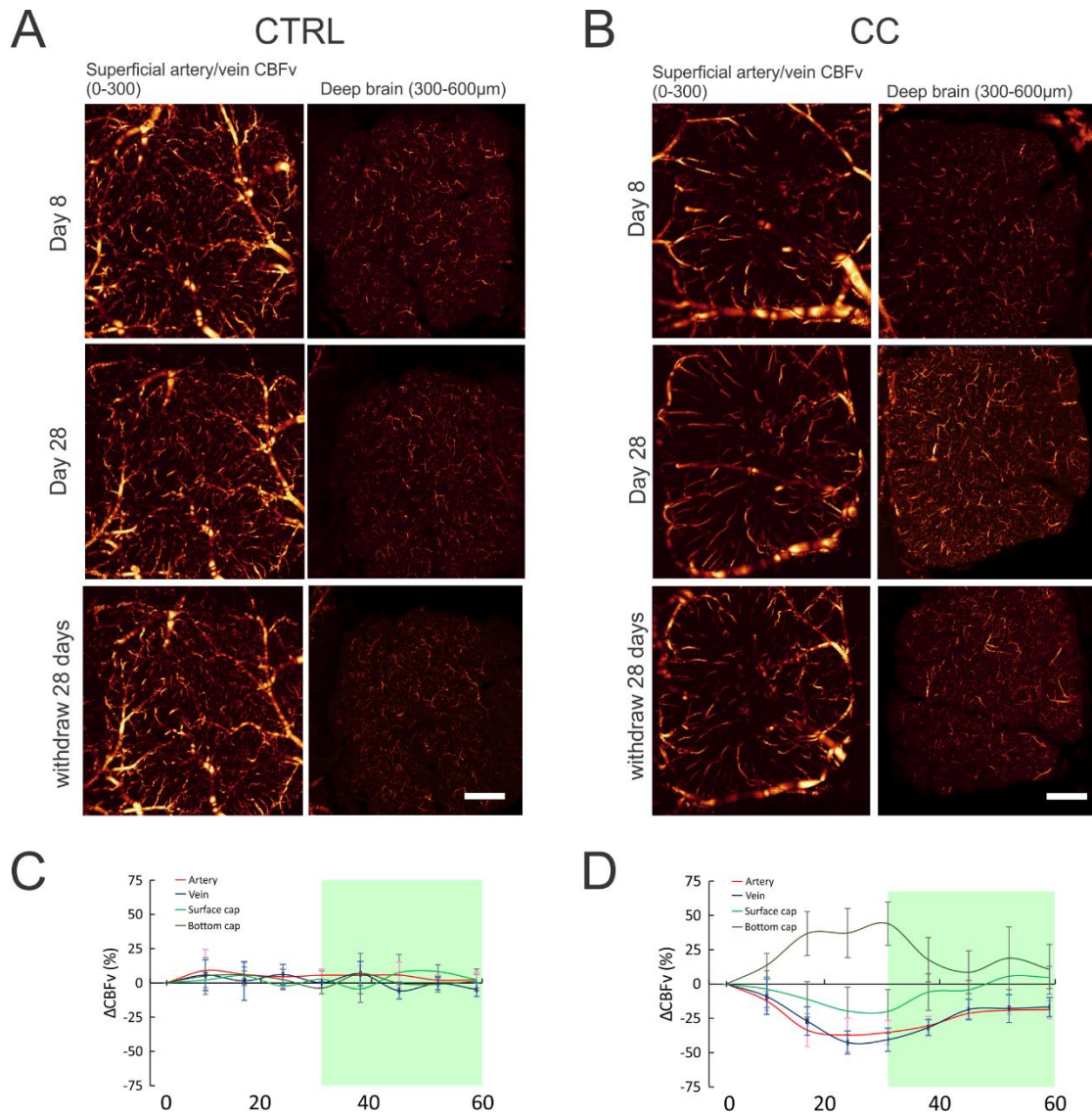
Figure 6-7 **Chronic cocaine elicited CBFv reorganization in the sensorimotor cortex.** (**A**) µODT images of superfical (a, c: L1, L2/3, 0-300µm) layers and deep cortical (b, d: L4, 300-600µm) layers of a control mouse aquired day 8 and day 28 through a chronic cranial window.(**B**) mouse undergoing chronic cocaine exposures (35mg/kg/day, ip). (**C**) and (**D**): time courses of ΔCBFv (%) in arteries (red), veins (blue), superficial (orange) and deep (green) capillaries in control (n=5) and chronic cocaine (n=5) mice, respectively. Scale bar: 500µm.

Statistical figures of time-lapse flow image analyses in Figure 6-7C and D indicate that the superfical CBFv networks in control mice remained largely unchanged. In chronic cocaine mouse, superficial arterial ΔCBFv (red trace) decreased to -33.59±11.94% between day 17-32, and then after cocaine withdrawal slowly recovered to -21.41±3.85% at day 42 with no further changes thereafter. Although slightly delayed, superficial venous ΔCBFv (blue trace) also decreased to -42.63±8.50% by day 22-32, and then slowly recovered after cocaine withdrawal to -18.66±7.36% at day 42 (partial recovery). Superficial capillary ΔCBFv slowly decreased to -19.64±17.29% around day 25-32, and then after cocaine withdrawal it almost recovered near day 38 followed by a slight overshoot (p=0.935, n=5).

In contrast, deep capillary ΔCBFv significantly increased 36.75±16.04% (p<0.001, n=5) by day 17 and remained high till day 32 when cocaine was withdrawn, after which it rapidly declined to 8.58±15.62% (p=0.309, n=5) around day 42 but did not fully return to its baseline. Also, Figure 6-7B Day 28 reveal that many vascular flow sections are longer, which is consistent with an increase of flow routing to the deep cortical layers.

2.7. Angiogenesis and VEGF upregulation

We hypothesized that hypoxia driven angiogenesis, which is a well-documented process in stroke and in the tumor microenvironment, underlie the slow recovery and reorganization of flow observed with protracted cocaine exposure. Consistent with this hypothesis we show in Figure.7 that chronic cocaine-induced vasoconstriction of arteries and veins (μOCA Day 28 v.s. Day 8) occurred in parallel to an increase in microvascular density, i.e., angiogenesis in deep cortical layers (Density map Day 28 v.s. Day 8). Quantitative analysis based on image segmentation and vessel tracking[125] showed (Figure 6-8C) that between day 0 and day 31 there were no significant changes in microvascular density in superficial layers (-4.18±14.72%, p=0.484; green trace) but there were significant increases (21.04±11.98%, p=0.006) in deep cortical layers (dark trace). The increases in vascular density in the deep cortical layers correlated with the time of greatest vasoconstriction in the venous vessels (blue trace in Figure 6-8B), suggesting that angiogenesis following chronic cocaine exposure was triggered by vasoconstriction-induced ischemia. This was further cross-validated by *ex vivo* VEGF fluorescence microscopy, which showed significant VEGF upregulation in the deep cortical layers (152.50±15.56%, p=0.002) after 4-week cocaine exposures and a fallback to 87.73±8.71% (p=0.105) after 28 days of cocaine withdrawal. Interestingly VEGF was also significantly increased in superficial layers (202.83±83.64%, p=0.032) at 4 weeks and then fallen back to 99.89±27.90% (p=0.995) after 28 days of withdrawal.
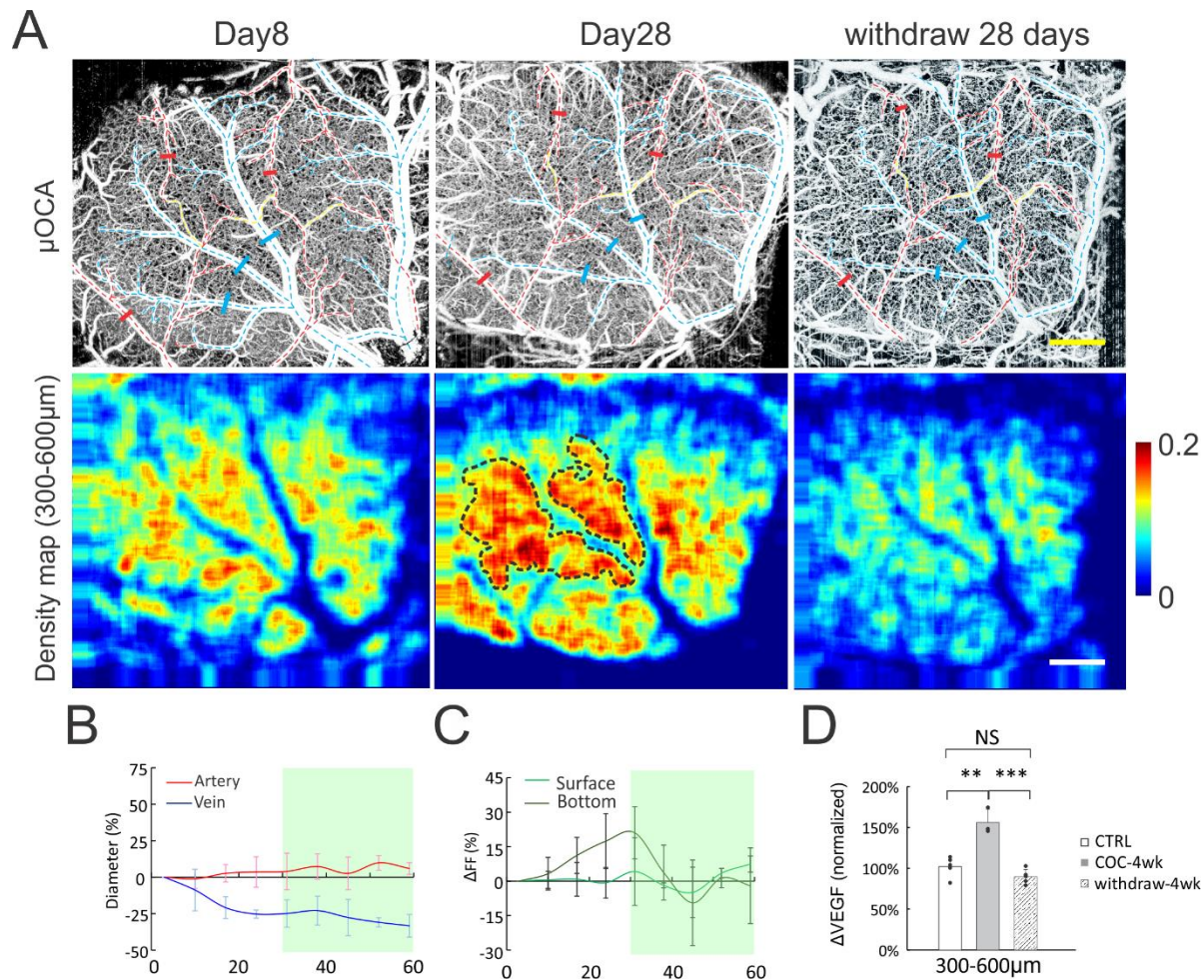
Figure 6-8 Cocaine elicited vasoconstriction in superficial layers and angiogenesis in deep layers of the sensorimotor cortex. (A) upprer row: Cerebrovascular images acquired with µOCA on day 0 and day 28 after cocaine exposures (35mg/kg/day, ip); arterial and venous vessels are marked in red and blue dashed lines, solid bars are marked for vessel size quantification. (A) lower row: corresponding microvasculature density maps of deep layers, dashed black circles outline the regions of most eminent angiogenesis surrounding areas with vessel vasoconstriction. (B) time-lapse vasoconstriction in arteris and veins, (C) time-lapse microvascular density changes in superfical and deep cortical layers, (D) VEGF upregulation. *P<0.05, **P<0.01, ***P<0.001, and NS denotes not statistically significant. Unpaired 2-tailed Student's t tests were performed for statistical analysis and average values are shown as the mean + s.t.d in (D) with n_{ctrl}=5, n_{4w-cc}=3, and $n_{withdraw}$=5. Scale bar: 500µm.

3. Conclusions & Discussions

In this paper, we show that in chronically cocaine exposed mice the abrupt exacerbation of vasoconstriction and hypoperfusion triggered by an acute cocaine challenge, led to cortical ischemia and the emergence of a TIA. We also show that chronic cocaine gradually resulted in a redistribution of flow from superficial to deep cortical layers and led to angiogenesis in deep cortical layers that, we hypothesize, prevented further deterioration of the TIA with continuous cocaine use. This study for the first time shows evidence of a TIA in an animal model of chronic cocaine exposure that allowed us to investigate the longitudinal changes in the cerebrovascular networks associated with TIA subjected to protracted cocaine exposure. This allowed us to show that: 1) chronic cocaine exposure induces severe vasoconstriction and hypoperfusion, which is exacerbated during acute intoxication, triggering TIAs that presented as transitory hemiparalysis; and 2) vascular adaptations including CBFv reorganization from superficial to deep cortical layers along with angiogenesis that prevented further exacerbation of TIA with continued cocaine exposures.

Our results corroborate prior findings from our group that chronic cocaine enhances the vasoconstricting effects and the decreases in CBFv triggered by an acute cocaine challenge, thus leading to ischemia [126]. Here we expand our understanding by documenting that this sensitized vascular response is responsible for the emergence of the TIA.

Furthermore, our longitudinal design allowed us to monitor for the first time the emergence and severity of the TIA as a function of days of cocaine exposure, and showed that while TIA severity peaked around 17-24 days it declined thereafter, which was suggestive of a compensatory response to counteract the hypoperfusion.

The quantitative capability of our imaging tools with their high temporal and spatial resolutions allowed us to monitor dynamic changes in the cerebrovascular networks. We found the CBFv was decreased in chronic-cocaine animals across the vascular network including arteries, veins and capillaries, which is in agreement with clinic finding of CBF reduction in cocaine abusers [127]. In addition, we observed evidence of arterial stenosis in the cortex of TIA animals (e.g., Figure 6-5 above) that was associated reduced CBFv in microvascular networks in the surrounding local area (e.g., yellow dishes marked in Figure 6-5). Though we are interpreting the reductions in CBFv to reflect arterial vasoconstriction we cannot rule out the contribution of micro-thrombosis. Indeed, clinical studies have reported both vascular stenosis [128] and micro-thrombosis in cerebral and coronary arteries of cocaine abusers [129, 130]. The parallel time-lapse imaging allowed us to assess the associations between TIA hemiparalysis and CBFv disruption elicited by chronic cocaine. Though prior studies had shown decreases in cortical CBF[131] in cocaine abusers and in animal models of chronic cocaine exposures, the enhanced spatial resolution of our imaging tools allowed us to quantify flow in various vascular compartments and to link these, for the first time, with the associated behavioral deficits. Noteworthy was the marked reduction of flow in capillaries (67% reduction on the TIA side and 30% on the non-TIA side) prior to the acute cocaine challenge. This marked flow deficit in the resting state could be regarded as a portent for TIA, particularly when further challenged with an acute dose of cocaine.

Our findings indicate that the TIA is triggered by both pronounced and sustained CBFv decreases from the chonic cocaine exposure along with an abrupt exacerbation of the CBFv decreases during intoxication (~9.5× steeper flow drop in response to an acute cocaine challenge). Although decreases in resting-state flow could result in impaired neuronal function due to the tight coupling between neuronal activity and CBF, these resting flow reductions by themselves did not account for the TIA paralysis, which manifested only after an acute cocaine exposure. We postulate that this abrupt decrease in CBFv interferes with the buffering capacity of the vascular system to compensate for regional hypoperfusion. Indeed, abrupt perturbation of CBF can trigger symptom presentation in vascular diseases in other organs such as lung and heart[132, 133].

Intriguingly, motor behavior in the chronic cocaine exposed mice recovered within 14'28"±2'30" after an acute cocaine challenge even though they still had marked deficits in arterial (38.56±11.00%), venous (43.88±10.89%) and capillary (60.55±4.44%) perfusion. This is suggestive of an uncoupling between neurophysiological and cerebral vascular deficits, which is a phenomenon that has previously been reported clinically is disorders associated with cerebral ischemia [134, 135].

Our findings revealing flow redistribution from superficial to deep cortical layer, increases in vessel density, and increases in VEGF suggest that these compensatory responses might have prevented further deterioration of the TIA despite continuous cocaine use. Ischemia triggered by cocaine is likely to have stimulated angiogenesis as has been shown to be the case for animal models of cerebral stroke[136]. Indeed prior studies showed that chronic cocaine elicited marked HbO_2 decreases along with an upregulation of VEGF and HIF that were interpreted to reflect hypoxia-driven angiogenesis [137], Similarly upregulation of platelet derived growth factor (PDGF) after chronic cocaine was interpreted to reflect an increase in vessel permeability that might indirectly stimulate angiogenesis[138]. Apart from ischemia, it is also plausible that the serotonin enhancing effects of cocaine might have also contributed to angiogenesis for sustained administration of serotonin reuptake inhibitors (SSRI) has been shown to improve recovery of stroke, in animal models and in humans[139, 140]. Inasmuch, as cocaine like SSRIs, blocks serotonin transporters [141, 142], this effect could have accelerated the recovery associated with its vasoconstricting effects.

Additionally, collateral circulation determines the fate of salvageable ischemic tissue and its augmentation is widely regarded as a promising therapeutic approach to stroke or ischemia. However, technical limitations of image resolution or depth of prior imaging studies of TIA had prevented the assessment of flow across different cortical layers. Here, we were able to longitudinally image CBFv networks across cortical L1-L6 in chronic cocaine mice for 9wks (5wk cocaine treatment and 4wk withdrawal). The observed 36.75±16.04% increase of capillary CBFv in deep cortical layers (L3-L5: 300-600μm) was likely due to enhanced collateral circulation to compensate for flow deficits. The reorganization of CBF from superficial to deep cortical layers in the somatosensory cortex[143] was associated with longer vessels reaching the deep cortical layers and with significant increases in VEGF. Vascular networks across cortical layers are heterogeneous[144] and thus this could account for the differences in the vascular responses to chronic cocaine between the superficial and the deep cortical layers. However, they could also reflect differences in neuronal demand needs, vascular innervation, or collateral perfusion between the deep and the superficial cortical layers[145]. Alternatively they could also reflect differences in neuronal sensitivity to cocaine as shown by the higher sensitivity of superficial layers to cocaine's enhancement of sensory signals than that of deep cortical layers[146].

Inasmuch as the vascular adaptations that we report in our model of chronic cocaine exposure are analogous to those reported in animal models of arterial occlusion [108], which benefited from proangiogenic therapies. This would suggest that similar strategies might be beneficial to help enhance brain recovery after cocaine-induced ischemia [147] [148]. Thus, our findings are clinically relevant which suggest that enhancing angiogenesis might prevent strokes in cocaine abusers and improve recovery in cocaine abusers suffering from strokes or TIA presentations. Similarly, it suggests that other pharmacological interventions shown to be beneficial in enhancing recovery from stroke such as SSRIs might also help prevent and/or accelerate recovery from ischemia in cocaine abusers. Additionally, the characterization of the development of TIA and emerging angiogenesis with repeated cocaine exposure, provides a model with which to test therapeutic strategies to minimize cocaine-induced hypoxia that could be clinically beneficial.

In interpreting our findings, it is important to address its limitations. Most notable of which is the limitation of translating findings in an animal model to the human condition, which is a universal confound in preclinical studies. Indeed, cocaine abusers frequently consume multiple drugs (i.e. nicotine, alcohol) and might inject contaminants (i.e. procainamide) all of which can contribute to cocaine associated strokes and TIA whereas we only administered cocaine to our animals which is not a self-administration model. However, this rather than detract enhances the value of our findings for it indicates that cocaine by itself is able to induce cerebrovascular pathology, which in humans might be further exacerbated by co-morbid use of other drugs or contaminants. Also while multiple studies have given cocaine to rodents this is the first one to report a consistent emergence of a TIA with chronic cocaine, which raises the possibility that the strain of mice (C57/B6 mice) was particularly sensitive to cocaine-induced vascular dysfunction and questions its generalizability to other strains. However, this is not different from the diversity seen clinically. Indeed, cerebrovascular pathology does not occur in all cocaine abusers, even in those with very severe levels of abuse, which is likely to reflect intersubject diversity (genetic, developmental, environmental), that leads to differences in cerebrovascular responses to cocaine. Moreover, one could argue that an animal model that has greater sensitivity to cocaine's adverse cerebrovascular effects offers a tool with which to investigate the development and recovery of cocaine induced TIA. Nonetheless, as for other conditions for which animal models are used to study diseases these have to be recognized as tools that help us control and measure processes that are not possible to do in humans, but that don't always have a direct one to one correspondence to human diseases. For our study we chose a daily cocaine dose of 35 mg/kg (i.p.) since this dose results in cocaine plasma levels consistent to those that have been reported in cocaine abusers [120] but since in our study we did not measure cocaine levels in plasma nor its metabolites this limits our ability to determine the representativeness of the cocaine levels in our mice to those seen clinically. Also the failure to measure cocaine and its metabolites in plasma precluded us to assess if these changed with chronic exposure and whether they related to the observed recovery. Note however that at least for 7 days exposure rodent studies showed that cocaine plasma concentrations did not change between acute and chronic cocaine exposures (7 days 20mg/kg i.p.)[120]. Finally, a limitation for our studies was that the imaging was conducted under anesthesia (isoflurane), which might have influenced the reactivity of blood vessels to cocaine. We selected isoflurane anesthesia to minimize these potential confounding effects, for it does not alter PCO2 (e.g., arterial carbon dioxide tension) nor PO2 (e.g., coronary sinus oxygen tension) [149].

In summary here we show that chronic cocaine decreased CBF and sensitized vessels to cocaine induced vasoconstriction such that with an acute cocaine injection this triggered an abrupt reduction in flow and ischemia resulting in a TIA manifested as contralateral paralyses. We also show that vasoconstriction and ischemia triggered by cocaine were associated with vascular reorganization and angiogenesis that we hypothesize prevented further deterioration of TIA despite continuous cocaine administration. Strategies to accelerate vascular recovery might be beneficial to improve clinical outcomes in cocaine abusers.

7. Quantitative imaging of rodent hemodynamic response to brain functional stimulation

The complex relation between neuronal activity and functional hyperemia ensures the blood flow supply meets the metabolic demands of neuron and glia activity[150, 151]. It serves as the fundamental basis for current imaging technologies to study brain functional response and thus becomes a vital research topic in neuroscience community [152-154]. However, we still do not fully understand of the local regulation of cerebral blood flow (CBF) and metabolism during neuron activity. Two main hypotheses have been proposed: "Metabolic hypothesis" and "Neurogenic hypothesis" [155]. The former claims the elevation of blood flow is the result of the increasing demands of glucose, oxygen and other nutrients during functional activity while the latter believes it is neuronal activity that directly regulates vasodilation/vasoconstriction through neurotransmitters or neuropeptide molecules. To tackle the complex relation between oxygenation, neuronal activity and CBF change, there is a keen demand for a versatile imaging tool capable of measuring vascular, hemodynamic metabolic, and neuronal parameters in deep tissue with high spatiotemporal resolution and sensitivity. The limitations of macroscopic (e.g. PET, MRI [156]) and microscopic (e.g. two/multi photon microscope[157]) imaging modalities prevent them from being the ideal tools for studying neurovascular coupling due to either limited resolution or insufficient FOV that fails to cover large vascular network and considerable population of neurons.

Multi-modality imaging system shed a light on neurovascular coupling by combining the advantages of several optical modalities which meets the demands for both high spatiotemporal resolution, deep penetration depth and large field of view and thus becomes a promising tool for studying neurovascular coupling. Zhijia Y. et. al. proposed a multimodal system that monitored multiple parameters during neurovascular uncoupling events including cerebral blood flow, blood volume, hemoglobin oxygenation, Ca^{2+} signaling thus allowing us to distinguish the hemodynamic change in vessel versus that in cells [18]. Besides the combination of OCT and optical intrinsic signal imaging (OISI), Mohammad A. Y. et. al. introduced 2-photon and confocal microscopy to provide angiography with micron level resolution, absolute pO_2 and NADH auto-fluorescence[19]. In our system, we combined μODT, OISI, laser speckle contrast imaging (LSCI) and GFP fluorescence imaging to characterize the cerebral hemodynamics and neuronal activity during the brain functional response to electric stimulation.

In this Chapter, we first demonstrated a new scanning scheme for functional stimulation study. Then we explicitly introduced the optical path design of the new multimodal microscopic system. Different from the previous μODT in which the scanning rate is limited by the detectable sensitivity for capillaries[103], the new system circumvents this limitation by implementing C-mode phase subtraction. Optical ray-tracing simulation was conducted for both OCT near infrared optical path and fluorescence visible optical path to characterize the system's parameters.

1. Methods:
    1.1. Animal preparation

C57 mice (male, 4 weeks, N=4 total) was initially anesthetized with 2.5% isoflurane and a cranial window was created over the left sensorimotor cortex. A small hole was created in the skull over the hind paw (HP) cortical area using a dental drill (XL-30w, OSADA Electric), and 0.3 μl of

GCaMP6f virus (AAV1.Syn.GCaMP6f.WPRE.SV40, Penn Vector Core) was slowly injected into the HP cortex (AP -0.7 mm, ML 1.5 mm) for neuronal uptake. After the injection, animals were monitored daily to ensure that they remained healthy.

During the experiment, Dexmedetomidine (1mg/kg) was then injected intraperitoneally and at the meantime, isoflurane was reduced to minimized dose (e.g. 1.0%). Animal's physiological states are continuously monitored, including electrocardiography (ECG), respiration rate, body temperature (Module 224002, Small Animal Instruments). All the procedures were in accordance with the National Institutes of Health Guide for the Care and Use of Laboratory Animals and were approved by the Institutional Animal Care and Use Committees of Stony Brook University.

1.2. Electric stimulation

To implement electric stimulation, two needle electrodes connected to an electrical stimulator (A-M System 2100, Sequim, WA, USA) were inserted under the skin of contralateral hind paw. After 10s delay, each hindpaw stimulation epoch lasted for 10 s during which bipolar rectangular electrical pulses (0.3 ms pulse width, 3-5 mA peak-to-peak amplitude) were delivered at 3-5Hz.

1.3. µODT's scanning scheme for functional study

Figure 7-1 demonstrates the schematic of 4D image acquisition in response to hind paw stimulation. The white dashed box in Figure 7-1a) represents the sub-ROI of a full field image (1.5×1.5mm^2) for stimulation recording. Figure 7-1b) demonstrates the simulation configuration whose details have been stated in 7.1.2 and Figure 7-1c) describes the data acquisition and image mosaicking of 4D µODT data. In Figure 7-1c), 4D data is shown as 2D matrix of x-z cross-sectional B-scan represented by each square. The first stimulation session started with the time-course monitoring for 105s of B-scan in the first y position y_1. After the stimulation, 3-5min recovery time was given to the animal. Then, the motor stage (Newport) with high precision transited the animal to the next y position (y_1) with incremental step of 4µm and the second stimulation session at y_2 started. 25 stimulation sessions were repeated to generate 4D images I(x,y,z,t) asynchronously. To obtain time-course functional response of 3D vascular network, 25 B-scans in different y positions but at the same time point (t_i) were stacked together yielding a 3D volume image at single time point $I(x,y,z)|_{t_i}$. After reconstruction, the asynchronous 4D images I(x,y,z,t) were converted to a time sequence of 3D volume image ($0.1 \times 0.5 \times 1.4$mm^2) with temporal resolution of 10Hz.
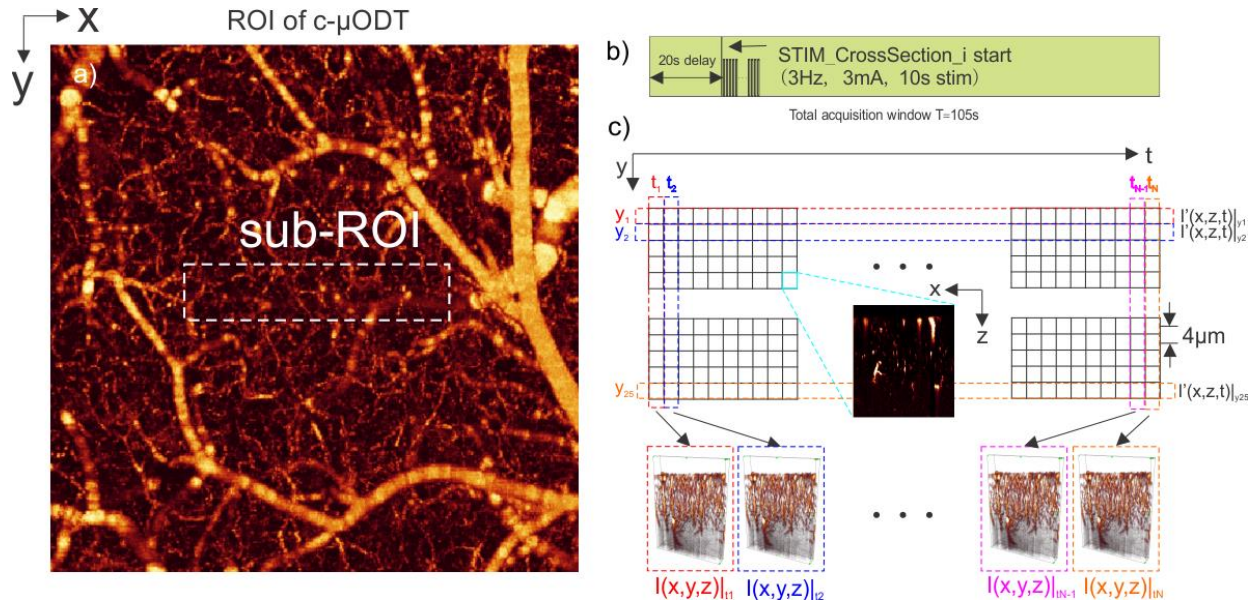
Figure 7-1 Stimulation scheme for c-µODT imaging of functional response to hind paw stimulation. a) Full field µODT image of mouse sensorimotor cortex ($1.5 \times 1.5 \text{mm}^2$) in which the write dashed box is the sub-ROI for stimulation study. b) Configuration of hindpaw electric stimulation (0.3 ms pulse width, 3 mA peak-to-peak amplitude, Delay: 20s, Duration:10s). Total data acquisition time: 105s. c) 4D image of functional response. 2D matrix of x-z cross-sectional B-scan. Time-course response of 3D capillary network I(x,y,z,t) can be obtain by restacking data.

1.4. Analysis of capillary response to electric stimulation

Heterogeneous neurological and physiological of multi-layer cortical layers result in various functional hyperemia response during functional stimulation in terms of response amplitude, delay latency, time to peak. Figure 7-2 shows the analysis of brain functional response of different cortical layers. Figure 7-2a) plots the functional responses of all capillaries captured in ROI (%) which can be replotted as a 2D depth-resolved map by sorting capillary response curves according to their depth location. Figure 7-2c) shows the averaged response of each cortical layer. Both Figure 7-2b) and c) demonstrate earlier onset time and greater response amplitude of L4 compared to other cortical layers. To quantitatively characterize the response features, each response curve was normalized and fitted by a skew Gaussian distribution $f(t)$:

$$f(t) = \frac{2}{\omega} \frac{1}{\sqrt{2\pi}} e^{-\left(\frac{t-\xi}{\omega}\right)^2} \cdot \frac{1}{2}\left[1 + erf\left(\alpha \frac{t-\xi}{\sqrt{2}\omega}\right)\right] \qquad \text{Eq.7-1}$$

Where α, ξ, ω denotes shape, location and scale of the skew normal distribution. Erf is the error function. Skewness of the functional response progressively increases from L1 0.59±0.11 to L5 0.76±0.06 characterizing the response's curve's change. In Figure 7-2e), L4 demonstrates the earliest time-to-peak period (9.65±2.97s) approximately 0.85s faster than L1 whose time-to peak period is 10.50±7.81s. Additionally, L4 shows the most intense response whose amplitude reaches 24.37±2.15% suggesting that L4 not only responses faster than other layers due to its direct correlation with TC but also demonstrates the largest response amplitude.
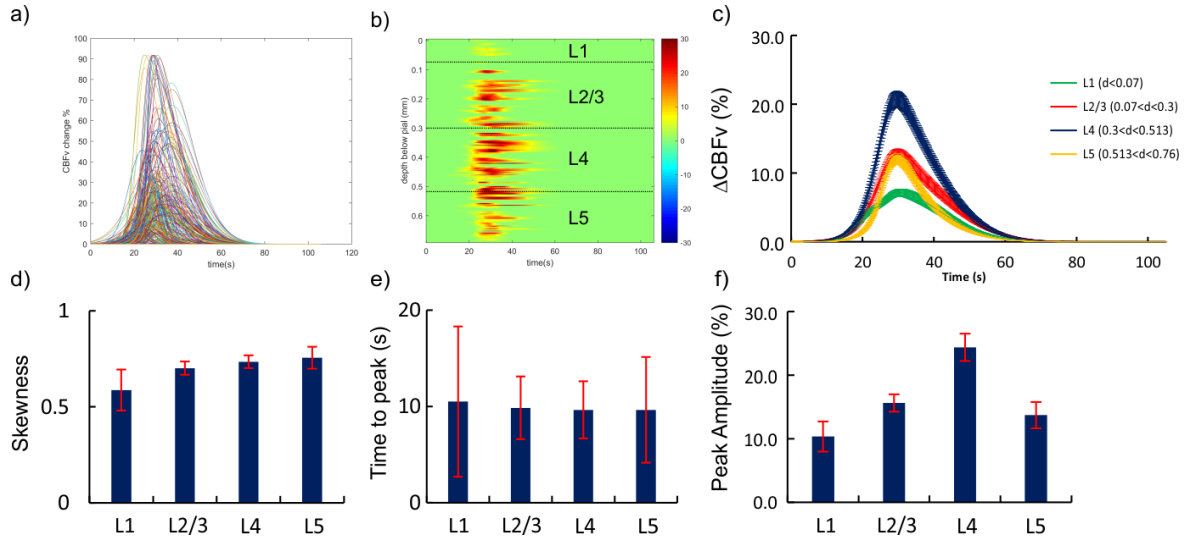
Figure 7-2 Analysis of capillay response in different cortical layers. a) Time-course reponse curve of all capillaries. b) Depth-resolved functional map . c) Averaged time-course respnose curve of different cortical layers. d-f) skewness, time-to-peak period and peak amplitude of different cortical layers. L1: d<70µm, L2/3: 70µm <d<300µm, L4: 300µm <d<513µm, L5: 513µm <d<760µm.

1.5. Nikon Eclipse FN1based microscopic multi-modality system

The custom multi-modality system was developed based on a Nikon Eclipse FN1 microscope consisting of a laser scanning ultrahigh-resolution optical coherence tomography (µOCT) and a GFP fluorescence and optical intrinsic signal imaging (OISI) system. Figure 7-3 shows the system setup. Both near infrared (NIR) and visible light (VIS) path used infinity optical system in which a short pass dichroic mirror (Thorlab 950nm short pass) split the merged signal allowing OCT signal in NIR band is received by the laser scanning system and fluorescence/OISI signal in VIS band is captured by camera.

In µOCT system, an ultra-broadband light source (Thorlab LSC2000C, λ_0=1310nm, $\Delta\lambda_{FWHM}$ =220nm) was used to illuminate a spectral-domain OCT engine determining the system coherence L_c=2(ln2)/π·λ_0^2/$\Delta\lambda_{cs}$ approximately 2.8µm in brain tisuse. In the sample arm, the Guassian beam was collimated by an achromatic collimator (f=10mm) with central wavelength of 1300nm which can yield a beam size of D=2f·NA_{eff}=1.8mm. After being expanded by 4 times by the tube lens (EFL_{tube}/EFL_{scan}=200mm/50mm=4), the expanded beam size of ϕ7.2mm well matches Olympus LMPLN5XIR whose entrance pupil is 2f·NA_{obj}=7.2mm. The collimated beam was transversely scanned by a pair of x/y scanning mirror consisting of a galvo scanner (Cambridge Technology 6215H) and a 4kHz resonance scanner (Cambridge Technology CRS4K). The collimated beam was focused onto the intermediate plane by an f50mm scan lens (Thorlab, SL50-2P2) and then entered infinity space through a Nikon tube lens (f/200mm). The light was focused onto the animal's sub-cortical layers for microvascular network imaging and the light backscattered from the mouse cortex was coherenced with the light reflected from the reference mirror. The coherence signal emitted from the detection fiber port which connected to a custom high-resolution spectrometer (Wasatch Photonics spectrometer). The interference fringes spectrally encoding the depth profile were detected by a high-speed line scan InGaAs camera (2048-pixels, 147k-lines/s;

GL2048, Sensors Unlimited) synchronized with sequential transverse scans for 2D/3D μOCT acquisition. In the reference arm, the light emitting from the reference arm collimator (f=10mm) and propergated through prism pair first then passed through scan lens, tube lens and objecitve sequentially in order to compensate the dispersion in the sample arm.

In the camera system, a custom illumination module consisting of multi-wavelength LED light guide (480nm, 532nm, 628nm, 830nm) was coupled into an annular ring illuminator to provide time-sharing sequential illumination onto the cortical window (>ϕ5mm). After passing through the 950nm short pass dichroic mirror, the VIS signal was filtered by a GFP dichroic mirror with cut-off wavelength at 495nm (T495lpxr, Chroma) which blocked the excitation light at 480nm and enabled fluorescence imaging (532nm), OISI (532nm, 628nm) and LSCI (830nm) which were recorded by a sCMOS camera (Andor Zylor 4.2 PLUS).
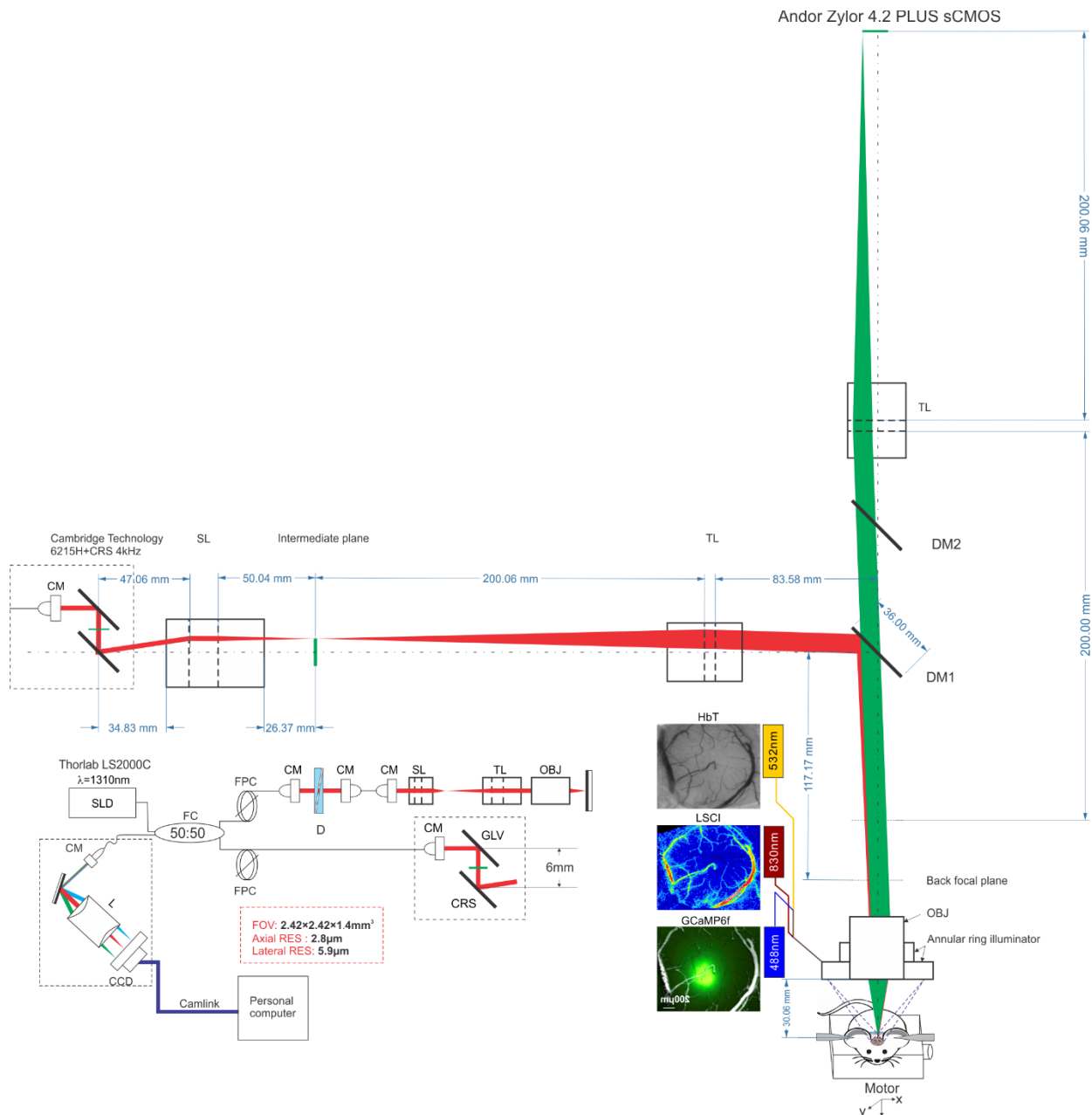
Figure 7-3 Schematic of multi-modality system that combines μOCT system (1310nm), LSCI (830nm), OISI (532nm and 628nm) and fluorescence imaging (ex:480nm em:532nm). The inset is the μOCT system integrated into the microscope. SLD: super luminance diode laser, FC: fiber couple (50:50), FPC: Fiber polarization controller, CM: fiber collimator; SL: scan lens, TL: tube lens, OBJ: objective, GLV: galvo scanner, CRS: 4kHz resonance scanner, LG: lens group. DM1: a dichroic mirror cutoff=950nm (short pass). DM2: GFP dichroic mirror cutoff: 495nm (long pass).

1.6. Selection of objective

To simultaneously record OCT, OISI, LSCI and GCamp6f fluorescence imaging, VIS light ranging from 480 to 700nm (e.g. GCaMP6[158], OISI) and NIR/IR light ranging from 800nm to 1400nm (e.g. OCT and LSCI) must share one objective. Therefore, the ideal objective needs to fulfill the following requirements: 1. Moderate NA ranging from 0.1 to 0.3 which ensures the sufficient depth of field (DOF=$0.565\lambda/\sin^2(\sin^{-1}(NA)/2)$)and high capillary resolution ($0.61\lambda/(n\cdot NA)$). 2. High transmission rate for both VIS and NIR/IR bands. 3. Chromatic aberration corrected for VIS and NIR/IR bands. Table 7-1 lists the specifics of 7 objectives including objective magnification (Mag), effective focal length (EFL), numerical aperture (NA), working distance (WD), entrance pupil diameter (EP), depth of field (DOF) and lateral resolution (RES).

Table 7-1 Specifics of candidate objectives

#	Candidate Objective	Mag	Mag (Nikon TL)	EFL[a]	NA	WD	EP[b]	DOF[c]	RES[d]
1	Nikon LU Plan Fluor 5X/0.15NA	5x	5x	40mm	0.15	23.5mm	12mm	43.62μm/176.63μm	1.60μm/ 3.94μm
2	Nikon TU Plan Fluor 10x/0.3NA	10x	10x	20mm	0.3	17mm	12mm	10.91μm/43.39μm	0.80μm/ 1.97μm
3	Nikon lambda 5x/0.2NA	5x	5x	40mm	0.2	20mm	16mm	26.73μm/98.91μm	1.20μm /2.96μm
4	Nikon Plan Fluor 4x/0.13NA	4x	5x	50mm	0.13	17.1mm	13mm	59.37μm/235.49μm	1.85μm /4.55μm
5	Olympus LMPLN10XIR	10x	11.11x	18mm	0.3	18mm	10.8mm	10.91μm/43.39μm	0.80μm/ 1.97μm
6	Olympus LMPLN5XIR	5x	5.56x	36mm	0.1	23mm	7.2mm	89.37μm/398.68μm	2.42μm/ 5.92μm
7	Thorlab LSM03	5x	5.56x	36mm	0.05	25.1mm	4.0mm	263.89μm/1598μm	4.81μm/ 11.84μm

a)   Objective EFL=Tube lens EFL/Magnification. Tube lens EFL varies from different microscope manufactures. Nikon EFL_{Tube}=200mm, Olympus EFL_{Tube}=180mm.
b)   EP=$2f\cdot NA$. f is the effect focal length of the objective.
c) $DOF_{532nm}=\lambda n/NA^2+n/(M\cdot NA)\cdot e$, e is the spacing of pixels (6.5μm), M is the lateral magnification.
     $DOF_{1310nm}=0.565\lambda/\sin^2(\sin^{-1}(NA)/2)$
     DOF_{532nm}/DOF_{1310nm}
d)   Res=$0.61\lambda/(n\cdot NA)$, Res_{532nm}/Res_{1310nm}

Figure 7-4 demonstrates the schematics of system setup for measuring objective transmission at 1310nm. 50:50 fiber coupler was illuminated by the OCT light source (Thorlab LS2000C, λ=1310nm). Port 3 was not wired and Port 4 was connected to collimator yielding the collimated beam (ϕ=4.75mm) which passed through the objective and reflected by a static mirror. After

suffering double-path transmission loss, the reflected signal was finally collected by an optical power meter (PM100D, Thorlab) connected to Port 2. By comparing measured power to the theoretical power at Port 2, we can evaluate the transmission loss of different objectives.
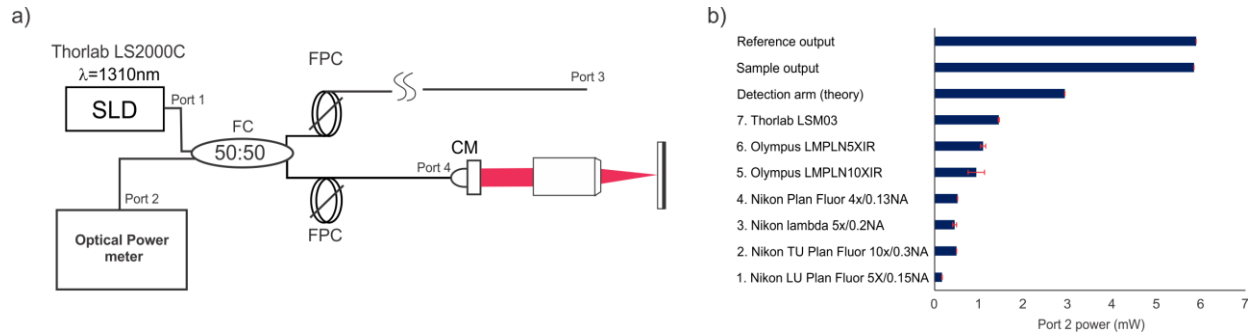
Figure 7-4 a) Schematics of system setup for measuring objectives' transmission loss b) Measured power of different objectives at Port 2 compared to the theoretical power.

Firstly, the theoretical power at Port 2 was estimated by directly measuring the out power at Port 3 and Port 4. Both Port 3 and Port 4 reached the output power of approximately 5.8mW approximately 50% of the laser output 11.8mW. Thus, the theoretical power of Port 2 should be 2.9mW about 50% of Port 4 output power. Then, the transmission loss of different objectives were evaluated at Port 2. For each objective, the measurement was repeatedly conducted on 3 different day experiments to rule out the measurement error induced by imperfect optical alignment. The averaged power (n=3) was used for comparison. The highest measured power was given by Thorlab LSM03 reaching 1.44±0.01mW (n=3) followed by Olympus LMPLN5XIR (1.02±0.06mW, n=3) and Olympus LMPLN10XIR (0.94±0.18mW, n=3). The best Nikon objective (Nikon Plan Fluor 4x/0.13) can only provide 0.51±0.002mW whose performance was approximately 50% of Olympus objective.

Although Thorlab LSM03 provides the best transmission rate at 1310nm, it is only optimized for NIR/IR band (λ=1310nm). To evaluate objectives' performance at VIS spectral band, we compared SNR of GFP fluorescence images acquired with different objectives. Figure 7-5 shows the comparison of 3 different objectives: Nikon Plan Fluor 4x, Olympus LMPLN5XIR and Thorlab LSM03. Figure 7-5d shows the intensity plots of a single neuron cell based on which SNR was measured. Both Nikon plan fluor 4x (Figure 7-5a') and Olympus LMPLN5XIR (Figure 7-5b') provide clear images and comparable SNR (SNR$_{Nikon}$=8.46dB, SNR$_{Olympus}$=8.08dB,). On the contrary, the image by Thorlab LSM03 is blurring with low SNR=6.765dB due to the aberration suggesting that Thorlab objective is only designed for NIR/IR band and not suitable for the multi-modality system.

In conclusion, considering both NIR/IR transmission loss and aberration in VIS band, Olympus LMPLN5XIR provided balanced performance and is suitable for the multi-modality system.
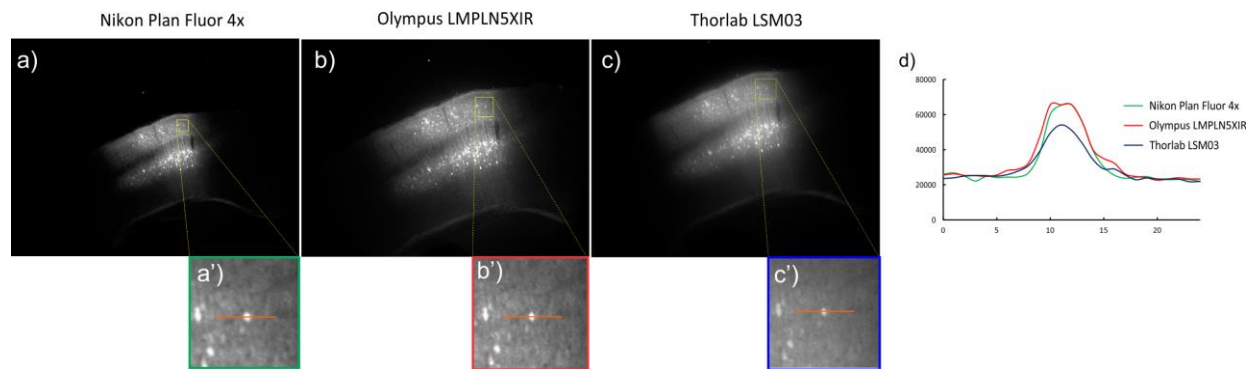
Figure 7-5 Comparison of GFP fluorescence image acquired with different objectives. a) Nikon Plan Fluor 4x b) Olympus LMPLN5XIR c) Thorlab LSM03 a'-c') are corresponding zoom-in images. d) Intensity profile of single neuron cell acquired by 3 objectives (oranges line in a'-c').

1.7. C-mode µODT by resonant scan

The coupling of A-scan rate and minimum detectable flow prevents the high speed monitoring functional response. Although the temporal resolution for slow flow can be improved by optical contrast agent (about 4 times)[103], A-scan rate of µODT is still insufficient, especially for large 3D cerebral vascular networks. To improve the imaging speed, we propose a new scanning strategy known as C-mode µODT which utilizes one galvo scanner (Cambridge Technology 6215H) and one 4kHz resonant scanner. Different from the conventional phase subtraction method in which phase shift was calculated between adjacent A-scans, C-mode µODT calculated phase shift between two adjacent B-scans whose time interval is determined by the resonant frequency of the resonance scanner. Figure 7-6 demonstrates the four views of the scan head. The sub-image (view A-A) in Figure 7-6a) and Figure 7-6b) show the tilting angle respect to z axis of resonant scanner and galvo scanner are 45° and 37.5° respectively. Additionally, two scanners' pivots separation is 0.295in (7.493mm) (Figure 7-6b)).
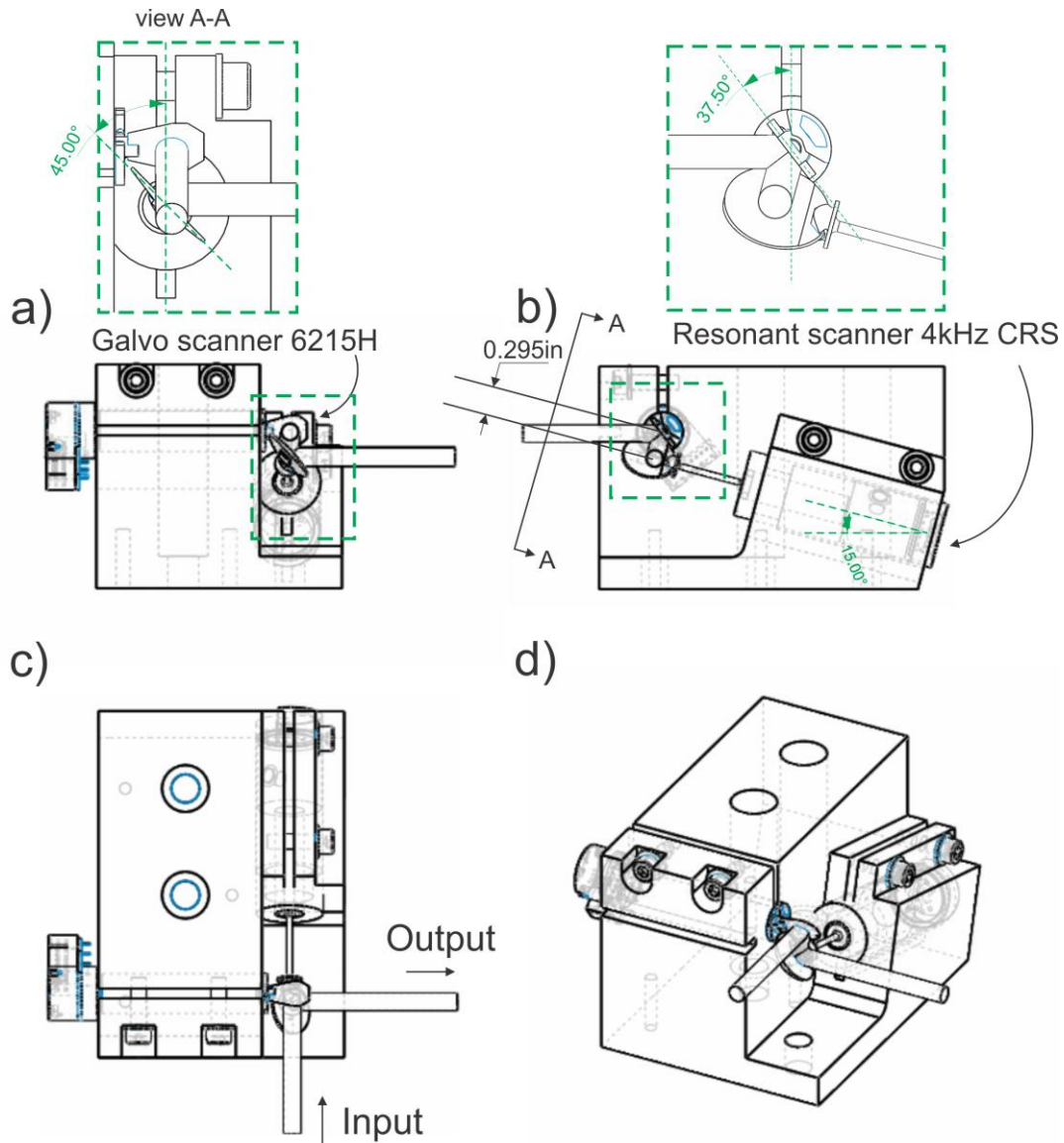
Figure 7-6 Four views of c-mode μODT's scan head. a) Front view. Sub-image (view A-A) shows the resonant scanner's tilting angle is 45° b) Right view. Scanner's pivots separation is 0.295inch. The inset shows the galvo scanner's tilting angle is 37.5°. c) Top view. The arrow shows the input and output beam d) Trimetric view.

C-mode μODT system consists of 3 scanning freedoms including galvo scanner (GLV) for y axis scan, 4kHz resonant scanner (CRS) x axis scan and linear transition stage for x scan which are all precisely synchronized by a custom GUI software. Figure 7-7 shows the synchronization of CRS in x direction (CRS_X_{obj}) and ramping scan by GLV in y direction (GLV_Y_{obj}). At the beginning of the scanning thread, an initial signal (Figure 7-7a) was generated by the GUI software to trigger 1) A TTL pulse train (120kHz) for triggering camera 2) CRS DC command (0-5V) to drive the CRS. Then GLV was controlled by analog voltage output directly triggered by CRS which was generated at each alteration of scanning direction (8kHz/2=4kHz). After CRS finishes one sinusoidal scan cycle (forward and backward scan) as it is highlighted by a dashed blue box of Figure 7-7b), GLV incremented by one step size Δy:

$$\Delta y = \frac{Y_{Obj}}{\text{Sampling Point \#}} \qquad\qquad \text{Eq.7-2}$$

Where Y_{Obj} is the scanning range in y direction and the number of sampling point is 8000. Thus $\Delta y=2.4/8000=0.3\mu m$ which is about 20 times smaller than its diffraction limitation $d=0.61\lambda/NA=0.61\times1.31\mu m/(0.1\times1.35)=5.92\mu m$ providing sufficient oversampling and thus can dramatically reduce its phase noise. Figure 7-7c) is the zoom-out curve of Figure 7-7b) showing the time-course sinusoidal scanning pattern of CRS and ramp scan pattern of GLV which can generate a single stripe scan in object plane shown in Figure 7-7d). To reconstruct the flow information, the aforementioned phase subtraction method (PSM) (Eq. 1-26) was used. However, different from the conventional PSM in which phase shift is calculated between two A-scans, phase shift in C-mode µODT is calculated between adjacent B-scans:

$$\Delta\phi = \arctan\left\{ \frac{\sum_{j=1}^{J}\left[Im(A_{t+\Delta T,z})Re(A_{t,z}) - Im(A_{j,z})Re(A_{t+\Delta T,z})\right]}{\sum_{j=1}^{J}\left[Re(A_{t+\Delta T,z})Re(A_{j,z}) - Im(A_{t,z})Im(A_{t+\Delta T,z})\right]} \right\} \qquad \text{Eq.7-3}$$

Where ΔT represents the time duration between either two forward B-scans or two backward B-scans. $A_{t,z}$ denotes the analytical OCT signal.
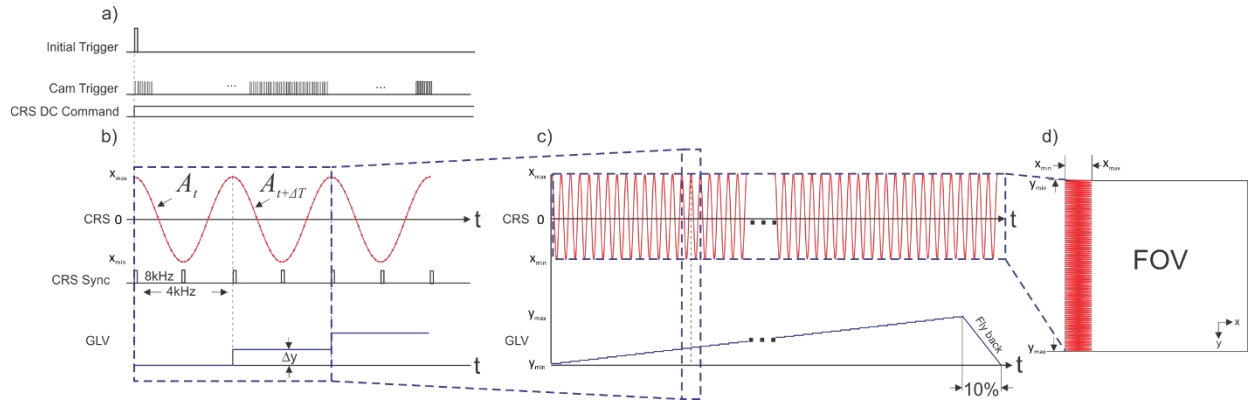
Figure 7-7 Triggering/scanning strategy of C-mode µODT. a) Initialization signal for single stripe scan that triggers the pulse train for camera (120kHz) and CRS DC command. b) Sinusoidal scan by CRS yields a synchronizing signal (8kHz) at each time it alters the scanning direction. GLV increments Δy when CRS completes a full cycle scan (4kHz). c) Zoom-out scanning pattern of b) showing the CRS's sinusoidal scan and GLV's ramping scan. d) En-face view of single stripe scanning pattern of C-mode µODT. CRS: Resonant scanner. GLV: Galvo scanner.

To ensure the µOCT ($X_{Obj}\times Y_{Obj}$ mm^2) covers the same FOV of fluorescence/OISI image acquired by the camera, the laser scanning system needs to generate an intermediate image plane whose size is the same as camera sensor size. Since Andor Zyla 4.2 PLUS sCMOS has a sensor chip as large as 13.3×13.3mm^2, the scanning range on the intermediate plane equals to ±6.65mm corresponding to optical scanning angle $\theta_{op\_X}=\arcsin(\pm6.65mm/50mm)=\pm7.64°$ or mechanical angle $\theta_{mch\_X}= \theta_{op\_X}/2=\pm3.82°$. However, the current camera technology is not fast enough to capture a B-scan of 2.4mm at frame rate of 8kHz. Because it requires a camera frame rate at least

$$f = 4\text{kHz} \times 2 \times \frac{GLV\_X_{obj}}{\text{Diffraction limitation}} = 8\text{kHz} \times \frac{GLV\_X_{intm} / \text{Maginifcation}}{0.61\lambda/\text{NA}} \qquad \text{Eq.7-4}$$

$$= 8\text{kHz} \times \frac{13.3mm / 5.5}{0.61 \times 1.31\mu m / (0.1 \times 1.35)} = 3.27\text{MHz} \gg 147\text{kHz (our camera)}$$

*Where 4kHz is the round-trip scanning frequency of resonant scanner consisting a forward and a backward scan. To calculate the frequency of single-trip, a factor of 2 is multiplied.

To solve this problem, we reduced the scanning range of resonant scanner in x direction and ensured CRS's mechanical scanning angle lied within operational range ($\geq 1°$). Thus, we set $\theta_{mch}\_X = \pm 1°$ and $\theta_{op}\_X = \pm 2°$ corresponding to scanning range on the intermediate plane $CRS\_X_{intm} = \sin(\pm 2°) \times 50\text{mm} = \pm 1.75\text{mm}$ and on the object plane $CRS\_X_{obj} = CRS\_X_{intm}/5.5 = \pm 317\mu m$.

Figure 7-8 shows Zemax simulation with multiple configuration (Table 7-2) to demonstrate the "stripe" scanning pattern. Figure 7-8 a)-d) are four views of the scanning system in which clear aperture of GLV and CRS are 5mm and 12.7mm, respectively. The input collimated beam (ϕ1.8mm) was reflected by GLV and CRS sequentially then focused onto the intermediate plane by the scan lens Figure 7-8d). A summary of scanning parameters of GLV, CRS and motor stage is listed in Table 7-4.

<p align="center">Table 7-2 Multi-configuration of scanning system (mechanical angle)</p>

	GLV	CRS
Cong #1	-3.82°	-1°
Cong #2	-3.82°	0
Cong #3	-3.82°	+1°
Cong #4	0	-1°
Cong #5	0	0
Cong #6	0	+1°
Cong #7	+3.82°	-1°
Cong #8	+3.82°	0
Cong #9	+3.82°	+1°
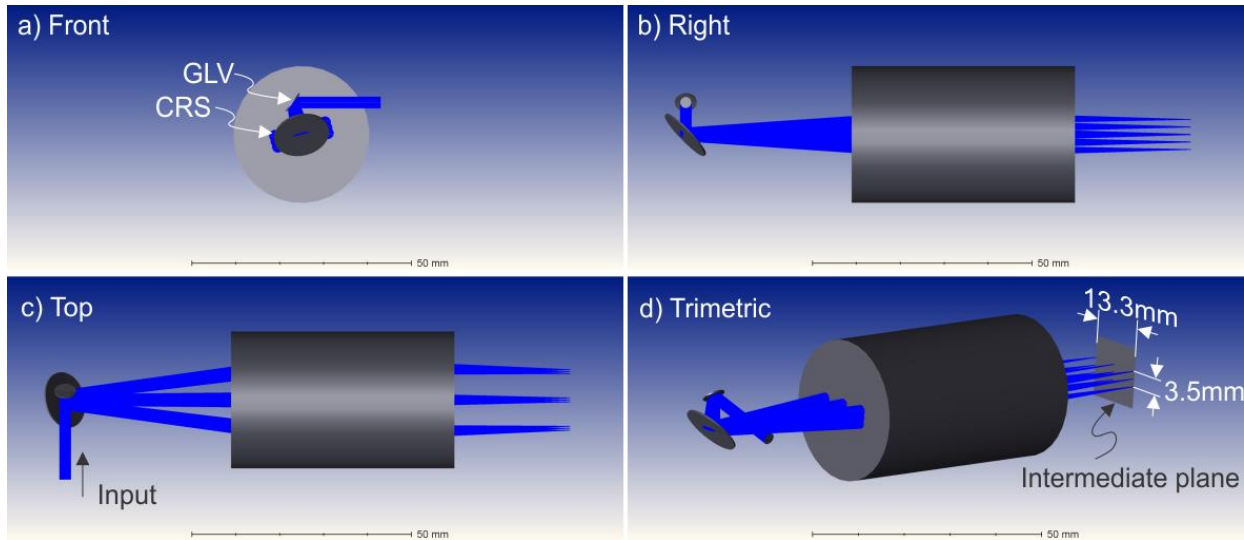
Figure 7-8 Four views of scanning system in Zemax. a) Front view b) Right view c) Top view d) Trimetric view.

Although the scanning range by CRS is dramatically reduced to ±317µm, our camera is still not fast enough (147kHz<<856kHz) to provide sufficient sampling points leaving huge gap (Figure 7-9a) between the acquisition points. To solve this problem, the second resonant pattern was scanned (Figure 7-9a orange curve) with incremental step of diffraction limitation (Δδ) in X direction by the motor stage (Figure 7-9b). Each sample point of the second scan pattern (orange line, Figure 7-9b) is displaced from its corresponding sample point of the previous "stripe" (red curve, Figure 7-9b) by a step size Δδ. We repeated this procedure until the accumulation of motor stage displacement in X direction covers the largest gap (Δx_{max}) between two sampling points (Figure 7-9b, green). Thus, the separation between adjacent sample points can be expressed as:

$$\Delta x = X\left[\cos(\frac{t}{T}2\pi) - \cos(\frac{t+\Delta t}{T}2\pi)\right]$$

Eq.7-5

Where X denotes the scanning range in x direction X=|±317|=317µm. Δt is the time duration between two sampling points ($\Delta t = 1/f_{exp} = 1/120kHZ$). T is the time duration for one scanning cycle (T=1/4kHz). Due to the nonlinearity of resonant scan, Δx varies as function of time.
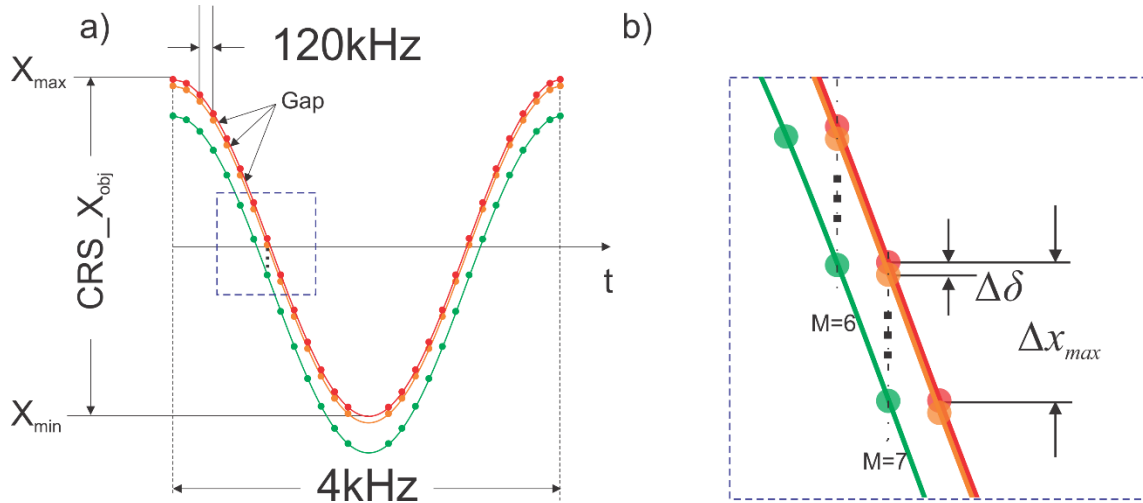
Figure 7-9 Repeated resonant scan with incremental step to fill up the large separation between adjacent sample points a) Repeated resonant scan within one cycle (red curve: 1st scan, orange curve:2nd scan with increments of $\Delta\delta$, green curve: last scan with increments of Δx_{max}). b) Zoom-in view of the blue dashed box in a). $\Delta\delta$: diffraction limitation.

To obtained the maximum separation Δx_{max}, we took the first order derivative of Δx and make it equal to zero:

$$\Delta x' = X\left[-\sin(\frac{2\pi}{T}t_m)\left[1-\cos\frac{2\pi}{T}\Delta t\right]+\cos(\frac{2\pi}{T}t_m)\sin(\frac{2\pi}{T}\Delta t)\right]=0 \qquad \text{Eq.7-6}$$

$$\tan\frac{2\pi}{T}t_m = \frac{\sin\dfrac{2\pi}{T}\Delta t}{1-\cos\dfrac{2\pi}{T}\Delta t} \qquad \text{Eq.7-7}$$

Where $t_m=0.2333T+N\cdot T/2$, N=0,1,2,3… denotes the time point yielding the maximum separation

$$\Delta x_{max} = 435\mu m\left[\cos(2\pi\cdot0.2333)-\cos(2\pi\cdot0.2333+2\pi\cdot1/30)\right]=66.21\mu m \qquad \text{Eq.7-8}$$

If the step size equals to the diffraction limitation $\Delta\delta=0.61\lambda/NA\approx6\mu m$, approximately 11 steps are required to complete the maximum motor transition Δx_{max}. Additionally, a general expression can calculate the number of incremental steps required (N) for each sampling point (M):

$$N = \frac{X\left[\cos(\dfrac{\Delta t\cdot M}{T}2\pi)-\cos(\dfrac{\Delta t\cdot(M+1)}{T}2\pi)\right]}{\Delta\delta} \qquad \text{Eq.7-9}$$

$$M=0,1,2….T/(2\Delta t)-1$$

*Where M is the point index. Since the x displacement is an even function, we only consider the first half cycle or forward scan and thus the maximum M equals to T/(2Δt)-1.

Table 7-3 Incremental steps required (N) for each sample point (M)

M	0	1	2	3	4	5	6	7	8	9	10	11	12	13	14
N	1.2	3.4	5.5	7.4	8.9	10.1	10.8	11.0	10.8	10.1	8.9	7.4	5.5	3.4	1.2

In summary, the multi-modality system completes the C-mode μODT scan by implementing 3 movement freedoms including a resonant scanner for x axis scan, a Galvo scanner for y axis scan and a motor stage for x axis transition which fills up the gaps due to the limited sampling number. Table 7-4 lists the summary of scanning configurations for these 3 movement freedoms.

Table 7-4 Summary of scanning configurations for full field imaging

	Galvo scanner	Resonant scanner	Motor stage
Scanning direction	Y	X	X
Scanning type	Ramping	Sinusoidal scan	Linear transition
Scanning frequency	0.5Hz (8000points)	4kHz	0.5Hz
Duty cycle	90% (ramping)	100% (sinusoidal)	NA
Mechanical Angle	±3.82°	±1°	NA
Optical Angle	±7.64°	±2°	NA
Scanning range on Intermediate plane	±6.65mm	±1.75mm	NA
Scanning range on object plane	±1.2mm	±0.32mm	Increments: 6μm
			Increment steps:11
			Total transition:66μm

2. Conclusions & Discussions

We developed a novel multi-modality optical imaging system that combines the advantages of ultrahigh-resolution optical Doppler tomography (μODT) for quantitatively imaging 3D microvascular flow and GCamp6f fluorescence for monitoring neuronal activity [159]. Additionally, we also developed a high-speed scanning strategy of μODT system for monitoring cerebral blood flow's response to hind paw functional stimulation.

Monitoring microvascular network dynamics during neuronal activity requires high temporal resolution due to either the neurons' and astrocytes' fast regulation of blood flow through directly controlling arteriole smooth muscle[160] or capillary regulation by pericytes[161]. Laser speckle contrast imaging (LSCI) provides decent temporal resolution for imaging the superficial vascular networks owning to the advances of high speed camera and spatiotemporal algorithm [162]. Additionally, ultra-fast fMRI with temporal resolution of 50ms shed light on the vascular response of different cortical layers[163] showing the onsite time difference of approximately 0.25s between L2/3 and L4 which suggests the minimum frame rate is at least 8fps to capture the heterogeneous response of different cortical layers. Our system provides the frame rate of 10fps which is sufficient to measure the onsite time and differentiate the onsite difference across cortical layers. Furthermore, optical contrast agent, intralipid, has been reported to enable

higher temporal resolution for dynamically tracking vascular responses to drug challenge[103]. Thus, higher temporal resolution (e.g. 20fps) can be achieved by implementing the imaging contrast agent.

In Figure 7-2, we demonstrated the method of quantitative analysis of function hyperemia in different cortical layers. It is noticeable that L4 had earlier to-peak time compared to other layers which can be explained as the synchronous neuronal activity in L4 layer because of the major thalamocortical input (TC) of L4 [164, 165]. Moreover, the depth-resolved optical imaging also reported the strongest function response occurred in L4 layers [166] which closely coincides with our results. The earliest onsite time should range from 0.5s to 0.67s after electrode stimulation according to previous researches [124, 166]. However, our results showed a slight raise even before the stimulation which might be the artifact of data interpolation. Higher temporal resolution is strongly encouraged to eliminate this artifact.

The depth of field (DOF) determined by the Rayleigh range couples with the system's lateral resolution. Instead of using Gaussian beam, Bessel beam has been demonstrated capable of improving the system's DOF, whilst preserving the transverse resolution [167-169]. It might be of great help in the multi-modality system since NIR and VIS have their own optical paths. Thus, decoupling the OCT's resolution from fluorescence imaging's resolution becomes feasible. However, the influence of Bessel beam in scattering biological tissue has been investigated [170] demonstrating the Gaussian beam in focus suffers less reduction of local contrast than does the Bessel beam. Therefore, careful consideration need to take since simply replacing the Gaussian beam with the Bessel bean may lead to the loss of signal-to-noise ratio (SNR).

One of the major limitations of this system is the limited camera speed leading to insufficient sampling points for C-mode μODT. Utilizing motor stage as the third movement freedom was only a compromised choice rather than an optimized design. Because the instability of A-scan trigger signal in each 'stripe scan' may lead to imperfect reconstruction of B-scans. Additionally, the nonlinearity of resonant scan causes distorted image which requires post-processing algorithms or modified clocking for compensation.

8. Conclusion and future work

Optical coherence tomography (OCT) has been becoming one of the most active and rapidly growing bio-optical imaging modalities since it was invented in early 1990s [13]. After more than 25 years of development, there are more than 20,000 publications in a wide range of clinical specialties as well as other applications with annual publication reaching approximately 3,500 [171]. Following active academic research, over $500M of venture capital poured into corporate R&D investment to develop OCT related products urging the exponential growth of OCT market worldwide. During the last decades, various OCT applications have been comprehensively studied, some of which have been successfully commercialized, for example, ophthalmic products (Zeiss Inc.), cardiovascular products (St. Jude Medical), demonology products (Michelson diagnostics) and gastroenterology products (Ninepoint Medical). Especially, OCT has become the standard-of-care in ophthalmology that allows for 3D imaging of retina.

There is no doubt that imaging 3D structure of biological tissue by OCT technology has been comprehensively studied in the past decades. Interestingly, functional imaging with OCT is now attracting tremendous attentions. As the core topic of the present dissertation, ultrahigh-resolution optical coherence Doppler tomography (μODT) demonstrates its great potential in neurology and oncology researches owing to its capillary resolution and large field of view (FOV)[103, 143, 172, 173].

In Chapter 1, the basic principle of OCT was reviewed mathematically showing that the fundamental image contrast of OCT is generated from temporal coherence between the static mirror in the reference arm and the multiple scatterers in the biological tissue sample. The axial resolution of OCT is directly determined by the coherence length of the light source which is inverse proportional to its spectral bandwidth. Then, the algorithm for quantifying blood flow velocity was introduced demonstrating the proportional relation between the flow velocity and the phase shift between adjacent A-scans.

Chapter 2-4 explicitly described the development of μODT as well as the hardware and software improvements. Specifically, Chapter 2 introduced the hardware configurations of the newly developed 1310nm μODT system which was powered by an ultra-broadband superluminance diode (SLD) yielding the axial resolution of 2.8μm in tissue. Additionally, the custom spectrometer provided sufficient imaging depth of 1.5mm with only 10dB SNR loss. Moreover, the data acquisition graphic user interface (GUI) was redesigned based on Qt platform. Integrated with GPU processing and circular buffer structure, data processing and acquisition speed was significantly increased. Most importantly, the new system enabled the penetration depth of 1.4mm, 4 times deeper than that of previous 800nm system allowing for monitoring the depth dependent vascular response to drug challenge. In Chapter 3, we introduced a novel optical contrast agent: intralipid, a FDA approved fat emulsion commonly used as nutrition supply for patients. We also demonstrated its dramatic enhancement for μODT images, especially for microvascular network imaging. The underestimated flow velocity of small capillary was explained as the result of the sparse distribution of red blood cells (RBCs) in capillary. By injecting the fat emulsion, small intralipid particles flew at the same velocity as RBCs yielding the same phase shift detected by μODT. Chapter 4 demonstrates the improvements of phase subtraction method (PSM) in which the dynamic range of PSM was improved by summing up the phase shifts of adjacent 3 A-scans and Doppler angle was detected by calculating the gradient for each point of the extracted vessel

skeleton. Additionally, Hessian matrix method was introduced to extract Doppler angle of arbitrary vessels by analyzing its eigenvalues and eigenvectors.

Chapter 5 and 6 demonstrated the pre-clinical applications of great translational implication using µOCT. In Chapter 5, we proposed a new approach to identify the tumor boundary. Different from the conventional approach relying on the scattering feature of necrotic tissue, the new method analyzed angiogenic vasculature in the tumor microenvironment which had superior sensitivity and specificity over other optical technologies. Chapter 6 correlated the dysfunction of cerebral vascular network with cocaine-induced transient ischemic attack (TIA). We found that the severely hypo-perfused left cortex due to cocaine elicited vasoconstriction was tightly coupled with the hemi-paralysis on the contralateral sides. Additionally, according to a longitudinal study, the angiogenesis triggered by the hypoxic cerebral environment relieved the symptom demonstrating the declined occurrence of paralysis after the same dose cocaine challenge.

Chapter 7 focused on the development of multi-modality system that combined µODT and fluorescence imaging in order to address those unanswered questions of neurovascular coupling. This chapter first introduced a high-speed scanning strategy for monitoring vascular function response allowing for quantitatively analyzing the differences of functional response across cortical layers in term of onset time, response peak amplitude and so on. Then, it also explicitly described the system setup-a modified Nikon FN1 microscope containing a laser scanning near infrared light path and a visible light path split. Furthermore, a new C-mode µODT scanning mode was introduced to unleash the camera's power for high-speed data acquisition.

Although great progresses have been made, there remain some challenges to be addressed in our future work.

1. Absolute velocity measurement.

Although the absolute velocity can be theoretically retrieved by $v = v_z / \cos\theta$, the corrected velocity at $\theta = 90°$ is usually impractically large due to either the background noise floor or the impact of finite objective NA which correlates the broadness of Doppler spectrum [33, 34]. Thus, a more precise model is required taking account both the background noise and objective NA. Additionally, hardware modifications may be required to retrieve the absolute flow velocity. For example, dual-beam or triple-beam illumination enables measuring axial velocity from various angles which is theoretically able to retrieve the absolute velocity [174, 175]. However, few groups able to present promising data which maps the absolute cerebral blood flow velocity of whole vascular network. More theoretical and experimental studies are required to find out the best approach to measuring absolute flow velocity.

2. Explore novel anti-angiogenic therapies using µOCT.

Chapter 5 demonstrated a new method for identifying tumor boundary which has great clinical implication. Some theoretical tumor model shows the decrease vessel density in the tumor center contradicting our results[176]. This suggests that the angiogenesis progression during tumor growth may vary depending on either tumor cell types or the environment. Nevertheless, both increased or declined vessel density can be used as the imaging contrast for identifying tumor boundary. The next step is to validate the new anti-angiogenic therapy using the present method.

For example, VEGFR-2 blockade has been reported to reduce total tumor volume, angiogenesis in term of declined fractal dimension.

3. Imaging cocaine-induced transient ischemic attack (TIA) in awake animals.

In Chapter 6, we demonstrated cocaine-induced TIA was closely correlated with the hypo-perfused cortex on its contralateral side. However, due to the limitation of current imaging system, the µODT images were acquired under anesthetized condition (Isoflurane 2.0%) which may affect CBFv or vasoconstriction response [177] right after cocaine challenge since Isoflurane is a vasodilator [178]. To address this limitation, there is a keen demand for a portable µODT system allowing for monitoring CBFv change of awake animal subjected to cocaine challenge. Additionally, real-time monitoring neuronal activity during TIA is also desirable if GCamp6f fluorescence imaging can be integrated into this portable device. Last but not least, simultaneously imaging both cortices help us to understand the side-preferred hypo-perfusion and cocaine incuded hemi-paralysis, however, requires a huge cranial window covering both cortices which still remains a great imaging and surgical challenge.

4. Explore new high-speed µODT.

It has been commonly acknowledged that the scanning speed of µODT using phase subtraction method (PSM) is limited. Specifically, its A-scan frequency (f) is limited by the fundamental mechanism of phase-resolved methods [16, 44] since the measured phase is coupled with the duration between A-scans ($T=1/f$). Its B-scan rate is limited by the requirement of oversampling A-scan number [45]. We believe dual-beam scanning strategy is a viable solution which circumvents the speed limitations for both A-scan frequency and B-frame rate. Specifically, a vessel is sequentially scanned by Beam1 and Beam2, the separation between which generates a time duration for accumulating the phase shift. Thus, the phase shift can be obtained by $\Delta\phi=\phi_{Beam2}|_{t2} - \phi_{Beam1}|_{t1}$. Using the dual-beam scanning strategy, the phase shift duration is decoupled from the scanner's speed since it is determined by $\Delta t=\Delta d/v_x$ where Δd is the distance separation between two beam foci and v_x is the lateral scanning speed. However, this is just a conceptual design and still requires huge amount of theoretical and experimental works.

References

1. H. Gohe, T.W., *Der Ultraschall in der Medizin.* Klinische Wochenschrift, 1940. **19**(2).
2. Brownell, W.H.S.G.L., *Localization of brain tumors with positron emitters.* Nucleonics, 1953. **11**: p. 40-45.
3. Oldendorf, W.H., *Isolated Flying Spot Detection of Radiodensity Dis-Continuities-Displaying the Internal Structural Pattern of a Complex Object.* Bio-Medical Electronics, IRE Transactions on, 1961. **8**(1): p. 68-72.
4. Damadian, R., *Tumor Detection by Nuclear Magnetic Resonance.* Science, 1971. **171**(3976): p. 1151-1153.
5. Ogawa, S., et al., *Brain magnetic resonance imaging with contrast dependent on blood oxygenation.* Proceedings of the National Academy of Sciences, 1990. **87**(24): p. 9868-9872.
6. Devor, A., et al., *Frontiers in optical imaging of cerebral blood flow and metabolism.* J Cereb Blood Flow Metab, 2012. **32**(7): p. 1259-76.
7. Kim, S.G. and S. Ogawa, *Biophysical and physiological origins of blood oxygenation level-dependent fMRI signals.* J Cereb Blood Flow Metab, 2012. **32**(7): p. 1188-206.
8. Schaffer, C.B., et al., *Two-Photon Imaging of Cortical Surface Microvessels Reveals a Robust Redistribution in Blood Flow after Vascular Occlusion.* PLoS Biol, 2006. **4**(2): p. e22.
9. Lecoq, J., et al., *Simultaneous two-photon imaging of oxygen and blood flow in deep cerebral vessels.* Nat Med, 2011. **17**(7): p. 893-898.
10. Shih, A.Y., et al., *Two-photon microscopy as a tool to study blood flow and neurovascular coupling in the rodent brain.* J Cereb Blood Flow Metab, 2012. **32**(7): p. 1277-1309.
11. Paulson, O.B., et al., *Cerebral blood flow response to functional activation.* J Cereb Blood Flow Metab, 2009. **30**(1): p. 2-14.
12. Yao, J., et al., *High-speed label-free functional photoacoustic microscopy of mouse brain in action.* Nat Meth, 2015. **12**(5): p. 407-410.
13. Huang, D., et al., *Optical coherence tomography.* Science, 1991. **254**(5035): p. 1178-1181.
14. Srinivasan, V.J. and H. Radhakrishnan, *Optical Coherence Tomography angiography reveals laminar microvascular hemodynamics in the rat somatosensory cortex during activation.* NeuroImage, 2014. **102, Part 2**(0): p. 393-406.
15. Ren, H., C. Du, and Y. Pan, *Cerebral blood flow imaged with ultrahigh-resolution optical coherence angiography and Doppler tomography.* Optics Letters, 2012. **37**(8): p. 1388-1390.
16. Zhao, Y., et al., *Phase-resolved optical coherence tomography and optical Doppler tomography for imaging blood flow in human skin with fast scanning speed and high velocity sensitivity.* Optics Letters, 2000. **25**(2): p. 114-116.
17. Mariampillai, A., et al., *Optimized speckle variance OCT imaging of microvasculature.* Optics Letters, 2010. **35**(8): p. 1257-1259.
18. Yuan, Z., et al., *Imaging separation of neuronal from vascular effects of cocaine on rat cortical brain in vivo.* NeuroImage, 2011. **54**(2): p. 1130-1139.
19. Yaseen, M.A., et al., *Multimodal optical imaging system for in vivo investigation of cerebral oxygen delivery and energy metabolism.* Biomedical Optics Express, 2015. **6**(12): p. 4994-5007.
20. Drexler, W., et al., *Optical coherence tomography today: speed, contrast, and multimodality.* Journal of Biomedical Optics, 2014. **19**(7): p. 071412-071412.
21. Yuichi, T., S. Masayuki, and K. Fumihiko, *Two-dimensional optical coherence tomography using spectral domain interferometry.* Journal of Optics A: Pure and Applied Optics, 2000. **2**(1): p. 21.
22. Chen, W., et al., *High-speed swept source optical coherence Doppler tomography for deep brain microvascular imaging.* Scientific Reports, 2016. **6**: p. 38786.
23. Choi, W., et al., *Phase-sensitive swept-source optical coherence tomography imaging of the human retina with a vertical cavity surface-emitting laser light source.* Optics Letters, 2013. **38**(3): p. 338-340.

24. Baumann, B., et al., *Total retinal blood flow measurement with ultrahigh speed swept source/Fourier domain OCT.* Biomedical Optics Express, 2011. **2**(6): p. 1539-1552.

25. Izatt, J.A. and M.A. Choma, *Theory of Optical Coherence Tomography*, in *Optical Coherence Tomography*, W. Drexler and J. Fujimoto, Editors. 2008, Springer Berlin Heidelberg. p. 47-72.

26. Goodman, J.W., *Statistical Optics.* 2000: Wiley-Interscience Publication.

27. Born, M.A.X. and E. Wolf, *CHAPTER VII - ELEMENTS OF THE THEORY OF INTERFERENCE AND INTERFEROMETERS*, in *Principles of Optics (SIXTH (CORRECTED) EDITION)*. 1980, Pergamon. p. 256-369.

28. Ren, H.-G., et al., *Cocaine-induced cortical microischemia in the rodent brain: clinical implications.* Mol Psychiatry, 2012. **17**(10): p. 1017-1025.

29. Yuan, Z., et al., *A digital frequency ramping method for enhancing doppler flow imaging in Fourier-domain optical coherence tomography.* Optics Express, 2009. **17**(5): p. 3951-3963.

30. Srinivasan, V.J., et al., *OCT methods for capillary velocimetry.* Biomedical Optics Express, 2012. **3**(3): p. 612-629.

31. Srinivasan, V.J., et al., *Optical coherence tomography for the quantitative study of cerebrovascular physiology.* J Cereb Blood Flow Metab, 2011. **31**(6): p. 1339-45.

32. Srinivasan, V.J., et al., *Quantitative cerebral blood flow with Optical Coherence Tomography.* Optics Express, 2010. **18**(3): p. 2477-2494.

33. Ren, H., et al., *Imaging and quantifying transverse flow velocity with the Doppler bandwidth in a phase-resolved functional optical coherence tomography.* Optics Letters, 2002. **27**(6): p. 409-411.

34. Piao, D., L.L. Otis, and Q. Zhu, *Doppler angle and flow velocity mapping by combined Doppler shift and Doppler bandwidth measurements in optical Dopplertomography.* Optics Letters, 2003. **28**(13): p. 1120-1122.

35. Proskurin, S.G., Y. He, and R.K. Wang, *Determination of flow velocity vector based on Doppler shift and spectrum broadening with optical coherence tomography.* Optics Letters, 2003. **28**(14): p. 1227-1229.

36. You, J., et al., *Volumetric Doppler angle correction for ultrahigh-resolution optical coherence Doppler tomography.* Applied Physics Letters, 2017. **110**(1): p. 011102.

37. You, J., et al., *Optical coherence Doppler tomography for quantitative cerebral blood flow imaging.* Biomedical Optics Express, 2014. **5**(9): p. 3217-3230.

38. Qi, L., et al., *Fully distributed absolute blood flow velocity measurement for middle cerebral arteries using Doppler optical coherence tomography.* Biomedical Optics Express, 2016. **7**(2): p. 601-615.

39. Chen, Z., et al., *Noninvasive imaging of in vivo blood flow velocity using optical Doppler tomography.* Optics Letters, 1997. **22**(14): p. 1119-1121.

40. van Leeuwen, T.G., et al., *High-flow-velocity and shear-rate imaging by use of color Doppler optical coherence tomography.* Optics Letters, 1999. **24**(22): p. 1584-1586.

41. Morofke, D., et al., *Wide dynamic range detection of bidirectional flow in Doppler optical coherence tomography using a two-dimensional Kasai estimator.* Optics Letters, 2007. **32**(3): p. 253-255.

42. Zhao, Y., et al., *Doppler standard deviation imaging for clinical monitoring of in vivo human skin blood flow.* Optics Letters, 2000. **25**(18): p. 1358-1360.

43. Liu, G. and Z. Chen, *Advances in Doppler OCT.* Chinese optics letters : COL / sponsored by the Chinese Optical Society, 2013. **11**(1): p. 011702.

44. Yang, V.X.D., et al., *Improved phase-resolved optical Doppler tomography using the Kasai velocity estimator and histogram segmentation.* Optics Communications, 2002. **208**(4–6): p. 209-214.

45. Hyle Park, B., et al., *Real-time fiber-based multi-functional spectral-domain optical coherence tomography at 1.3 μm.* Optics Express, 2005. **13**(11): p. 3931-3944.

46.   Yang, V., et al., *High speed, wide velocity dynamic range Doppler optical coherence tomography (Part I): System design, signal processing, and performance.* Optics Express, 2003. **11**(7): p. 794-809.

47.   Hendargo, H.C., et al., *Doppler velocity detection limitations in spectrometer-based versus swept-source optical coherence tomography.* Biomedical Optics Express, 2011. **2**(8): p. 2175-2188.

48.   !!! INVALID CITATION !!!

49.   Heshmat, S., S. Tomioka, and S. Nishiyama, *Reliable phase unwrapping algorithm based on rotational and direct compensators.* Applied Optics, 2011. **50**(33): p. 6225-6233.

50.   Tomioka, S. and S. Nishiyama, *Phase unwrapping for noisy phase map using localized compensator.* Applied Optics, 2012. **51**(21): p. 4984-4994.

51.   DeFelipe, J., L. Alonso-Nanclares, and J. Arellano, *Microstructure of the neocortex: Comparative aspects.* Journal of Neurocytology, 2002. **31**(3-5): p. 299-316.

52.   Kobat, D., N.G. Horton, and C. Xu, *In vivo two-photon microscopy to 1.6-mm depth in mouse cortex.* Journal of Biomedical Optics, 2011. **16**(10): p. 106014-106014-4.

53.   Wang, R.K., et al., *Three dimensional optical angiography.* Optics Express, 2007. **15**(7): p. 4083-4097.

54.   Lee, S.-W., et al., *Optimization for Axial Resolution, Depth Range, and Sensitivity of Spectral Domain Optical Coherence Tomography at 1.3 µm.* The journal of the Korean Physical Society, 2009. **55**(6): p. 2354-2360.

55.   Ha Usler, G. and M.W. Lindner, *"Coherence radar" and "spectral radar"-new tools for dermatological diagnosis.* J Biomed Opt, 1998. **3**(1): p. 21-31.

56.   Hagen-Eggert, M., P. Koch, and G. Hüttmann. *Analysis of the signal fall-off in spectral domain optical coherence tomography systems*. 2012.

57.   Yun, S., et al., *High-speed spectral-domain optical coherence tomography at 1.3 µm wavelength.* Optics Express, 2003. **11**(26): p. 3598-3604.

58.   Dorrer, C., et al., *Spectral resolution and sampling issues in Fourier-transform spectral interferometry.* Journal of the Optical Society of America B, 2000. **17**(10): p. 1795-1802.

59.   Hagen-Eggert, M., P. Koch, and G. Hüttmann. *Analysis of the signal fall-off in spectral domain optical coherence tomography systems*. in *SPIE BiOS*. 2012. SPIE.

60.   Potsaid, B., et al., *Ultrahigh speed 1050nm swept source/Fourier domain OCT retinal and anterior segment imaging at 100,000 to 400,000 axial scans per second.* Opt Express, 2010. **18**(19): p. 20029-48.

61.   Potsaid, B., et al., *Ultrahigh speed Spectral / Fourier domain OCT ophthalmic imaging at 70,000 to 312,500 axial scans per second.* Optics Express, 2008. **16**(19): p. 15149-15169.

62.   Sun, T. and R.F. Hevner, *Growth and folding of the mammalian cerebral cortex: from molecules to malformations.* Nat Rev Neurosci, 2014. **15**(4): p. 217-232.

63.   Cho, N.H., et al., *High Speed SD-OCT System Using GPU Accelerated Mode for in vivo Human Eye Imaging.* Journal of the Optical Society of Korea, 2013. **17**(1): p. 68-72.

64.   Sylwestrzak, M., et al., *Four-dimensional structural and Doppler optical coherence tomography imaging on graphics processing units.* J Biomed Opt, 2012. **17**(10): p. 100502.

65.   Iadecola, C., *Neurovascular regulation in the normal brain and in Alzheimer's disease.* Nat Rev Neurosci, 2004. **5**(5): p. 347-360.

66.   Logothetis, N.K., et al., *Neurophysiological investigation of the basis of the fMRI signal.* Nature, 2001. **412**(6843): p. 150-157.

67.   Bélanger, M., I. Allaman, and Pierre J. Magistretti, *Brain Energy Metabolism: Focus on Astrocyte-Neuron Metabolic Cooperation.* Cell Metabolism, 2011. **14**(6): p. 724-738.

68.   Turk-Browne, N.B., *Functional Interactions as Big Data in the Human Brain.* Science, 2013. **342**(6158): p. 580-584.

69.   Fox, M.D., et al., *Coherent spontaneous activity accounts for trial-to-trial variability in human evoked brain responses.* Nat Neurosci, 2006. **9**(1): p. 23-25.

70.   Fox, M.D. and M.E. Raichle, *Spontaneous fluctuations in brain activity observed with functional magnetic resonance imaging.* Nat Rev Neurosci, 2007. **8**(9): p. 700-711.

71.   Brown, E.B., et al., *In vivo measurement of gene expression, angiogenesis and physiological function in tumors using multiphoton laser scanning microscopy.* Nat Med, 2001. **7**(7): p. 864-868.

72.   Drew, P.J., et al., *Chronic optical access through a polished and reinforced thinned skull.* Nat Meth, 2010. **7**(12): p. 981-984.

73.   Blinder, P., et al., *The cortical angiome: an interconnected vascular network with noncolumnar patterns of blood flow.* Nature Neuroscience, 2013. **16**(7): p. 889-897.

74.   Ren, H.-G., C.-W. Du, and Y.-T. Pan, *Cerebral blood flow imaged with ultrahigh-resolution optical coherence angiography and Doppler tomography.* Optics Letters, 2012. **37**(8): p. 1388-1390.

75.   Ren, H.-G., et al., *Quantitative imaging of red blood cell velocity invivo using optical coherence Doppler tomography.* Appl Phys Lett. , 2012. **100**(23): p. 233702-2337024.

76.   Hope-Ross, M., et al., *Adverse reactions due to indocyanine green.* Ophthalmology, 1994. **101**(3): p. 529-33.

77.   Leitgeb, R.A., et al., *Real-time measurement of in vitro flow by Fourier-domain color Doppler optical coherence tomography.* Optics Letters, 2004. **29**(2): p. 171-173.

78.   Vakoc, B., et al., *Phase-resolved optical frequency domain imaging.* Optics Express, 2005. **13**(14): p. 5483-5493.

79.   Koch, E., J. Walther, and M. Cuevas, *Limits of Fourier domain Doppler-OCT at high velocities.* Sensors and Actuators A: Physical, 2009. **156**(1): p. 8-13.

80.   Itoh, K., *Analysis of the phase unwrapping algorithm.* Applied Optics, 1982. **21**(14): p. 2470-2470.

81.   Bouwens, A., et al., *Quantitative lateral and axial flow imaging with optical coherence microscopy and tomography.* Optics Express, 2013. **21**(15): p. 17711-17729.

82.   Peterson, L.M., et al., *Orientation-independent rapid pulsatile flow measurement using dual-angle Doppler OCT.* Biomedical Optics Express, 2014. **5**(2): p. 499-514.

83.   Trasischker, W., et al., *In vitro and in vivo three-dimensional velocity vector measurement by three-beam spectral-domain Doppler optical coherence tomography.* Journal of Biomedical Optics, 2013. **18**(11): p. 116010-116010.

84.   Pan, Y.T., et al., *Subcellular imaging of epithelium with time-lapse optical coherence tomography.* Journal of Biomedical Optics, 2007. **12**(5): p. 050504-050504-3.

85.   Batchelor, G.K., *An Introduction to Fluid Dynamics.* 2000: Cambridge University Press.

86.   Kim, T.N., et al., *Line-Scanning Particle Image Velocimetry: An Optical Approach for Quantifying a Wide Range of Blood Flow Speeds in Live Animals.* PLoS ONE, 2012. **7**(6): p. e38590.

87.   Yousefi, S., T. Liu, and R.K. Wang, *Segmentation and quantification of blood vessels for OCT-based micro-angiograms using hybrid shape/intensity compounding.* Microvascular Research, 2015. **97**(0): p. 37-46.

88.   Ostrom, Q.T., et al., *CBTRUS Statistical Report: Primary Brain and Other Central Nervous System Tumors Diagnosed in the United States in 2009–2013.* Neuro-Oncology, 2016. **18**(suppl_5): p. v1-v75.

89.   Laws, E.R., et al., *Survival following surgery and prognostic factors for recently diagnosed malignant glioma: data from the Glioma Outcomes Project.* J Neurosurg, 2003. **99**(3): p. 467-73.

90.   Hamstra, D.A., et al., *Functional Diffusion Map As an Early Imaging Biomarker for High-Grade Glioma: Correlation With Conventional Radiologic Response and Overall Survival.* Journal of Clinical Oncology, 2008. **26**(20): p. 3387-3394.

91.   Moffat, B.A., et al., *Functional diffusion map: A noninvasive MRI biomarker for early stratification of clinical brain tumor response.* Proceedings of the National Academy of Sciences of the United States of America, 2005. **102**(15): p. 5524-5529.

92.   Spence, A.M., D.A. Mankoff, and M. Muzi, *Positron emission tomography imaging of brain tumors.* Neuroimaging Clin N Am, 2003. **13**(4): p. 717-39.

93.   Van de Wiele, C., et al., *Nuclear medicine imaging to predict response to radiotherapy: a review.* International Journal of Radiation Oncology*Biology*Physics, 2003. **55**(1): p. 5-15.

94.   Wang, S., et al., *Three-dimensional computational analysis of optical coherence tomography images for the detection of soft tissue sarcomas.* J Biomed Opt, 2014. **19**(2): p. 21102.

95.   Ren, H., et al., *Enhancing Detection of Bladder Carcinoma In Situ by 3-Dimensional Optical Coherence Tomography.* The Journal of Urology, 2010. **184**(4): p. 1499-1506.

96.   Zakharov, V.P., et al., *Comparative analysis of combined spectral and optical tomography methods for detection of skin and lung cancers.* J Biomed Opt, 2015. **20**(2): p. 25003.

97.   Vakoc, B.J., et al., *Three-dimensional microscopy of the tumor microenvironment in vivo using optical frequency domain imaging.* Nat Med, 2009. **15**(10): p. 1219-1223.

98.   Lin, R., et al., *Longitudinal label-free optical-resolution photoacoustic microscopy of tumor angiogenesis in vivo.* Quantitative Imaging in Medicine and Surgery, 2014. **5**(1): p. 23-29.

99.   Weis, S.M. and D.A. Cheresh, *Tumor angiogenesis: molecular pathways and therapeutic targets.* Nat Med, 2011. **17**(11): p. 1359-1370.

100.   Carmeliet, P., *Angiogenesis in life, disease and medicine.* Nature, 2005. **438**(7070): p. 932-6.

101.   Welter, M., K. Bartha, and H. Rieger, *Vascular remodelling of an arterio-venous blood vessel network during solid tumour growth.* Journal of Theoretical Biology, 2009. **259**(3): p. 405-422.

102.   You, J., et al., *Quantitative imaging of microvascular blood flow networks in deep cortical layers by 1310 nm muODT.* Opt Lett, 2015. **40**(18): p. 4293-6.

103.   Pan, Y., et al., *Ultrasensitive detection of 3D cerebral microvascular network dynamics in vivo.* NeuroImage, 2014. **103**: p. 492-501.

104.   Park, K., et al., *Cranial window implantation on mouse cortex to study microvascular change induced by cocaine.* Quantitative Imaging in Medicine and Surgery, 2015. **5**(1): p. 97-107.

105.   Cadotte, D.W., et al., *Speckle variance optical coherence tomography of the rodent spinal cord: in vivo feasibility.* Biomedical Optics Express, 2012. **3**(5): p. 911-919.

106.   Liu, X., M. Kirby, and F. Zhao, *Motion analysis and removal in intensity variation based OCT angiography.* Biomedical Optics Express, 2014. **5**(11): p. 3833-3847.

107.   Olabarriaga, S.D., M. Breeuwer, and W.J. Niessen, *Evaluation of Hessian-based filters to enhance the axis of coronary arteries in CT images.* International Congress Series, 2003. **1256**: p. 1191-1196.

108.   Krupinski, J., et al., *Three-dimensional structure and survival of newly formed blood vessels after focal cerebral ischemia.* Neuroreport, 2003. **14**(8): p. 1171-6.

109.   Lange , R.A. and L.D. Hillis *Cardiovascular Complications of Cocaine Use.* New England Journal of Medicine, 2001. **345**(5): p. 351-358.

110.   Satran, A., et al., *Increased Prevalence of Coronary Artery Aneurysms Among Cocaine Users.* Circulation, 2005. **111**(19): p. 2424-2429.

111.   Treadwell, S.D. and T.G. Robinson, *Cocaine use and stroke.* Postgraduate Medical Journal, 2007. **83**(980): p. 389-394.

112.   Toossi, S., et al., *Neurovascular complications of cocaine use at a tertiary stroke center.* J Stroke Cerebrovasc Dis, 2010. **19**(4): p. 273-8.

113.   Archavlis, E. and M. Carvi Y Nievas, *Cerebral vasospasm: a review of current developments in drug therapy and research.* journal of Pharmaceutical Technology and Drug Research, 2013. **2**(1).

114.   Pereira, J., et al., *Platelet activation in chronic cocaine users: Effect of short term abstinence.* Platelets, 2011. **22**(8): p. 596-601.

115.   Sáez, C.G., et al., *Increased number of circulating endothelial cells and plasma markers of endothelial damage in chronic cocaine users.* Thrombosis Research, 2011. **128**(4): p. e18-e23.

116.   Daras, M., A.J. Tuchman, and S. Marks, *Central nervous system infarction related to cocaine abuse.* Stroke, 1991. **22**(10): p. 1320-5.

117.   Sakadžić, S., et al., *High-resolution in vivo optical imaging of stroke injury and repair.* Brain Research, 2015. **1623**: p. 174-192.

118.   Jia, Y., et al., *In vivo optical imaging of revascularization after brain trauma in mice.* Microvascular Research, 2011. **81**(1): p. 73-80.

119. Srinivasan, V.J., et al., *Multiparametric, Longitudinal Optical Coherence Tomography Imaging Reveals Acute Injury and Chronic Recovery in Experimental Ischemic Stroke.* PLoS ONE, 2013. **8**(8): p. e71478.
120. Morrell, J.I., J.C. Basso, and M. Pereira, *Both High and Low Doses of Cocaine Derail Normal Maternal Caregiving – Lessons from the Laboratory Rat.* Frontiers in Psychiatry, 2011. **2**: p. 30.
121. Sofuoglu, M., et al., *Intravenous cocaine increases plasma epinephrine and norepinephrine in humans.* Pharmacology Biochemistry and Behavior, 2001. **68**(3): p. 455-459.
122. ABBOUD, F.M., et al., *Sensitization of Arteries, Veins, and Small Vessels to Norepinephrine After Cocaine.* Circulation Research, 1964. **15**(3): p. 247-257.
123. Yu, X., et al., *Direct imaging of macrovascular and microvascular contributions to BOLD fMRI in layers IV–V of the rat whisker–barrel cortex.* NeuroImage, 2012. **59**(2): p. 1451-1460.
124. Yu, X., et al., *Deciphering laminar-specific neural inputs with line-scanning fMRI.* Nat Meth, 2014. **11**(1): p. 55-58.
125. Frangi, A.F., et al., *Multiscale vessel enhancement filtering*, in *Medical Image Computing and Computer-Assisted Intervention — MICCAI'98: First International Conference Cambridge, MA, USA, October 11–13, 1998 Proceedings*, W.M. Wells, A. Colchester, and S. Delp, Editors. 1998, Springer Berlin Heidelberg: Berlin, Heidelberg. p. 130-137.
126. Ren, H., et al., *Cocaine-induced cortical microischemia in the rodent brain: clinical implications.* Mol Psychiatry, 2012. **17**(10): p. 1017-25.
127. Volkow, N.D., et al., *Cerebral blood flow in chronic cocaine users: a study with positron emission tomography.* Br J Psychiatry, 1988. **152**: p. 641-8.
128. Ibrahim, M., R. Hasan, and M. Awan, *Cocaine-induced coronary stent thrombosis.* Experimental & Clinical Cardiology, 2013. **18**(1): p. e57-e59.
129. Konzen, J.P., S.R. Levine, and J.H. Garcia, *Vasospasm and Thrombus Formation as Possible Mechanisms of Stroke Related to Alkaloidal Cocaine.* Stroke, 1995. **26**(6): p. 1114-1118.
130. Killam, A.L., *Cardiovascular and thrombosis pathology associated with cocaine use.* Hematol Oncol Clin North Am, 1993. **7**(6): p. 1143-51.
131. Volkow, N.D., B. Rosen, and L. Farde, *Imaging the living human brain: Magnetic resonance imaging and positron emission tomography.* Proceedings of the National Academy of Sciences, 1997. **94**(7): p. 2787-2788.
132. Perper, J.A. and D.H. Van Thiel, *Respiratory Complications of Cocaine Abuse*, in *Recent Developments in Alcoholism: Alcohol and Cocaine Similarities and Differences Clinical Pathology Psychosocial Factors and Treatment Pharmacology and Biochemistry Medical Complications*, M. Galanter, Editor. 1992, Springer US: Boston, MA. p. 363-377.
133. Schwartz, B.G., S. Rezkalla, and R.A. Kloner, *Cardiovascular Effects of Cocaine.* Circulation, 2010. **122**(24): p. 2558-2569.
134. Rossini, P.M., et al., *Does cerebrovascular disease affect the coupling between neuronal activity and local haemodynamics?* Brain, 2004. **127**(Pt 1): p. 99-110.
135. Liu, Y.H., et al., *Assessment of neurovascular dynamics during transient ischemic attack by the novel integration of micro-electrocorticography electrode array with functional photoacoustic microscopy.* Neurobiol Dis, 2015. **82**: p. 455-65.
136. Font, M.A., A. Arboix, and J. Krupinski, *Angiogenesis, Neurogenesis and Neuroplasticity in Ischemic Stroke.* Current Cardiology Reviews, 2010. **6**(3): p. 238-244.
137. Krock, B.L., N. Skuli, and M.C. Simon, *Hypoxia-Induced Angiogenesis: Good and Evil.* Genes & Cancer, 2011. **2**(12): p. 1117-1133.
138. Yao, H., M. Duan, and S. Buch, *Cocaine-mediated induction of platelet-derived growth factor: implication for increased vascular permeability.* Blood, 2011. **117**(8): p. 2538-2547.
139. Siepmann, T., et al., *Selective serotonin reuptake inhibitors to improve outcome in acute ischemic stroke: possible mechanisms and clinical evidence.* Brain and Behavior, 2015. **5**(10): p. e00373.

140. Siepmann, T., et al., *The Effects of Pretreatment versus De Novo Treatment with Selective Serotonin Reuptake Inhibitors on Short-term Outcome after Acute Ischemic Stroke.* J Stroke Cerebrovasc Dis, 2015. **24**(8): p. 1886-92.

141. Ravna, A.W., I. Sylte, and S.G. Dahl, *Molecular Mechanism of Citalopram and Cocaine Interactions with Neurotransmitter Transporters.* Journal of Pharmacology and Experimental Therapeutics, 2003. **307**(1): p. 34-41.

142. Thompson, B.J., et al., *Transgenic elimination of high-affinity antidepressant and cocaine sensitivity in the presynaptic serotonin transporter.* Proceedings of the National Academy of Sciences, 2011. **108**(9): p. 3785-3790.

143. You, J., et al., *Quantitative imaging of microvascular blood flow networks in deep cortical layers by 1310 nm μODT.* Optics Letters, 2015. **40**(18): p. 4293-4296.

144. Merkle, C.W. and V.J. Srinivasan, *Laminar microvascular transit time distribution in the mouse somatosensory cortex revealed by Dynamic Contrast Optical Coherence Tomography.* NeuroImage, 2016. **125**: p. 350-362.

145. Jackman, K. and C. Iadecola, *Neurovascular regulation in the ischemic brain.* Antioxid Redox Signal, 2015. **22**(2): p. 149-60.

146. Devonshire, I.M., J.E.W. Mayhew, and P.G. Overton, *Cocaine preferentially enhances sensory processing in the upper layers of the primary sensory cortex.* Neuroscience, 2007. **146**(2): p. 841-851.

147. Kusaka, N., et al., *Enhanced brain angiogenesis in chronic cerebral hypoperfusion after administration of plasmid human vascular endothelial growth factor in combination with indirect vasoreconstructive surgery.* J Neurosurg, 2005. **103**(5): p. 882-90.

148. Marti, H.H., *Angiogenesis--a self-adapting principle in hypoxia.* Exs, 2005(94): p. 163-80.

149. Boylan, J.F., et al., *Cocaine toxicity and isoflurane anesthesia: hemodynamic, myocardial metabolic, and regional blood flow effects in swine.* J Cardiothorac Vasc Anesth, 1996. **10**(6): p. 772-7.

150. Bélanger, M., I. Allaman, and Pierre J. Magistretti, *Brain Energy Metabolism: Focus on Astrocyte-Neuron Metabolic Cooperation.* Cell Metabolism. **14**(6): p. 724-738.

151. Iadecola, C., *Neurovascular regulation in the normal brain and in Alzheimer's disease.* Nature Reviews Neuroscience, 2004. **5**: p. 347.

152. Tran, C.H.T. and G.R. Gordon, *Acute two-photon imaging of the neurovascular unit in the cortex of active mice.* Frontiers in Cellular Neuroscience, 2015. **9**(11).

153. Hillman, E.M., et al., *Depth-resolved optical imaging and microscopy of vascular compartment dynamics during somatosensory stimulation.* Neuroimage, 2007. **35**(1): p. 89-104.

154. Kleinfeld, D., et al., *Fluctuations and stimulus-induced changes in blood flow observed in individual capillaries in layers 2 through 4 of rat neocortex.* Proceedings of the National Academy of Sciences, 1998. **95**(26): p. 15741-15746.

155. Devor, A., et al., *Frontiers in optical imaging of cerebral blood flow and metabolism.* Journal of Cerebral Blood Flow & Metabolism, 2012. **32**(7): p. 1259-1276.

156. Marota, J.J., et al., *Investigation of the early response to rat forepaw stimulation.* Magnetic resonance in medicine, 1999. **41**(2): p. 247-252.

157. Shih, A.Y., et al., *Two-photon microscopy as a tool to study blood flow and neurovascular coupling in the rodent brain.* J Cereb Blood Flow Metab, 2012. **32**(7): p. 1277-309.

158. Chen, T.-W., et al., *Ultrasensitive fluorescent proteins for imaging neuronal activity.* Nature, 2013. **499**(7458): p. 295-300.

159. Chen, T.-W., et al., *Ultra-sensitive fluorescent proteins for imaging neuronal activity.* Nature, 2013. **499**(7458): p. 295-300.

160. Huneau, C., H. Benali, and H. Chabriat, *Investigating Human Neurovascular Coupling Using Functional Neuroimaging: A Critical Review of Dynamic Models.* Frontiers in Neuroscience, 2015. **9**(467).

161.   Hall, C.N., et al., *Capillary pericytes regulate cerebral blood flow in health and disease.* Nature, 2014. **508**: p. 55.
162.   Boas, D.A. and A.K. Dunn. *Laser speckle contrast imaging in biomedical optics*. 2010. SPIE.
163.   Yu, X., et al., *Deciphering laminar-specific neural inputs with line-scanning fMRI.* Nature Methods, 2013. **11**: p. 55.
164.   Yu, X., et al., *Direct Imaging of Macrovascular and Microvascular Contributions to BOLD fMRI in Layer IV–V of the Rat Whisker-Barrel Cortex.* NeuroImage, 2012. **59**(2): p. 1451-1460.
165.   Silva, A.C. and A.P. Koretsky, *Laminar specificity of functional MRI onset times during somatosensory stimulation in rat.* Proc Natl Acad Sci U S A, 2002. **99**(23): p. 15182-7.
166.   Srinivasan, V.J. and H. Radhakrishnan, *Optical Coherence Tomography angiography reveals laminar microvascular hemodynamics in the rat somatosensory cortex during activation.* NeuroImage, 2014. **102, Part 2**: p. 393-406.
167.   Hu, D., et al. *Extended focus optical coherence tomography with optical fiber based Bessel beam illumination*. in *Lasers and Electro-Optics (CLEO), 2013 Conference on*. 2013. IEEE.
168.   Lee, K.-S. and J.P. Rolland, *Bessel beam spectral-domain high-resolution optical coherence tomography with micro-optic axicon providing extended focusing range.* Optics Letters, 2008. **33**(15): p. 1696-1698.
169.   Tamborski, S., et al., *Extended-focus optical coherence microscopy for high-resolution imaging of the murine brain.* Biomedical Optics Express, 2016. **7**(11): p. 4400-4414.
170.   Curatolo, A., et al., *Quantifying the influence of Bessel beams on image quality in optical coherence tomography.* Scientific Reports, 2016. **6**: p. 23483.
171.   Swanson, E.A. and J.G. Fujimoto, *The ecosystem that powered the translation of OCT from fundamental research to clinical and commercial impact [Invited].* Biomedical Optics Express, 2017. **8**(3): p. 1638-1664.
172.   Baran, U. and R.K. Wang, *Review of optical coherence tomography based angiography in neuroscience.* Neurophotonics, 2016. **3**(1): p. 010902.
173.   Srinivasan, V.J., et al., *Optical coherence tomography for the quantitative study of cerebrovascular physiology.* Journal of Cerebral Blood Flow & Metabolism, 2011. **31**(6): p. 1339-1345.
174.   Leitgeb, R.A., et al., *Doppler Optical Coherence Tomography.* Progress in Retinal and Eye Research, 2014. **41**(Supplement C): p. 26-43.
175.   Doblhoff-Dier, V., et al., *Measurement of the total retinal blood flow using dual beam Fourier-domain Doppler optical coherence tomography with orthogonal detection planes.* Biomedical Optics Express, 2014. **5**(2): p. 630-642.
176.   Welter, M., K. Bartha, and H. Rieger, *Vascular remodelling of an arterio-venous blood vessel network during solid tumour growth.* J Theor Biol, 2009. **259**(3): p. 405-22.
177.   Du, C., et al., *Differential effects of anesthetics on cocaine's pharmacokinetic and pharmacodynamic effects in brain.* Eur J Neurosci, 2009. **30**(8): p. 1565-75.
178.   Schwinn, D.A., R.W. McIntyre, and J.G. Reves, *Isoflurane-induced vasodilation: role of the alpha-adrenergic nervous system.* Anesth Analg, 1990. **71**(5): p. 451-9.